Physical synchronization of soft self-oscillating limbs for fast and autonomous locomotion

Accepted Preprint. Published in edited form as: *Science*, May 8th, 2025
doi.org/10.1126/science.adr3661

Alberto Comoretto[1], Harmannus A.H. Schomaker,[1] Johannes T.B. Overvelde[1,*]

[1]Autonomous Matter Department, AMOLF, Science Park 104, 1098 XG Amsterdam, The Netherlands

[*]To whom correspondence should be addressed; E-mail: overvelde@amolf.nl.

Animals achieve robust locomotion by offloading regulation from the brain to physical couplings within the body. In contrast, locomotion in artificial systems often depends on centralized processors. We introduce a rapid and autonomous locomotion strategy with synchronized gaits emerging through physical interactions between self-oscillating limbs and the environment, without control signals. Each limb is a single soft tube that only requires constant flow of air to perform cyclic stepping motions at frequencies reaching 300 hertz. By combining several of these self-oscillating limbs, their physical synchronization enables locomotion speeds that are orders of magnitude faster than comparable state-of-the-art. Through body-environment dynamics, these seemingly simple devices exhibit autonomy, including obstacle avoidance, amphibious gait transitions, and phototaxis.

Nature masters the complex problem of locomotion through embodied solutions, harnessing the synergy between the nervous system, body, and environment (*1*). The foundation of animal locomotion lies in the periodic and asymmetric motion of individual limbs (*2, 3*) (Fig. 1A). Multiple oscillating limbs are typically coordinated through a variety of embodied couplings, which are computationally and metabolically inexpensive by diminishing or even eliminating the need for sequential individual inputs from a central brain (*3*). These embodied couplings are often implemented through both internal neural connections (i.e., explicitly) and external interactions with the environment (i.e., implicitly). For instance, stick insects achieve synchronized walking gaits through both explicit neural connections and implicit body-environment interactions, avoiding centralized patterning (*4*). Sea stars explicitly coordinate their five arms in a decentralized fashion through a nerve ring (*5*) and occasionally exhibit a fast bouncing gait as an escape response, with their hundreds of tube feet achieving synchronization through implicit mechanical coupling with the external substrate (*6*) (Fig. 1A).

Inspired by nature, robots can delegate the locomotion task to their bodies (*7, 8*), thus minimizing energy and time costs associated with a central computer. For instance, by harnessing the dynamics of the body, rigid robots based on passive-dynamic walkers (*9*) and synergy-based quadrupeds (*10*) reduce, but do not eliminate, the amount of control required for locomotion. Without processors, soft robots based on twisting liquid crystal elastomers (*11*) and elasto-active structures (*12*) harness shape reconfiguration to avoid obstacles autonomously. However, due to the lack of limbs, their applicability is limited to specific tasks and environments (*13*), in contrast to the wide spectrum of robust behaviors typical of animals, which is often enabled by interactions between multiple self-oscillators (*14*).

Among soft-limbed robots, fluidic circuits (*15*) sequence the activation of limbs (*16*) for walking gaits (*17–20*) without the need for electronic processors. However, fluidic circuits still emulate their electronic counterpart (*21*), involving multiple, macroscopic, digital or analog components that deliver sequential control signals. This architecture leads to energy losses and delay across the fluidic network, causing slow sequencing of the limbs in the order of one hertz, with consequent ineffective locomotion of only a few body lengths (BLs) per minute (*17–20, 22–26*), which is impractical for most real-world applications (*27–29*). Moreover,

autonomous behavior of walkers with fluidic processors remains elusive, with the exception of one-time-use touch sensing (*18*) and reprogrammable sequencing of non-integrated soft fingers (*19*).

Inspired by the movement principles of animals that do not require centralized processing, we aim to harness physical synchronization of limbs for rapid and autonomous locomotion in soft-limbed robots with embedded fluidic circuits. To do so, in this work we introduce three levels of behavioral hierarchy (Fig. 1B) based on *i)* asymmetric self-oscillating motion at the limb level, *ii)* explicit internal fluidic coupling leading to synchronized gaits, and *iii)* implicit coupling between body dynamics and environmental interactions resulting in autonomous behavior. Based on these principles, we develop robotic demonstrations that display rapid locomotion and adaptive behaviors, providing fundamental and general insights into how to instill autonomy in systems without electronic, electronic-like mechanical (*30*), or fluidic (*21*) processors.

Self-oscillating limb To enable rapid locomotion without a central processor, here we develop a limb that undergoes periodic and asymmetric motions by harnessing a self-oscillating behavior of thin soft tubes, analogous to oscillations occurring in flat tubes with flowing water (*31*), and reminiscent of promotional air dancers (*32*) often seen by the roadside. We build the limb by simply bending a thin-walled commercial silicone tube 180° and constraining it at the inlet and outlet in a 3D-printed holder (Fig. 1C and fig. S1). If no airflow is provided, the tube displays two stable states with either one (*33*) or two kinks (Fig. 1C,D). However, when we apply a constant airflow of 15 standard liter per minute (SLPM) to the inlet on the left side of the tube, the tube starts to spontaneously oscillate between states with one and two kinks, at a frequency of approximately $100\,\mathrm{Hz}$ (Fig. 1E and movie S1) (standard units of airflow in table S1).

The motion of the tube during the oscillation cycle is intrinsically asymmetric due to the applied directed airflow. As a result, the tip of the limb, which we define as the point on the tube closest to a defined surface (Fig. 1F and fig. S10), traces a hysteretic trajectory in the x-y plane orthogonal to the surface (Fig. 1G and fig. S10). The tube, therefore, acts as a limb that undergoes a full-step motion, with a periodic closed-loop sequence of stance and swing phases (Fig. 1L and movie S1), reminiscent of animals' limbs (*3*) (Fig. 1A).

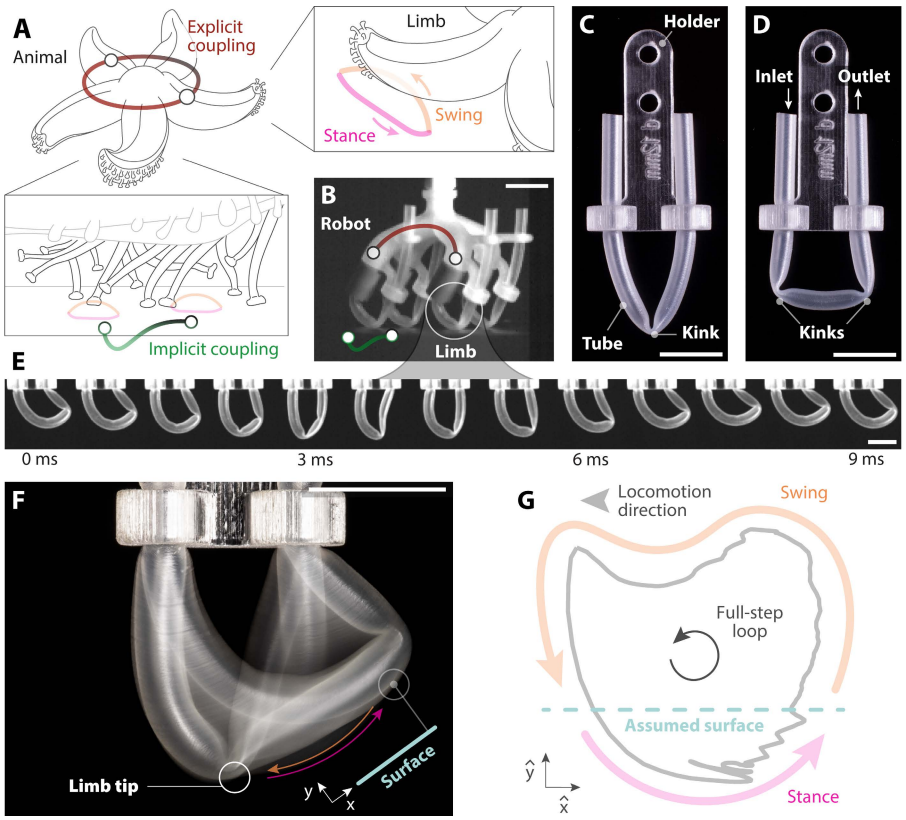

Figure 1: **Self-oscillating limbs that cyclically perform full-step motions.** (**A**) Animals locomote by coordinating multiple limbs via explicit coupling through neural connections or implicit coupling through interaction with the environment (*4–6*). Each limb of the animal performs oscillating and asymmetric (full-step) motions with stance and swing phases (*2, 3*). (**B**) We exploit these principles of explicit and implicit couplings between self-oscillating limbs for autonomous locomotion in robots. Our artificial limb is a soft tube bent 180° that, in static conditions, displays (**C**) one or (**D**) two kinks. (**E**) When constant airflow of 15 standard liter per minute (SLPM) is provided at the inlet on the left end, the tube self-oscillates at a frequency of 115 Hz (snapshots of one oscillation cycle). (**F**) The tip of the limb is the point on the tube closest to a defined surface (photograph with 0.5 s exposure time, capturing $\sim$ 50 consecutive oscillations). (**G**) The tip cyclically undergoes a full-step loop trajectory, with a stance phase followed by a swing phase (the reported tip trajectory coordinates $\hat{x}$ and $\hat{y}$ are normalized). Scale bars are 1 cm.

For constant input airflow, we delegate both the oscillation generation and the sequencing of the tip motion within each cycle directly to the limb itself, bypassing the requirement of additional circuitry (*15*), either fluidic (*18, 20*) or electronic (*34*).

We next aim to empirically understand the switching behavior between one and two kinks in the self-

oscillating limb. To do so, we detect the outer and inner edges of the tube (Fig. 2A and Supplementary Material section M3) and we map them on a new coordinate system along the center line of the tube (Fig. 2B, fig. S5 and fig. S12). Focusing on the local minima of the tube width, we indeed identify one or two kinks (Fig. 2B and movie S2). We refer to the kink with the smallest width as the dominant kink, and the second kink (if present at that instant) as the non-dominant kink.

From the location of the kinks in time (Fig. 2C and fig. S12), and the inlet pressure (Fig. 2D), we can identify four key steps during a single oscillation cycle. At $\sim 5\,\mathrm{ms}$ (Fig. 2E), we observe two kinks staying approximately at the same location on the tube until $\sim 35\,\mathrm{ms}$ (Fig. 2F). During this time, the pressure at the inlet decreases, causing the non-dominant kink to increasingly sharpen (fig. S21). Between $\sim 35\,\mathrm{ms}$ and $\sim 40\,\mathrm{ms}$ the non-dominant kink becomes dominant, while the other kink disappears at $\sim 40\,\mathrm{ms}$ (Fig. 2G). Until $\sim 60\,\mathrm{ms}$, the only kink in the tube starts to travel along the tube (Fig. 2H), as a result of an increase in pressure before the kink (fig. S14). Finally, after $\sim 60\,\mathrm{ms}$, a new kink forms upstream again due to an increase in bending moment (fig. S21). This state (equivalent to Figure 2E) is characterized by a lower fluidic resistance than the single kink state in Figure 2G, as both kinks have a larger angle (fig. S21), and thus causes pressure to drop again.

From a basic mass-spring model (Supplementary Material section S1), we gain insight into three ingredients that lead to the self-oscillating behavior (fig. S6): *i)* a local nonlinear torque-angle curve under bending leads to localized kinking of the tube (fig. S8); *ii)* the local flow resistance increases at the kink location, leading to increased pressure before the kink (fig. S20); *iii)* pressurization of the tube increases the torque required for kinking and unkinking (fig. S8 and fig. S9). Overall, for a constant inflow of air, the internal pressure varies depending on the kinks' resistance. In turn, pressure decrease favors kink growth, and pressure increase causes kinks to travel. This interaction between tube stiffening, kink growth and travel, and change in resistance sets up a hysteric actuation loop (fig. S14) that results in the self-oscillating behavior for constant inflow.

We find that the frequency of the self-oscillation can be tuned by varying the flowrate through the tube.

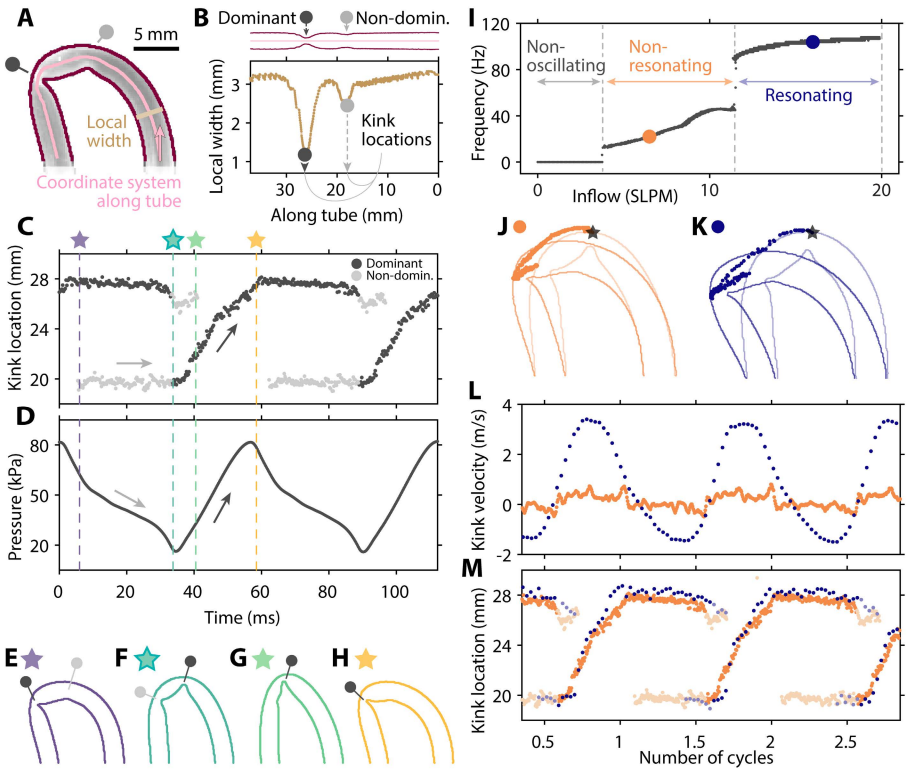

Figure 2: **Interplay between pressure and kinks' state enables self-oscillation at a range of frequencies.** (**A**) Detected edges of the tube (dark red) and coordinate system along the tube (pink). (**B**) The dominant and non-dominant kinks correspond to the local minima (black and grey dots) of the local width along the tube. The (**C**) location of the kinks along the tube and (**D**) pressure inside the tube are coupled. (**E**, **F**, **G**, **H**) State of the tube at four instants of the oscillating cycle. (**I**) The oscillation frequency displays three regimes for different inflow rates. Orange and blue dots correspond to the non-resonating and resonating study cases at 6.5 SLPM and 16 SLPM, respectively. The tube has lower structural displacement in the (**J**) non-resonating domain than in the (**K**) resonating domain, as shown by the kink covering a shorter distance. (**L**) In the resonating case, the structure undergoes high quasi-sinusoidal velocities, in comparison to the near-zero velocities of the non-resonating case. (**M**) The kink locations along the tube itself, for the two cases, overlap.

When we sweep the inflow between 0 and 20 SLPM, we observe three domains, with sharp transitions between them (Fig. 2I). For inflow values below $\sim$ 3.8 SLPM, the tube leaks and does not oscillate (fig. S13). For flowrates between $\sim$ 3.8 SLPM and $\sim$ 11.4 SLPM, the system oscillates at frequencies between $\sim$ 13 and $\sim$ 45 Hz. For even higher flowrates the frequency suddenly jumps to higher frequencies above $\sim$ 90 Hz.

This last sudden jump in frequency seems to be the result of structural resonance (movie S2). This can

be seen from the increase in the distance traveled by the kink (Fig. 2J,K and fig. S12) and by the dramatic increase in the kink velocity, that approaches a sinusoidal trend (Fig. 2L) (Supplementary Material section M3 for the definitions of kink distance and velocity). In comparison, the kink location along the tube does not change considerably when the flow is increased (Fig. 2M), therefore not constituting the origin of the sudden increase in frequency. We conclude that we can significantly increase the oscillation frequency by exploiting the resonance of the structure, as well as by varying design parameters (fig. S11 and fig. S18).

Explicit internal coupling of multiple limbs for ultrafast locomotion The individual self-oscillating limb requires integration with other limbs in a multi-limbed system to enable locomotion and autonomy in robotic applications. With the goal of synchronizing the activation of several limbs to generate specific gaits, we couple two limbs by connecting them in parallel to a single input, using two identical coupling tubes with an inner diameter of $2\,\mathrm{mm}$ (Fig. 3A). When providing a constant airflow to the inlet we observe that coupling tubes shorter than $12\,\mathrm{cm}$ lead to in-phase synchronization. The result is that the two kinks travel simultaneously (Fig. 3B) and the pressure signals align (Fig. 3C and movie S3), even though the natural frequencies of the two limbs are not identical and differ by $\sim 5\,\mathrm{Hz}$ ($\sim 2\%$) (fig. S15). In contrast, coupling tubes longer than $12\,\mathrm{cm}$ result in anti-phase synchronization where the limbs alternatively activate with a phase shift of $\sim 180°$ (Fig. 3D,E and movie S3).

When scanning a wide range of the coupling tubes' length, we note a sharp transition between the in-phase and anti-phase eigenmodes (Fig. 3F,G). When placed at this transition, the system continuously switches between the in-phase and anti-phase eigenmodes (violin plot at $12\,\mathrm{cm}$ in Figure 3G, figure S15 and movie S3).

This synchronization effect is reminiscent of strong coupling between the two oscillators (*35*). In soft systems, strong coupling has previously been observed in mechanically-coupled liquid crystalline oscillators (*36*), while here the coupling is induced by the fluidic interconnections.

Based on these findings, we build a robot with four strongly-coupled self-oscillating limbs, assembled onto a 3D-printed body with short inner channels with length $\sim 1.5\,\mathrm{cm}$, connected in parallel to a single

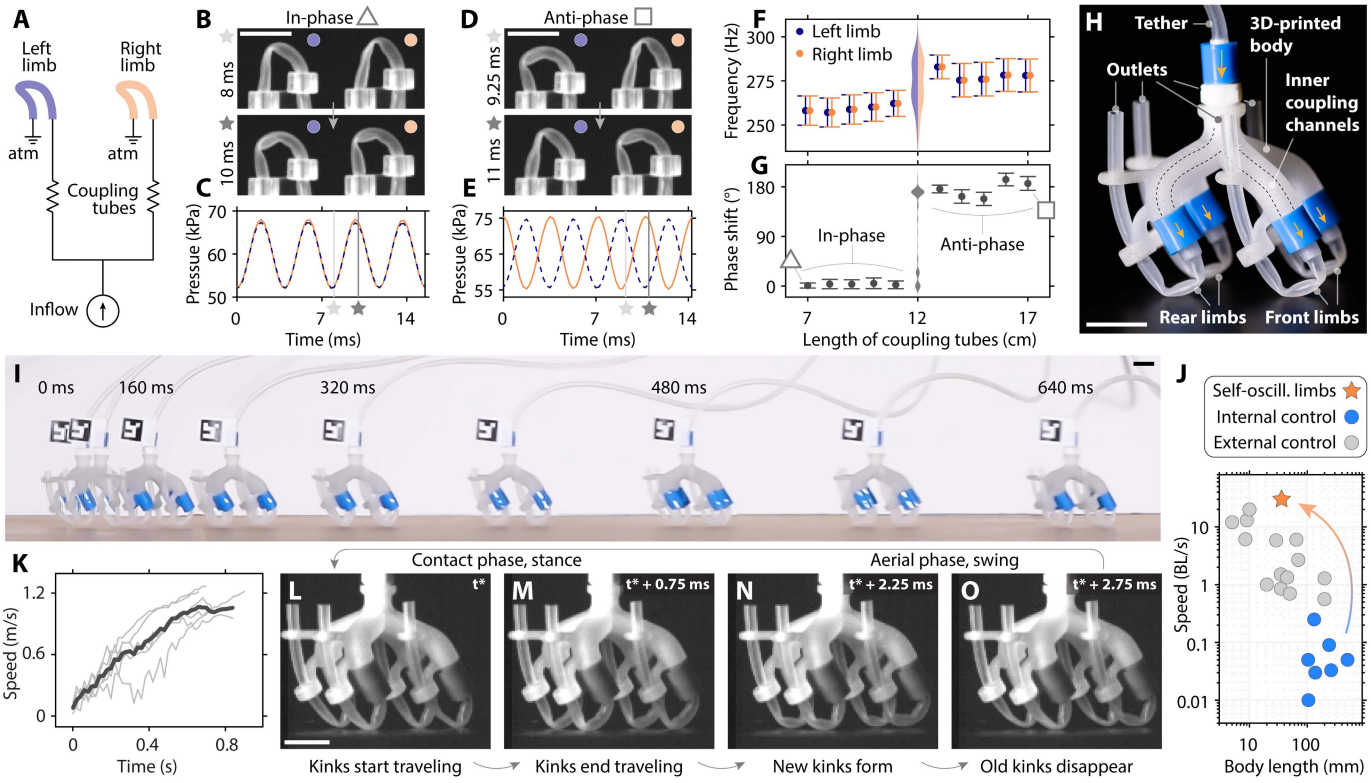

Figure 3: **Synchronization of multiple limbs through explicit, internal coupling for ultrafast locomotion.** (**A**) We couple two limbs in parallel to the same input flow source of 15 SLPM with two identical silicone tubes. We observe in-phase synchronization, with (**B**) simultaneous kink traveling and (**C**) aligned pressure signals, or anti-phase synchronization, with (**D**, **E**) alternate activation of the limbs. We scan the length of the coupling tubes, observing two separated in-phase and anti-phase domains, as (**F**) the oscillation frequency of left and right limbs match, and (**G**) the phase-shift is either $\sim 0°$ or $\sim 180°$. (**H**) The tethered robot has four limbs connected to a 3D-printed monolithic body, with four inner coupling channels. (**I**) The robot achieves ultrafast locomotion on a flat surface (speed $\sim$ 30 BL/s, 1.1 m/s). (**J**) Comparison between tethered soft robots with internal and external control and our robot equipped with synchronizing self-oscillating limbs, in terms of relative speed and body length. (**K**) Speed of the robot for six runs (grey) and mean speed (black). The four limbs, within ~ 3 ms, simultaneously go through a (**L**, **M**) stance phase, followed by a (**N**, **O**) swing phase. All scale bars are 1 cm.

tether (Fig. 3H, fig. S3 and fig. S4). We orient the limbs with a $30°$ angle to the surface to optimize the effective stance (fig. S10). When we provide a constant inflow of $\sim$ 28 SLPM to the tether (fig. S22), the robot accelerates (Fig. 3I and movie S4), reaching a steady-state speed of 30 ± 2.5 BL/s (1.1 m/s) (Fig. 3J,K), with a response time of 0.66 s (Fig. 3K and fig. S22) and Froude number $\sim$ 20.6 (Supplementary Material

section S4). This speed is two orders of magnitude higher than comparable state-of-the-art tethered robots with internal actuation sequencing (*20*), and similar to current ultrafast tethered soft robots that need external control (*37*) (Fig. 3J, fig. S27 and table S2).

Looking closely at the gait in Figure 3L-O and movie S4, we observe that all the limbs autonomously activate in synchrony, since we used short inner coupling channels. The robot runs with a stotting gait, typical of gazelles (*38*), reached after some initial transient asynchronous behavior which lasts $\sim 0.2\,\mathrm{s}$ (Fig. 3K and movie S4). Note that the four limbs oscillate at a frequency of $\sim 300\,\mathrm{Hz}$ (Fig. 3L-O), about three times higher than the case of the single limb that we analyzed in Figure 2, because the tubes are smaller in diameter by a factor ~ 0.8 and shorter in length by a factor ~ 0.5 (Supplementary Material section S4).

Implicit environmental coupling for fast and autonomous locomotion Even though our robot achieved ultrafast locomotion without external control, it still required a tether that provides a power of $\sim 85\,\mathrm{W}$, leading to a relatively high cost of transport of ~ 1926 (Supplementary Material section S4). At the moment, it is not possible to generate this power from a lightweight on-board pressure source, making this robot not directly suited for untethered applications. We find that the main limitation comes from the required flow of ~ 3.8 SLPM for the individual limb to not leak through the kink and start oscillating (Fig. 2I and fig. S13). We hypothesize that an increase in kink resistance can reduce the leakage and thus the minimum flow needed to achieve self-oscillation, thus reducing the required power.

We modified the design of our tubes by heat-sealing two thermoplastic polyurethane (TPU) sheets along two parallel lines. We mount this TPU component to a hinge joint to obtain a self-oscillating pouch limb (fig. S2). This updated limb has a much higher flow resistance upon kinking (fig. S21) and performs the full-step oscillation (Fig. 4A) with a minimum input airflow of only $0.1\ \mathrm{SLPM}$ (fig. S16). Compared to the silicone tube limb, we observe a lower oscillation frequency of maximum $\sim 3.5\,\mathrm{Hz}$ (fig. S16 and fig. S18). This is likely due to the higher geometric volume of air required for the kink to travel ($\sim 2.5\,\mathrm{mL}$ compared to $\sim 0.04\,\mathrm{mL}$, Supplementary Material section S2) which leads to a longer kink traveling time, and the absence

of a resonant mode. However, this frequency reduction is compensated by a larger stroke per cycle of the pouch limb (Fig. 4B, fig. S16 and movie S1).

We build an untethered robot with two pouch tubes as soft limbs, each requiring only $\sim 0.06\,\mathrm{W}$ of fluidic power (Supplementary Material section S2 and fig. S17), and each connected to its own $3\,\mathrm{V}$ air pump, powered by a $3.7\,\mathrm{V}$ LiPo battery with $380\,\mathrm{mA\,h}$ (Fig. 4C, fig. S3 and fig. S4). The total weight of the assembled robot equals $76.7\,\mathrm{g}$, which is ~ 6 times lower than the maximum force two pouch-based limbs can provide (fig. S19). When we turn the pumps on, the robot starts to cyclically hop at a rate of $\sim 2\,\mathrm{Hz}$ (movie S5), with each hopping cycle characterized by a stance phase followed by a swing phase (Fig. 4D). The untethered robot moves with a speed of $1.93 \pm 0.07\,\mathrm{BL/s}$ ($18.1\,\mathrm{cm/s}$) (fig. S22), which is one order of magnitude faster than untethered soft fluidic robots (*26*), and comparable to state-of-the-art untethered soft robots (*39*) (fig. S27 and table S3). Under the tested conditions, the robot locomotes with a cost of transport ~ 11, in the same order of land animals of comparable size such as mice (*40*), and with Froude number ~ 0.16 (Supplementary Material section S4).

In this untethered scenario, the robot's high speed is attributed to the synchronization of the soft limbs. However, in this case, synchronization emerges due to implicit interactions with the environment, and not through embedded fluidic connections as was the case for the tethered robot, as each limb has its own power source. In principle, we observe that the two limbs actuate at different natural frequencies and thus out of phase when placed upside down (Fig. 4E and movie S5). When we flip the robot into the working position where the two limbs interact with the ground, either on a flat surface (Fig. 4F) or on gravel (fig. S23 and fig. S24), the limbs start to actuate simultaneously and in-phase, while requiring higher pressures (Fig. 4G and movie S5). This in-phase synchronization results from the positive coupling between the limbs, where the activation of one limb stimulates the activation of the other limb. Additional mass stabilizes the in-phase synchronized mode and improves the tolerance to imbalance in left and right input flows (Supplementary Material section S4 and fig. S26).

Harnessing such implicit interactions to achieve synchronization also enables autonomous behaviors, as

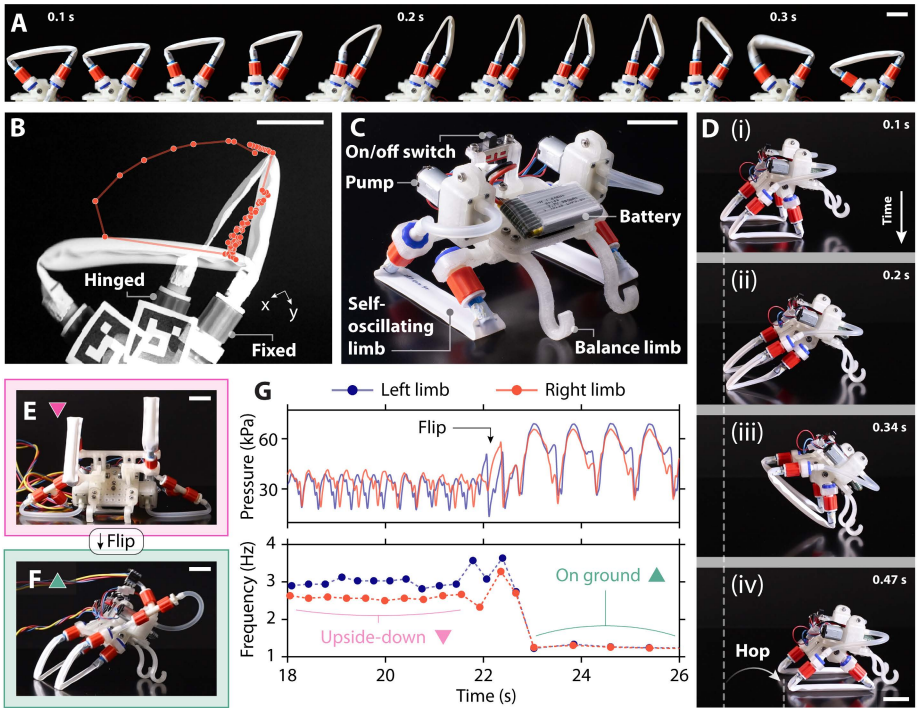

Figure 4: **Synchronization of limbs through implicit interaction for fast, untethered locomotion.** The updated pouch limb (**A**) cyclically performs full-step motions with a low inflow of 0.3 SLPM, (**B**) displaying large hysteresis and stroke enabled by a hinge joint. (**C**) We mount two self-oscillating limbs on an untethered robot that carries a LiPo battery and two pumps. (**D**) The robot cyclically hops with (i, ii) a stance phase followed by (iii, iv) a swing phase. (**E**) The two limbs are not synchronized when the system is upside down, because they are independently powered by the two pumps. (**F**) When the robot interacts with the ground, the two limbs synchronize. (**G**) While interacting, the pressure signals of the two limbs increase, and the frequencies equalize. All scale bars are 2 cm.

external cues can affect the coupling between the body dynamics and the environment. For instance, through implicit coupling with its surroundings, the robot autonomously transitions to a new locomotion gait when interacting with an aquatic environment (Fig. 5A and movie S6), without requiring any control input (*14*) or morphological change (*40*). After diving into the water, the in-phase hopping gait within seconds transitions to an anti-phase gait (Fig. 5B), which is stable in steady-state conditions, with a phase shift of $181 \pm 8°$ (Supplementary Material section S4). The anti-phase gait seems to be stabilized by a sideways swaying of the robot, leading to negative coupling in which the activation of a limb suppresses the activation of the other limb

(movie S6). To confirm this, we check that manually constraining the swaying motion causes the limbs to not synchronize anymore (movie S6). Therefore, the coupling between the body dynamics and the surrounding medium determines the stability of a specific gait for the robot and, thus, its behavior.

When encountering an obstacle, too, the mechanical interactions between the body and an obstacle cause temporary asynchronous activation of the legs, resulting in the robot steering in place and avoiding the obstacle (Fig. 5C and movie S6). By harnessing these environmental cues, the robot changes behavior and autonomously escapes a U-shaped obstruction after noisy and consecutive random changes of direction (Fig. S25 and movie S6).

As the amphibious locomotion is unidirectional and the body-obstacle interactions result in random outcomes (movie S6), we propose that additional sensing is still needed to provide the robot with a high-level sense of direction. We take inspiration from Braitenberg's 'aggressive vehicle 2b' (*41*), and design internal connections by equipping the robot with two 'eyes' (LDR light sensors) that activate the opposite soft limbs when sensing light (Fig. 5D and fig. S4). This relatively simple robot achieves autonomous phototaxis, as it steers in place when only one eye detects light and implicitly coordinates the limbs to hop forward when both eyes do (fig. S22 and movie S7). Outside of the lab, this allows the robot to move from a dark room to a brighter one (movie S7) and to continuously follow an operator who carries a light (Fig. 5E and movie S7).

Conclusions In conclusion, we leverage kinks traveling along a soft tube to create a self-oscillating limb that cyclically performs a full-step motion at high frequencies. Inspired by nature, we blur the boundaries between actuation, control, and body-environment feedback by physically synchronizing multiple limbs via explicit and implicit couplings, realizing rapidly moving, autonomous robots. The observations from the various robotic demonstrations we performed point towards the potential of a holistic and overarching approach when designing robots, to achieve robust and adaptive behavior across diverse environments. This approach does place emphasis on the physical design of the highly interacting robot, and therefore, it will likely require the development and improvement of available design tools for these types of integrated systems to discover or

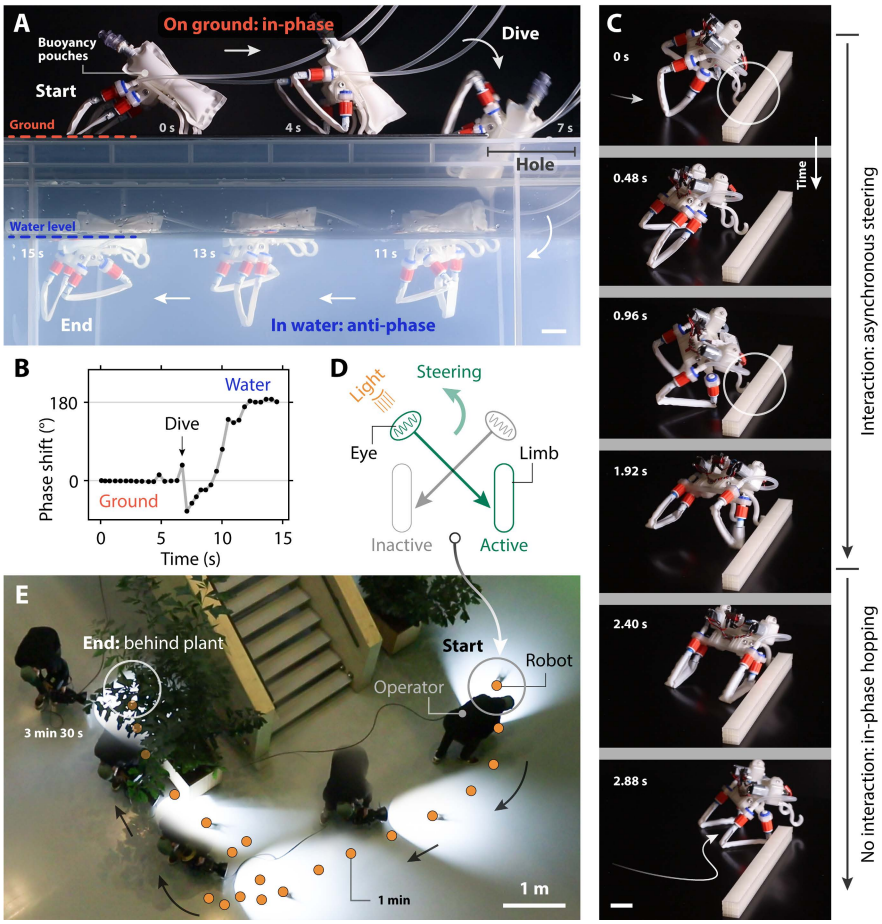

Figure 5: **Autonomy through physical interactions with the environment.** (**A**) After diving into the water, the robot equipped with buoyancy pouches (50 mL of air) autonomously transitions to an anti-phase swimming gait, through the implicit coupling with the new aquatic environment. (**B**) The phase shift between the two self-oscillating limbs is $\sim 0°$ (in-phase) when hopping on the ground and spontaneously transitions to $\sim 180°$ (anti-phase) when interacting with water. (**C**) When encountering an obstacle, the mechanical interactions (white circles) cause the limbs to activate asynchronously and, as a consequence, the robot steers in place, avoiding the obstacle. (**D**) To provide the robot with a high-level sense of direction, and inspired by Braitenberg's 'aggressive vehicle' (*41*), we cross-link light sensors (eyes) and the pumps so that a limb is active when the opposite eye detects light. (**E**) This robot achieves autonomous phototaxis by steering in place when only one eye is active and hopping forward when both eyes are, following an operator that carries a light in a real-world environment. Wherever not otherwise stated, scale bars are 2 cm.

design useful and robust emergent dynamic behaviors.

References

1. H. J. Chiel, R. D. Beer, The brain has a body: adaptive behavior emerges from interactions of nervous system, body and environment, *Trends in Neurosciences* **20**, 553-557 (1997).

2. A. J. Ijspeert, Biorobotics: Using robots to emulate and investigate agile locomotion, *Science* **346**, 196-203 (2014).

3. M. H. Dickinson, C. T. Farley, R. J. Full, M. A. R. Koehl, R. Kram, S. Lehman, How animals move: An integrative view, *Science* **288**, 100-106 (2000).

4. H. Cruse, V. Dürr, J. Schmitz, Insect walking is based on a decentralized architecture revealing a simple and robust controller, *Philosophical Transactions of the Royal Society A: Mathematical, Physical and Engineering Sciences* **365**, 221-250 (2007).

5. E. G. Clark, D. Kanauchi, T. Kano, H. Aonuma, D. E. G. Briggs, A. Ishiguro, The function of the ophiuroid nerve ring: how a decentralized nervous system controls coordinated locomotion, *Journal of Experimental Biology* **222**, jeb192104 (2019).

6. S. Heydari, A. Johnson, O. Ellers, M. J. McHenry, E. Kanso, Sea star inspired crawling and bouncing, *Journal of The Royal Society Interface* **17**, 20190700 (2020).

7. R. Pfeifer, M. Lungarella, F. Iida, Self-organization, embodiment, and biologically inspired robotics, *Science* **318**, 1088-1093 (2007).

8. L. M. Kamp, M. Zanaty, A. Zareei, B. Gorissen, R. J. Wood, K. Bertoldi, Reprogrammable sequencing for physically intelligent under-actuated robots, arXiv:2409.03737 [cs.RO], 2024.

9. S. Collins, A. Ruina, R. Tedrake, M. Wisse, Efficient bipedal robots based on passive-dynamic walkers, *Science* **307**, 1082-1085 (2005).

10. F. Stella, M. Achkar, C. D. Santina, J. Hughes, Paws: A synergy-based robotic quadruped leveraging passivity for robustness and behavioural diversity, 10.21203/rs.3.rs-3195331/v1 [Preprint], 2023.

11. Y. Zhao, Y. Chi, Y. Hong, Y. Li, S. Yang, J. Yin, Twisting for soft intelligent autonomous robot in unstructured environments, *Proceedings of the National Academy of Sciences* **119**, e2200265119 (2022).

12. Y. Xi, T. Marzin, R. B. Huang, T. J. Jones, P.-T. Brun, Emergent behaviors of buckling-driven elasto-active structures, *Proceedings of the National Academy of Sciences* **121**, e2410654121 (2024).

13. M. H. Raibert, *Legged robots that balance* (MIT press, 1986).

14. A. J. Ijspeert, A. Crespi, D. Ryczko, J.-M. Cabelguen, From swimming to walking with a salamander robot driven by a spinal cord model, *Science* **315**, 1416-1420 (2007).

15. K. McDonald, T. Ranzani, Hardware methods for onboard control of fluidically actuated soft robots, *Frontiers in Robotics and AI* **8** (2021).

16. M. Wehner, R. L. Truby, D. J. Fitzgerald, B. Mosadegh, G. M. Whitesides, J. A. Lewis, R. J. Wood, An integrated design and fabrication strategy for entirely soft, autonomous robots, *Nature* **536**, 451-455 (2016).

17. B. Gorissen, E. Milana, A. Baeyens, E. Broeders, J. Christiaens, K. Collin, D. Reynaerts, M. De Volder, Hardware sequencing of inflatable nonlinear actuators for autonomous soft robots, *Advanced Materials* **31**, 1804598 (2019).

18. D. Drotman, S. Jadhav, D. Sharp, C. Chan, M. T. Tolley, Electronics-free pneumatic circuits for controlling soft-legged robots, *Science Robotics* **6**, eaay2627 (2021).

19. L. C. van Laake, J. de Vries, S. Malek Kani, J. T. B. Overvelde, A fluidic relaxation oscillator for reprogrammable sequential actuation in soft robots, *Matter* **5**, 2898-2917 (2022).

20. S. Conrad, J. Teichmann, P. Auth, N. Knorr, K. Ulrich, D. Bellin, T. Speck, F. J. Tauber, 3d-printed digital pneumatic logic for the control of soft robotic actuators, *Science Robotics* **9**, eadh4060 (2024).

21. D. J. Preston, P. Rothemund, H. J. Jiang, M. P. Nemitz, J. Rawson, Z. Suo, G. M. Whitesides, Digital logic for soft devices, *Proceedings of the National Academy of Sciences* **116**, 7750-7759 (2019).

22. N. Vasios, A. J. Gross, S. Soifer, J. T. B. Overvelde, K. Bertoldi, Harnessing viscous flow to simplify the actuation of fluidic soft robots, *Soft Robotics* **7**, 1-9 (2020). PMID: 31070518.

23. H. Nabae, E. Kitamura, Self-excited valve using a flat ring tube: Application to robotics, *Frontiers in Robotics and AI* **9** (2022).

24. P. Rothemund, A. Ainla, L. Belding, D. J. Preston, S. Kurihara, Z. Suo, G. M. Whitesides, A soft, bistable valve for autonomous control of soft actuators, *Science Robotics* **3**, eaar7986 (2018).

25. W.-K. Lee, D. J. Preston, M. P. Nemitz, A. Nagarkar, A. K. MacKeith, B. Gorissen, N. Vasios, V. Sanchez, K. Bertoldi, L. Mahadevan, G. M. Whitesides, A buckling-sheet ring oscillator for electronics-free, multimodal locomotion, *Science Robotics* **7**, eabg5812 (2022).

26. C. J. Decker, H. J. Jiang, M. P. Nemitz, S. E. Root, A. Rajappan, J. T. Alvarez, J. Tracz, L. Wille, D. J. Preston, G. M. Whitesides, Programmable soft valves for digital and analog control, *Proceedings of the National Academy of Sciences* **119**, e2205922119 (2022).

27. O. D. Yirmibeşoğlu, T. Oshiro, G. Olson, C. Palmer, Y. Mengüç, Evaluation of 3d printed soft robots in radiation environments and comparison with molded counterparts, *Frontiers in Robotics and AI* **6** (2019).

28. M. Dunbabin, L. Marques, Robots for environmental monitoring: Significant advancements and applications, *IEEE Robotics Automation Magazine* **19**, 24-39 (2012).

29. J. L. Casper, M. Micire, R. R. Murphy, Issues in intelligent robots for search and rescue, *Unmanned Ground Vehicle Technology II*, G. R. Gerhart, R. W. Gunderson, C. M. Shoemaker, eds., International Society for Optics and Photonics (SPIE, 2000), vol. 4024, pp. 292 – 302.

30. H. Yasuda, P. R. Buskohl, A. Gillman, T. D. Murphey, S. Stepney, R. A. Vaia, J. R. Raney, Mechanical computing, *Nature* **598**, 39–48 (2021).

31. H. Tsukagoshi, A. Kitagawa, K. Tambo, H. Chiba, A fluid self-excited oscillation peculiar to flat ring tube and its application to wearable robots, *Proceedings 2007 IEEE International Conference on Robotics and Automation* (2007), pp. 3138–3139.

32. D. Gazit, A. L. Dranger, Apparatus and method for providing inflated undulating figures, US6186857B1 [Patent], 1997.

33. K. Luo, P. Rothemund, G. M. Whitesides, Z. Suo, Soft kink valves, *Journal of the Mechanics and Physics of Solids* **131**, 230-239 (2019).

34. M. T. Tolley, R. F. Shepherd, B. Mosadegh, K. C. Galloway, M. Wehner, M. Karpelson, R. J. Wood, G. M. Whitesides, A resilient, untethered soft robot, *Soft Robotics* **1**, 213-223 (2014).

35. A. Pikovsky, M. Rosenblum, J. Kurths, *Synchronization: A Universal Concept in Nonlinear Sciences*, Cambridge Nonlinear Science Series (Cambridge University Press, 2001).

36. G. Vantomme, L. C. M. Elands, A. H. Gelebart, E. W. Meijer, A. Y. Pogromsky, H. Nijmeijer, D. J. Broer, Coupled liquid crystalline oscillators in huygens' synchrony, *Nature Materials* **20**, 1702-1706 (2021).

37. Y. Wu, J. K. Yim, J. Liang, Z. Shao, M. Qi, J. Zhong, Z. Luo, X. Yan, M. Zhang, X. Wang, R. S. Fearing, R. J. Full, L. Lin, Insect-scale fast moving and ultrarobust soft robot, *Science Robotics* **4**, eaax1594 (2019).

38. F. R. Walther, Flight behaviour and avoidance of predators in thomson's gazelle (gazella thomsoni guenther 1884), *Behaviour* **34**, 184–221 (1969).

39. Z. Xiong, Y. Su, H. Lipson, Fast untethered soft robotic crawler with elastic instability, *2023 IEEE International Conference on Robotics and Automation (ICRA)* (2023), pp. 2606–2612.

40. R. Baines, S. K. Patiballa, J. Booth, L. Ramirez, T. Sipple, A. Garcia, F. Fish, R. Kramer-Bottiglio, Multi-environment robotic transitions through adaptive morphogenesis, *Nature* **610**, 283-289 (2022).

41. V. Braitenberg, *Vehicles: Experiments in Synthetic Psychology* (The MIT Press, 1986).

42. A. Comoretto, H. A. H. Schomaker, J. T. B. Overvelde, Physical synchronization of soft self-oscillating limbs for fast and autonomous locomotion: replication package, https://doi.org/10.5281/zenodo.14055942, 2025.

43. M. Arfaee, J. Kluin, J. T. B. Overvelde, Modeling the behavior of elastic pouch motors, *2023 IEEE International Conference on Soft Robotics (RoboSoft)* (2023), pp. 1–6.

44. Y. Zhai, A. D. Boer, J. Yan, B. Shih, M. Faber, J. Speros, R. Gupta, M. T. Tolley, Desktop fabrication of monolithic soft robotic devices with embedded fluidic control circuits, *Science Robotics* **8**, eadg3792 (2023).

45. L. C. van Laake, A. Comoretto, J. T. B. Overvelde, On the coexistence of pressure regulation and oscillation modes in soft hysteretic valves, *Journal of Fluids and Structures* **126**, 104090 (2024).

46. Wikipedia contributors, Standard litre per minute — Wikipedia, the free encyclopedia, [Online; accessed 24-January-2024], 2023.

47. B. Van Raemdonck, E. Milana, M. De Volder, D. Reynaerts, B. Gorissen, Nonlinear inflatable actuators for distributed control in soft robots, *Advanced Materials* **35**, 2301487 (2023).

48. R. M. Alexander, Optimization and gaits in the locomotion of vertebrates, *Physiological Reviews* **69**, 1199-1227 (1989). PMID: 2678167.

49. R. M. Alexander, Walking and running, *The Mathematical Gazette* **80**, 262–266 (1996).

50. G. Mao, D. Schiller, D. Danninger, B. Hailegnaw, F. Hartmann, T. Stockinger, M. Drack, N. Arnold, M. Kaltenbrunner, Ultrafast small-scale soft electromagnetic robots, *Nature Communications* **13**, 4456 (2022).

51. X. Ji, X. Liu, V. Cacucciolo, M. Imboden, Y. Civet, A. E. Haitami, S. Cantin, Y. Perriard, H. Shea, An autonomous untethered fast soft robotic insect driven by low-voltage dielectric elastomer actuators, *Science Robotics* **4**, eaaz6451 (2019).

52. M. Duduta, D. R. Clarke, R. J. Wood, A high speed soft robot based on dielectric elastomer actuators, *2017 IEEE International Conference on Robotics and Automation (ICRA)* (2017), pp. 4346–4351.

53. T. Park, Y. Cha, Soft mobile robot inspired by animal-like running motion, *Scientific Reports* **9**, 14700 (2019).

54. R. Chen, Z. Yuan, J. Guo, L. Bai, X. Zhu, F. Liu, H. Pu, L. Xin, Y. Peng, J. Luo, L. Wen, Y. Sun, Legless soft robots capable of rapid, continuous, and steered jumping, *Nature Communications* **12**, 7028 (2021).

55. J. Zhao, J. Zhang, D. McCoul, Z. Hao, S. Wang, X. Wang, B. Huang, L. Sun, Soft and fast hopping–running robot with speed of six times its body length per second, *Soft Robotics* **6**, 713-721 (2019). PMID: 31553262.

56. T. Umedachi, V. Vikas, B. A. Trimmer, Softworms: the design and control of non-pneumatic, 3d-printed, deformable robots, *Bioinspiration Biomimetics* **11**, 025001 (2016).

57. X. Huang, K. Kumar, M. K. Jawed, A. M. Nasab, Z. Ye, W. Shan, C. Majidi, Chasing biomimetic locomotion speeds: Creating untethered soft robots with shape memory alloy actuators, *Science Robotics* **3**, eaau7557 (2018).

58. M. A. Robertson, J. Paik, New soft robots really suck: Vacuum-powered systems empower diverse capabilities, *Science Robotics* **2**, eaan6357 (2017).

59. W. Hu, G. Z. Lum, M. Mastrangeli, M. Sitti, Small-scale soft-bodied robot with multimodal locomotion, *Nature* **554**, 81-85 (2018).

60. C. A. Aubin, R. H. Heisser, O. Peretz, J. Timko, J. Lo, E. F. Helbling, S. Sobhani, A. D. Gat, R. F. Shepherd, Powerful, soft combustion actuators for insect-scale robots, *Science* **381**, 1212-1217 (2023).

61. J. Liang, Y. Wu, J. K. Yim, H. Chen, Z. Miao, H. Liu, Y. Liu, Y. Liu, D. Wang, W. Qiu, Z. Shao, M. Zhang, X. Wang, J. Zhong, L. Lin, Electrostatic footpads enable agile insect-scale soft robots with trajectory control, *Science Robotics* **6**, eabe7906 (2021).

62. Y. Tang, Y. Chi, J. Sun, T.-H. Huang, O. H. Maghsoudi, A. Spence, J. Zhao, H. Su, J. Yin, Leveraging elastic instabilities for amplified performance: Spine-inspired high-speed and high-force soft robots, *Science Advances* **6**, eaaz6912 (2020).

Acknowledgments

We thank all members of our Soft Robotic Matter Group for the invaluable discussions. We thank Niels Commandeur for technical support, Sergio Picella for the input on the analytical model, and Corentin Coulais and Said RK Rodríguez for the constructive feedback. **Funding:** J.T.B.O. acknowledges the European Union's 2020 ERC-STG under grant agreement No. 948132. This work is part of the Dutch Research Council (NWO) and was performed at the research institute AMOLF. **Authors contributions:** A.C. and J.T.B.O. proposed and developed the research idea; A.C. designed and fabricated the devices; A.C. and H.A.H.S. performed

the experiments; A.C. and H.A.H.S. performed the data analysis; A.C. created the figures and videos; A.C. and J.T.B.O. wrote the manuscript; A.C., H.A.H.S., and J.T.B.O. revised the manuscript; J.T.B.O. supervised the research. **Competing interests:** A.C., H.A.H.S., and J.T.B.O. declare no competing interests. **Data and materials availability:** All data is available on Zenodo (*42*).

Supplementary Materials

The PDF file includes:

Materials and Methods

Supplementary Text

Figs. S1 to S27

Tables S1 to S4

Captions for Movies S1 to S7

References *(43-62)*

Other Supplementary Material for this manuscript includes the following:

Movies S1 to S7

Science
AAAS

Supplementary Materials for

Physical synchronization of soft self-oscillating limbs for fast and autonomous locomotion

Alberto Comoretto, Harmannus A.H. Schomaker, Johannes T.B. Overvelde

Corresponding author: overvelde@amolf.nl

The PDF file includes:

Materials and Methods

Supplementary Text

Figs. S1 to S27

Tables S1 to S4

Captions for Movies S1 to S7

References

Other Supplementary Material for this manuscript includes the following:

Movies S1 to S7

Materials and Methods

For brevity, we refer to the individual self-oscillating limb as the 'actuator' and to the locomoting robots as 'robots'. We describe the manufacturing procedure of actuators and robots in Section M1. The details of the experimental setups are reported in Section M2. In Section M3, we describe our pipeline for the numerical analysis of the high-speed recordings data.

M1 Manufacturing

The silicone tube actuator is composed of only two parts, a rigid holder and a soft tube, resulting in a three-step manufacturing procedure (Fig. S1). The thermoplastic polyurethane (TPU) pouch actuator, despite requiring more distinct parts than the silicone tube actuator, also follows a relatively straightforward manufacturing procedure (Fig. S2). The minimalistic design of the actuators results in a straightforward assembly of the tethered and untethered robots (Fig. S3).

Silicone tube actuator manufacturing

We 3D-print the rigid holder with the desired clamping distance d (Fig. S1A). Throughout our study, we chose the material VeroClear RGD810 (in combination with support material SUP705) using the Stratasys Eden260VS/VS PolyJet printer to achieve high precision. Similar results can be obtained with cheaper materials, e.g. PLA, using FDM 3D-printers such as the Ultimaker3. We press-fit the tube (internal diameter D_i and thickness t) in the left hole of the holder, and we mark the desired length l on the tube with a permanent marker (Fig. S1B). We press-fit the right side of the tube, making sure that the mark on the tube is aligned with the top surface of the holder (Fig. S1C). We estimate a total material cost of ~ 10 cents for an actuator with $l = 36\,\mathrm{mm}$, $D_i = 2.5\,\mathrm{mm}$, $t = 0.4\,\mathrm{mm}$, and $d = 12\,\mathrm{mm}$, with the holder printed in PLA (~ 2.7 cents) and the tube manufactured by Rubbermagazijn (~ 7.3 cents, since it is currently sold for 1.13 € per meter, and we require $\sim 65\,\mathrm{mm}$). A manufactured sample is shown in Figure S1D-F. Snapshots of the manufacturing

procedure are reported in Figure S1G-O.

TPU pouch actuator manufacturing

We take two TPU sheets (Ecoseal™ Film T150 85A, Rivertex) with thickness $0.15\,\mathrm{mm}$ and two TPU Festo™ tubes (PUN-6X1-BL) with external diameter $6\,\mathrm{mm}$ and length $10\,\mathrm{mm}$ (Fig. S2A). We seal the two sheets along two parallel lines of length $L+10\,\mathrm{mm}$, with L the desired length of the actuator, placed at a distance W, which is the width of the actuator. Throughout our study, we used actuators with $L = 80\,\mathrm{mm}$ and $W = 10\,\mathrm{mm}$. To heat-seal the two sheets, we use the printer Felix Tec 4, with a custom-made head, previously used by our group for similar sealing purposes (*43*). The head is equipped with a spherical nozzle that heats up and with an internal spring that allows for an even sealing of the sheets along the two lines. Note that we place a silicone mat between the bottom sheet and the print bed and oven paper between the top sheet and the hot head. The G-code sent to the printer is based on an Adobe Illustrator file containing the two parallel lines with desired length and distancing (red lines, Fig. S2B).

After sealing, we cut away the residual material using a scalpel. We insert the two TPU Festo™ tubes in the two open sides of the pouch, heat sealing the sheets to the tubes with a soldering iron at 300° so that the free length of the pouch tube is L (Fig. S2C). Finally, we insert Luer™ connectors (MLRL007-1 Male Luer to 500 Series Barb 3/32" 2.4 mm with Lock Ring FSLLR-3) in both Festo™ tubes to ease future connection in setups and robots (Fig. S2D). The actuator weights $0.88\,\mathrm{g}$ without the two Luer™ connectors, and $2.65\,\mathrm{g}$ with the connectors mounted. An example sample with $L = 80\,\mathrm{mm}$ and $W = 10\,\mathrm{mm}$, when not pressurized, has low bending stiffness and doesn't display multistability (Fig. S2E). Finally, we connect the inlet to a holder that is fixed to a base with a 55° angle, and the outlet to a holder that is fixed in position on the base, but free to rotate (Fig. S2F). Snapshots of the manufacturing procedure are reported in Figure S2G-R.

Tethered robot manufacturing

The body of the tethered robot is monolithic, and it acts both as a structural element to keep the four limbs in place and as the fluidic circuit to couple the four limbs so that they synchronize in-phase. The top view of the body (Fig. S3A) displays the inner channels of diameter $3\,\mathrm{mm}$ and length $\sim 15\,\mathrm{mm}$ that link the inlet to the four limbs connectors (Fig. S3B). We 3D-printed the body with the rigid material VeroClear RGD810, using the Stratasys Eden260VS/VS printer. We used the support material SUP705, which we then dissolved by placing the print in a 5% KOH solution in 20L of water. However, one could choose to 3D-print the robot's body with soft materials like TPU, given the monolithic design (*44*).

To reach the higher frequencies for the tethered robot, we implemented three design changes to the self-oscillating limb of Figure 1 and Figure 2. In Section S1, we explain in detail how such changes affect the frequency of the limbs and the speed of the robot. The three implemented changes are the following.

- We introduced an asymmetry in the design of the holder, placing the inlet higher than the outlet at a height h. We studied the influence of this parameter by testing samples with different asymmetry heights. In Figure S11D,E,F, we report the resulting frequency, stroke, and product between frequency and stroke for various heights. For the robot, we chose $h = 6\,\mathrm{mm}$ as it maximizes the product of frequency and stroke of the limb and, therefore, the theoretical speed that the robot can reach.

- We scaled down the tube (including the inlet-outlet distance d and the asymmetry height h) by a factor ~ 0.8. The tube in Figure 1 and Figure 2 has inner diameter $2.5\,\mathrm{mm}$ and thickness $0.4\,\mathrm{mm}$, while the updated tube has inner diameter $2\,\mathrm{mm}$ and thickness $0.3\,\mathrm{mm}$. Scaling down the tube by a factor $k \approx 0.8$ decreases the volume of air required for the kink to travel forward in one cycle by a factor $k^3 \approx 0.512$. Therefore, in principle, this factor approximately doubles $(1/0.512)$ the frequency of oscillation, as it halves the time required for the kink to travel, given the same inflow.

- In addition to adding asymmetry and scaling down the tube, we shortened it (so, shorter than the 0.8-scaled-down length) by another factor 0.65.

Each limb holder in the tethered robot is characterized by three parameters: the inclination α from the vertical, the distancing d, and the height h between the connector and the outlet holder (Fig. S3C). The holders of our robot are characterized by $\alpha = 30°$, $d = 7.8\,\mathrm{mm}$, and $h = 3.9\,\mathrm{mm}$. Each limb is mounted on the robot with a three-step process. The silicone tube (Rubbermagazijn) with inner diameter $2\,\mathrm{mm}$ and thickness $0.3\,\mathrm{mm}$ is fitted over the limb connector (Fig. S3D). A TPU Festo™ tube is fitted over the silicone tube to guarantee air-tightness (Fig. S3E). The silicone tube is press-fitted in the outlet holder, making sure that the actuator length is $l = 18\,\mathrm{mm}$. The remaining part of the tube is inserted in the horizontal holder so that the output flow doesn't create horizontal thrust effects that would otherwise contribute to the locomoting behavior of the robot (Fig. S3F).

Untethered robot manufacturing

The design of the untethered robot is modular, as displayed by the exploded render in Figure S3G. Each module is 3D-printed in PLA (BASF Ultrafuse PLA filament, color neutral, 2.85 mm) with the Ultimaker3 printer. The main body (red) has a LEGO®-like design so that all the other modules can be inserted or screwed on it. We fix the pumps holder (orange) and the on/off switch holder (yellow) on top of the main body. On the bottom, we fix the limbs' inlets holder (purple) with a $55°$ angle to the main body surface, same as in the case of the single actuator in Figure S2F. We insert the outlet holders (pink) on the green axis without tightening the screws so they rotate freely. We insert the female Luer connector (FTLLB230-1 Thread Style Panel Mount 1/4-28 UNF to 200 series 1/8" 3.2 mm) on both inlet and outlet holders to interface with the actuator's male connector. Finally, the balance limbs (blue) are screwed into the front side of the robot.

We insert the two $3\,\mathrm{V}$ mini air pumps (YYPN20-3M) in the holder. Each pump is independently connected to a pouch actuator through a silicone tube (inner diameter $2\,\mathrm{mm}$, length $80\,\mathrm{mm}$). We place a LiPo battery (Carson 500608131 Lipo-Akku 3.7V 380mAh) using Velcro adhesives. The pumps are connected to the LiPo through an on/off switch. The phototactic version of the untethered robot is equipped with two photoresistors (GL5528 LDR) and two transistors (BC546A) to detect light and activate the associated pump.

The complete schematics of the fluidic and electrical connections for the tethered, untethered, and phototactic robots are reported in Figure S4, highlighting their minimalistic design.

M2 Experimental setups

In this Section, we describe the setups that we use for our experimental campaigns. We use combinations of four setups, depending on the goal of each specific experiment. The *fluidic setup* is used wherever we need to control and acquire data of relevant fluidic quantities such as pressure and flow. The *high-speed recording setup* is used wherever imaging of the high-frequency oscillating actuator is needed. The *force-displacement setup* is used in the experiments where we constrain the actuator between fixed plates and where we control the bending angle of the tubes. The *torque-angle setup* is used in the experiments where we control the bending angle of the tubes while measuring the applied torque. The *ArUco tracking setup* is used whenever we are interested in the position and speed of the locomoting robots.

Fluidic setup

The fluidic setup, previously used by our group (*19, 45*) for similar acquisition purposes, is a custom-made acquisition setup based on the National Instruments IN USB-6212 input/output board and custom-made software. The setup has two analog output ports, which control the proportional pressure regulator (Festo™ VEAB-L-26-D18-Q4-V1-1R1) and the proportional flow control valve (Festo™ VEMD-L-6-14-20-D21-M5-1-R1-V4). Both regulators are connected to an upstream precision pressure regulator (Festo™ LRP-1/4-10). The setup has multiple analog input ports, which read the voltage output of pressure and flow sensors. The pressure sensors used throughout our study are the NXP MPX5100DP to read up to $100\,\mathrm{kPa}$, and the NXP MPX4250DP to read up to $250\,\mathrm{kPa}$. To measure pressures in the actuators of the hopping untethered robot, we used more compact pressure sensors (Honeywell 015PDAA5). We used the airflow sensor Honeywell AWM5104 to measure mass flow up to 20 standard liter per minute (SLPM). The regulators and sensors are summarized in Table S4. To remove sensor noise, we filter all acquired raw data with the MATLAB function

`smooth` with `loess` method. The connection between the various parts of the setup (regulators, sensors, and samples) is done using a combination of silicone tubes (Rubbermagazijn 2x4mm and 3x6mm), Festo™ tubes (PUN-6X1-BL), and Luer™ connectors (male-female, Luer-to-barb, and T connectors). The setup is equipped with digital output ports, used to trigger the high-speed recording setup and the force-displacement setup.

The airflow sensor that we used (Honeywell AWM5104) measures mass flowrate in Standard Liter Per Minute (SLPM). To obtain airflow values in SI units, we first convert to liters per minute (*46*):

$$Q^{\mathrm{LPM}} = Q^{\mathrm{SLPM}} \cdot \frac{T_{\mathrm{gas}}}{273.15} \cdot \frac{14.504}{p_{\mathrm{gas}}}, \tag{1}$$

with the temperature of the gas $T_{\mathrm{gas}} = 295.65\,\mathrm{K}$ assumed to be equal to the temperature in our lab, and the pressure of the gas p_{gas} assumed atmospheric ($1.013\,25 \times 10^5\,\mathrm{Pa} = 14.696\,\mathrm{psi}$), since in all our experiments the tubes vent to atmosphere. Therefore, we obtain the flow in liters per minute as:

$$Q^{\mathrm{LPM}} = 1.068 \cdot Q^{\mathrm{SLPM}}, \tag{2}$$

and we convert to cubic meters per second as:

$$Q^{m^3/s} = \frac{1.068}{6 \cdot 10^4} \cdot Q^{\mathrm{SLPM}}. \tag{3}$$

Throughout the text, we reported flow rates in SLPM. In Table S1, we report the corresponding values in SI units obtained by applying Equation (3).

High-speed recording setup

The high-speed recording setup consists of the high-speed camera Phantom v4.2 with the lens Navitar f75mm / F1.8, together with the spotlight Nanlite FS-300B LED Bi-color. The camera is set to a 256x256 pixels resolution, acquisition rate of 4000 frames per second, and $10\,\mu\mathrm{s}$ shutter speed. The camera trigger is controlled through a digital signal sent by the fluidic setup to ensure synchronization of the acquisition of both setups. The camera continuously records frames and stores the $\sim 0.5\,\mathrm{s}$ before the trigger instant.

Force-displacement setup

The force-displacement setup consists of the tensile-testing machine Instron 5965, equipped with a static load cell (Instron 2530-100N) with $100\,\mathrm{N}$ capacity. We used the machine in the displacement-control mode, storing force and displacement values. We trigger the starting of the test using a digital output from the fluidic setup, ensuring synchronization of the acquisition of both setups.

Torque-angle setup

The torque-angle setup consists of the microtorsion testing machine Instron MT1-E1 that controls the bending angle of the tube. At the same time, we measure the torque exerted on the tube with the load cell W-5510-T4 with torque capacity $0.225\,\mathrm{N\,m}$.

ArUco tracking setup

To measure the speed of each of our robots, we place an ArUco marker vertically on top of the robot. We record the robot sideways at a rate of 50 fps with the camera Canon EOS 850D equipped with the lens Canon f50mm / F1.8. For each frame of the videos, we detect the pixels associated with the four corners of the ArUco marker. We define the position of the robot as the average of the four detected corners.

To detect the ArUco marker, we use the following algorithm. We begin by initializing the standard ArUco marker detection parameters (`cv2.aruco.DetectorParameters_create`) and accessing a predefined dictionary of ArUco markers that correspond to the printed ArUco on the robot (`aruco.DICT_4X4_100`). The script opens a video file using OpenCV's video capture capabilities (`cv2.VideoCapture`). This opens a VideoWriter object to save the processed output.

As the script processes the video, it iterates through each frame, cropping off the nonessential parts of the video. These are the areas that do not have an ArUco throughout the entire video. Note that this cropping procedure is important in the side view experiments as the robot sits on a wooden table. In fact, the table would interfere with the tracking since the texture of the wood can cause false positives in the ArUco detection. Each

cropped frame is converted to the LAB color space to improve local contrast using Contrast-Limited Adaptive Histogram Equalization (`cv2.createCLAHE`). The script employs the `cv2.aruco.detectMarkers` function to detect the four corners of the ArUco markers in each frame. The script applies additional image processing methods if the initial detection attempt fails. For its second attempt, it uses a Gaussian blur (`cv2.GaussianBlur`) to soften the edges of the ArUco. For its third attempt, it employs a contrast and brightness adjustment to enhance the image using `cv2.convertScaleAbs`. In the rare cases where the four corners of the marker are not detected, the script is designed to use a fallback method, employing manual detection.

M3 Numerical analysis of the video recordings

We develop an algorithm to extrapolate quantitative information from the high-speed videos of the actuator that self-oscillates at high frequency. The Python algorithm implements, for each frame `iFrame` of the recording, *detection* of the pixels associated with the edge of the tube and *clustering* of the outer and inner edges. Using MATLAB code, we extrapolate the *center line*, *local width*, *kink location along the center line*, *kink width*, *actuator's tip*, *kink distance*, and *kink velocity*.

Edge detection and clustering

Silicone tube actuator. For each frame of the high-speed recordings, we increase the resolution using the command `cv.resize`. We convert to greyscale (`cv.cvtColor`) and apply Gaussian blur (`cv.gaussianBlur`). We perform Canny edge detection to identify pixels that separate bright areas from dark areas (`cv.Canny`). Note that an appropriate experimental setting of the lighting conditions, with the bright, illuminated tube on a dark background, is essential for successful edge detection.

For each frame, after edge detection, we have a matrix with `False` values, except for the `True` pixels associated with the edges. To extrapolate valuable information, we cluster the inner and outer edges, obtaining two separate lists of points associated with the two edges. To do so, we visually define a vertical threshold

`threshold_y` for the image to exclude pixels underneath it. We visually define a value `zero_x` representing a vertical line between the inlet and the outlet sides of the tube. We call the two sizes of the image `width` and `height`. We define the function `dfs` for a recursive depth-first search to find the connected pixels of the two clusters.

```
def dfs(x, y, visited, cluster):
    # Mark the pixel as visited and add it to the cluster
    visited.add((x, y))
    cluster.append((x, y))

    # Define the neighbors to visit
    neighbors = [(x-1, y), (x+1, y), (x, y-1), (x, y+1), (x-1, y-1), (x-1, y+1), (x+1, y-1), (x+1, y+1) ]

    # Visit each unvisited neighbor
    for nx, ny in neighbors:
        if (nx, ny) not in visited and 0 <= nx < width and 0 <= ny < height and ny <= start_y and table[ny, nx]:
            dfs(nx, ny, visited, cluster)
```

We find the starting index for the search, and we execute the recursive depth-first search.

```
# Find the starting y-coordinate for the outer edge
for y in range(0, height):
    for x in range(0, width):
        if table[y, x] > 0:
            start_y = y
            start_x = x

# Find the outer edge cluster
visited = set()
outer_edge = []
dfs(start_x, start_y, visited, outer_edge)
```

Note that, at this point, it is not ensured that the pixels associated with the edges are connected. Occasionally, we observe the pixels being disconnected at the kink, which is a challenging area of the image for the Canny detection algorithm. For this reason, we perform the recursive depth-first search twice, first starting from the left of the image, and then from the right. This ensures that the edges are complete. We then repeat this clustering process for the inner edge.

TPU pouch actuator. The detection algorithm described so far proved challenging in the case of the TPU pouch actuator, given its sharper kinks. For this reason, we implemented a slightly different algorithm

so that the edges of the TPU pouch actuator can reliably be detected for each frame. Similar to the previous algorithm, we open the video (`OpenCV`). With a loop, we process the data of the individual frames. For each frame, we perform a series of image-processing steps. We resize (using `cv.resize`) to enhance the number of pixels and therefore smooth the edges of the actuator. Second, we convert to grayscale (`cv.rgb2gray`) to highlight the difference between the black background and the white actuator. Third, we create a masking circle on the frame using `cv.circle`. This circle masks the actuator's holders, leaving only the TPU pouch tube visible. We combine this mask with the original image using `cv.bitwise_and` for selective focus on the TPU section of the actuator. Fourth, the script further processes each image by applying Gaussian blur (`cv.GaussianBlur`), smoothing the edges of the TPU and the background (specifically the kink, where the actuator folds onto itself). Fifth, we perform thresholding with `cv.threshold` to obtain a binary distinction between the TPU actuator and the background. Lastly, we use contour detection (`cv.findContours`) to extract the edge pixels between the TPU actuator and the background.

To cluster the inner and outer contours of the TPU pouch actuator, we employ the following custom algorithm to filter and connect the coordinates of the extracted contours. We start by identifying the start/end point of the outer contour as the coordinate with the maximum x and y positions. This is followed by a loop that sets the start as a reference and matches this with the closest coordinate in the list of all the contours. If the closest matching curve is within a set threshold (20 pixels), the algorithm connects the coordinates to form the curves, updates the newfound coordinate as a reference, and removes it from the initial list. Once no connecting coordinate is found, the same is repeated for the inner contour. The end result is a set of two sequences of coordinates that represent the inner and outer edges of the TPU actuator in the image.

```
# Identify the initial reference point
ref_point_idx = np.argmax(np.sum(coords, axis=1))
ref_point = coords[ref_point_idx]

# Function to compute the distance between two points
def compute_distance(pt1, pt2):
    return np.sqrt(np.sum((pt1 - pt2)**2))

connected_coords_outer = [ref_point]
# Remove the reference point from the array
```

```
coords = np.delete(coords, ref_point_idx, axis=0)

while len(coords) > 0:
    # Compute distances from the current ref_point to all other points
    distances = np.array([compute_distance(ref_point, pt) for pt in coords])

    # Index of the closest point
    min_distance_idx = np.argmin(distances)

    # Check if the closest point is further than 20
    if distances[min_distance_idx] > 20:
        break

    # Append the new coordinate and update the reference point
    ref_point = coords[min_distance_idx]
    connected_coords_outer.append(ref_point)

    # Remove the selected coordinate from the array
    coords = np.delete(coords, min_distance_idx, axis=0)
    # select new reference point index
    ref_point_idx = np.argmax(np.sum(coords, axis=1))
```

Definition of quantities of interest

Through the edge detection and clustering process, we obtained the two lists of the outer and inner edges' history in time. Each element of the list is an array with the points associated with the edge at the instant of interest. For each of these arrays, we extrapolate the following quantities of interest, reported in Figure S5 for visual clarification:

- the *rearranged edges*, defined as the same points of the detected clusters, but rearranged using a single linkage hierarchical clustering with leaf order optimization;
- the cluster of the *closest points in the inner edge* to the outer edge, defined as the ensemble of points in the inner edge that minimize the Euclidean distance to each point in the outer edge;
- the *center line* cluster as the ensemble of the average values between each pair of points belonging to the ordered outer edge and their closest points in the inner edge;

- the *local width* of the tube, defined as the Euclidean distance between each pair of points, one belonging to the ordered outer edge and one to its closest point in the inner edge;
- the *center line reference frame*, defined as the cumulative sum of the distances between consecutive points belonging to the center line;
- the *actuator's tip*, defined as the point on the outer edge with the maximum y-coordinate in the x-y reference frame;
- the *kinks' location* along the center line, defined as the two local minima of the local width over the center line coordinate;
- the *kinks' position* in the x-y reference frame, defined as the points of the outer edge associated with the kinks' locations;
- the *kinks' width*, defined as the local width of the tube at the kinks' locations.

We define, for each instant t_i:

- the *kink distance* as the Euclidean distance between the kink position in the x-y plane at time t_i and the kink position in the x-y plane at the reference time t_{ref}, which is arbitrary defined as the instant when the non-dominant kink changes role and becomes dominant;
- the *kink velocity* as the finite difference of the kink distance. Note that the term *velocity* here is not used according to the classical meaning, since it expresses the rate of change of the distance of the kink and *not* the rate of change of its position.

Supplementary Text

The development and the results of the mass-spring model are reported in Section S1. Additional experiments on the self-oscillating limbs are reported in Section S2. In Section S3, we study the kink formation in thin tubes undergoing bending. Additional experiments on the locomoting robots are reported in Section S4. For brevity, we refer to the individual self-oscillating limb as the 'actuator' and to the locomoting robots as 'robots'.

S1 Mass-spring model of the self-oscillating behavior

To gain fundamental insight into the self-oscillating behavior, we developed a basic mass-spring model. In summary, from the model, we learn three fundamental reasons behind the self-oscillating behavior: i) the localized kinking of the tube is associated with a local nonlinear torque-angle curve under bending; ii) the local flow resistance increases when kinks are formed, leading to increased pressure before the kink; iii) the internal pressurization increases the torque required for kinking and unkinking. We will now proceed to elaborate in detail on the development of the model and on the results of the simulations.

Model description

We represent the tube as a series of point masses connected by linear and torsional springs, simulating both stretching and bending resistance (Fig. S6A). The tube is discretized into N point masses, each of mass m, connected by linear springs of rest length L_0 and spring constant k_s, and torsional springs with stiffness k_b. The positions of the nodes are denoted by $\mathbf{r}_i = (x_i, y_i)$ for $i = 1, 2, \ldots, N$. We implement the model using a non-dimensionalized framework to view the relative differences of the parameters in the equations and describe the qualitative behavior.

The dynamics of each node i are governed by Newton's second law:

$$m\frac{d^2\mathbf{r}_i}{dt^2} = \mathbf{F}_{\text{linear},i} + \mathbf{F}_{\text{torsional},i} - c\frac{d\mathbf{r}_i}{dt}, \tag{4}$$

where c is the damping coefficient, $\mathbf{F}_{\text{linear},i}$ is the net force due to linear springs, and $\mathbf{F}_{\text{torsional},i}$ is the net force due to torsional springs acting on node i.

The linear spring forces are calculated based on Hooke's law for adjacent nodes:

$$\mathbf{F}_{\text{linear},i} = -k_s \left[(\ell_{i,i-1} - L_0) \frac{\mathbf{r}_i - \mathbf{r}_{i-1}}{\ell_{i,i-1}} + (\ell_{i,i+1} - L_0) \frac{\mathbf{r}_i - \mathbf{r}_{i+1}}{\ell_{i,i+1}} \right], \tag{5}$$

where $\ell_{i,j} = \|\mathbf{r}_i - \mathbf{r}_j\|$ is the distance between nodes i and j.

The torsional spring forces arise from the resistance to bending between consecutive segments:

$$\mathbf{F}_{\text{torsional},i} = -k_b(\theta_i - \theta_0), \tag{6}$$

where θ_i is the angle at node i between segments $\mathbf{r}_i - \mathbf{r}_{i-1}$ and $\mathbf{r}_{i+1} - \mathbf{r}_i$, and θ_0 is the rest angle. In our case, the rest configuration is when the tube is straight, so $\theta_0 = \pi$. The angle θ_i is computed using:

$$\theta_i = \arctan 2 \left((\mathbf{r}_i - \mathbf{r}_{i-1}) \times (\mathbf{r}_{i+1} - \mathbf{r}_i), (\mathbf{r}_i - \mathbf{r}_{i-1}) \cdot (\mathbf{r}_{i+1} - \mathbf{r}_i) \right), \tag{7}$$

where $\times$ denotes the 2D cross product and $\cdot$ denotes the dot product.

Non-dimensionalization

To reduce the complexity of the equations, we non-dimensionalize the system using characteristic scales:

- length scale: the rest length of the linear springs, L_0;
- time scale: $t_0 = \sqrt{\frac{m}{k_s}}$;
- mass scale: the mass of each node, m.

We further define the non-dimensional variables as:

- non-dimensional position, with $\mathbf{r}$ being the dimensional position:

$$\mathbf{r}' = \frac{\mathbf{r}}{L_0}, \tag{8}$$

- non-dimensional time, with t being the dimensional time:

$$t' = \frac{t}{t_0}, \tag{9}$$

- non-dimensional velocity:

$$\mathbf{v}' = \frac{d\mathbf{r}'}{dt'} = \frac{t_0}{L_0}\frac{d\mathbf{r}}{dt}. \tag{10}$$

The non-dimensional parameters are:

$$\eta = \frac{k_b}{k_s L_0^2}, \quad \zeta = c\frac{t_0}{m}, \tag{11}$$

resulting in the equations of motion in non-dimensional form:

$$\frac{d^2\mathbf{r}'_i}{dt'^2} = \mathbf{F}'_{\text{linear},i} + \mathbf{F}'_{\text{torsional},i} - \zeta\frac{d\mathbf{r}'_i}{dt'}, \tag{12}$$

where the non-dimensional forces are calculated similarly to their dimensional counterparts but using non-dimensional variables. The non-dimensional linear spring forces are:

$$\mathbf{F}'_{\text{linear},i} = -\left[(\ell'_{i,i-1} - 1)\frac{\mathbf{r}'_i - \mathbf{r}'_{i-1}}{\ell'_{i,i-1}} + (\ell'_{i,i+1} - 1)\frac{\mathbf{r}'_i - \mathbf{r}'_{i+1}}{\ell'_{i,i+1}}\right], \tag{13}$$

where $\ell'_{i,j} = \|\mathbf{r}'_i - \mathbf{r}'_j\|$. The non-dimensional torsional spring forces are:

$$\mathbf{F}'_{\text{torsional},i} = -\eta(\theta_i - \pi), \tag{14}$$

with θ_i computed using the non-dimensional positions.

Assumption one: nonlinear bending stiffness

Since we model the system with a set of torsional springs and near-rigid bars (linear springs with high stiffness compared to the torsional springs), we experimentally characterize the behavior of the tube under controlled bending. This will inform us about the torque-angle curve of the kinking tube. We will transfer this information to the torque-angle curve of the non-dimensional torsional springs in the model.

We use a microtorsion testing machine (Instron MT1-E1) to increase the bending angle quasi-statically, at a rate of $130\,^\circ/\mathrm{min}$. At the same time, we measure the torque exerted on the tube (load cell W-5510-T4 with torque capacity $0.225\,\mathrm{N\,m}$), and we regulate pressure inside the tube with a Festo™ pressure regulator (details on the setups in Section M2). In Figure S8A, we report the measured torque-angle curve of the silicone tube (with inner diameter $2.5\,\mathrm{mm}$, thickness $0.4\,\mathrm{mm}$) for a pressure of $20\,\mathrm{kPa}$. In Figure S8B, we also report snapshots of the experiment at four angle values. We observe that the torque-angle curve is non-monotonic, displaying the negative-stiffness regime typical of snapping structures (parallel to the negative stiffness of the pressure-volume curves of non-linear inflatable elements (*47*), but in the torque-angle regime). While kinking, the tube goes through an unstable regime when bending stiffness is negative, displaying a peak and a valley (Fig. S8A, red and blue dots).

To qualitatively capture the experimentally observed non-monotonic mechanical behavior of the tube during the kinking process, we modeled the torque-angle curve $\mathbf{F}'_{\text{torsional},i}$ as a nonlinear function of the torque with respect to the bending angle θ:

$$\mathbf{F}'_{\text{torsional},i} = \beta_{(\theta)}. \tag{15}$$

We introduce a negative stiffness regime in $\beta_{(\theta)}$ by using interpolation techniques that allow us to specify the peaks and minima of the torque angle curve. This approach enables us to simulate the non-linear behavior of the tube when the kink forms, which is assumption one (Fig. S6B). We define a set of control points representing the desired torsional force values at specific angles. These points are determined by a vector of stiffness parameters $k_b = [\beta_0, \beta_1, \beta_2]$, corresponding to the torque at key angular positions. The torsional force function $\beta_{(\theta)}$ is constructed using a Piecewise Cubic Hermite Interpolating Polynomial (PCHIP), which ensures smoothness and monotonicity where required. The control points are given by:

$$\begin{aligned} \theta_{\text{data}} &= [0, 0.3, \tfrac{2\pi}{3}, 2\pi], \\ k_{b,\text{data}} &= [0, \beta_0, \beta_1, \beta_2]. \end{aligned} \tag{16}$$

Using these points, the bending stiffness function becomes:

$$\beta_{(\theta)} = \text{PCHIP}_{(\theta_{\text{data}}, k_{b,\text{data}})(\theta)}, \tag{17}$$

where PCHIP denotes the interpolation operator.

The negative stiffness regime in the $\beta_{(\theta)}$ curve introduces an unstable equilibrium at a bending angle of 0.3 (Fig. S6B). When the tube's ends are brought closer together, the bending angles at the nodes increase, and the system seeks to minimize its potential energy. The negative stiffness regime results in a sudden increase in the bending angle of an element (a kink) as the system moves towards the local energy minima. This phenomenon effectively models the kinking behavior observed when bending flexible tubes (*33*). To introduce the kink in our simulated system in the most natural way, we initialize the system in half a circle with a curvature where the stable equilibrium of the system does not have a kink; we then drive the outer ends of the system closer together to a point where the system kinks (Fig. S6C). After we bring the endpoints closer together, we fix their positions for the rest of the simulation. Mathematically, we defined a movement function for the first two nodes:

$$x_i'(t') = \begin{cases} v'_{\text{move}} \cdot t', & \text{if } t' \leq 400, \\ v'_{\text{move}} \cdot 400, & \text{if } t' > 400, \end{cases} \tag{18}$$

where $v'_{\text{move}} = \dfrac{4}{400}$ is the non-dimensional movement rate.

Assumption two: the local flow resistance increases at the kink location

In the case of the self-oscillating tube, we assume that the point of highest curvature acts as a dominant fluidic resistance in the tube (Fig. 2 in the main text, Fig. S20, and Fig. S21). This higher fluidic resistance will cause a pressure difference before and after the kink (point of highest curvature). As a result, the nodes on the side of the air inflow (left) up to and including the kink (point of highest curvature) will be under more pressure than the nodes on the other (right) side of the kink (Fig. S6D). In our model, we do not directly model the flow. Instead, we assume that the kink leads to infinite fluidic resistance.

Assumption three: pressurization of the tube increases the torque required for kinking and unkinking

Experimentally, we observe that the torque required to form a kink increases as the pressure in the tube increases (Fig. S8C,D). Mathematically, we represent this effect by introducing a stiffness multiplier, denoted as κ, which multiplies the baseline torque-angle curve (Fig. S6E). The torque-angle curves for nodes that are in a "pressurized" state (i.e., that are on the left to the kink, including the kink) are modified as follows:

$$\beta'_{(\theta)} = \kappa\, \beta_{(\theta)}, \tag{19}$$

where:

- $\beta'_{(\theta)}$ is the torque-angle curve for nodes under higher pressure.
- κ is the stiffness multiplier ($\kappa > 1$) representing the effect of pressure-induced stiffening.
- $\beta_{(\theta)}$ is the baseline torque-angle curve, as previously defined in Eq. (17).

Implementation of the three assumptions in the model

To incorporate these two assumptions into our numerical simulation, we perform the following steps.

1. Forming the kink: at the start of the experiment, we drive the fixed nodes closer together to form the kink (Fig. S6C). From $t' = 400$ onwards, we fix their positions for the rest of the simulation.
2. Kink detection: at each time step starting from $t' = 600$, we identify the node with the maximum deviation from the rest angle $\theta_0 = \pi$. This node corresponds to the location of the kink (red dot in Figure S6D).
3. Pressure-induced stiffening: once the kink is identified, we increase the bending stiffness of all nodes to the left of the kink (including the kink node) (Fig. S6D) by multiplying their torque-angle curve by κ (Fig. S6E).

4. Time-dependent stiffening: to approximately model the gradual effect of pressure buildup, we use a sigmoid function to smoothly transition the stiffness increase over time:

$$\kappa_{(t')} = 1 + \delta\kappa \cdot S_{\left(t' - t'_{\text{kink}}\right)}, \tag{20}$$

where:

- $\delta\kappa = \kappa_{\text{assigned}} - 1$ is the maximum scalar with which the force is multiplied. So, effectively, κ transitions smoothly from 1 to the assigned value κ_{assigned}. Note that in the remainder of the text, for simplicity, when we refer to the assigned stiffness multiplier, we use κ.
- t'_{kink} is the non-dimensional time when the kink is formed.
- $S_{(t')}$ is the generalized sigmoid function:

$$S_{(t')} = \frac{1}{1 + e^{-k(t' - x_0)}}, \tag{21}$$

with parameters k controlling the slope and x_0 the midpoint of the transition.

5. Updating torsional forces: the torsional spring forces for nodes i on the left of the kink $i <= i_{\text{kink}}$ are recalculated using the increased torque:

$$\mathbf{F}'_{\text{torsional},i} = -\kappa_{(t')}\, \beta_{(\theta_i - \pi)}, \quad \text{for} \;\; i <= i_{\text{kink}}. \tag{22}$$

6. Time-dependent softening: for the torsional spring force acting on the nodes on the right side of the kink, we use the inverse of Eq. (21) to smoothly transition back to the initial $\beta_{(\theta)}$ curve. t'_{kink} is updated to the t' where $i > i_{\text{kink}}$.

Results of the model

When we drive the inlet and the outlet closer together, a kink forms (Fig. S7A). At non-dimensional time $t' = 600$ (start), we enforce assumptions two and three, i.e., the stiffening of the springs on the left of the kink

(Fig. S7B). We observe the kink propagating along the simulated tube (Fig. S7C). Since assumption one also holds for the stiffer springs (that is, the stiffer springs are also non-linear in the torque-angle behavior), a new kink forms in the stiffer region of the tube (Fig. S7C, pink star). This kink will then travel again due to the stiffening, and the cycle repeats.

We visualize the evolution of the simulated system in the spatiotemporal domain (Fig. S7D), noticing the single kink with one angle at a high value (red) and all other angles at a low value (grey) until $t' = 600$. After switching on assumptions two and three, the system self-oscillates at a stable frequency (Fig. S7D). We look at the spatiotemporal signature of two consecutive oscillations in Figure S7E. For a short amount of time, two kinks exist simultaneously on the tube, in accordance with the experimentally observed behavior (Fig. 2 in the main text). The duration of this two-kink state is, however, shorter (in relation to the traveling duration) when compared with the experiments in Figure 2C. Indeed, in terms of this two-kink state duration, it seems that our model is capturing the dynamic, resonating case in Figure 2M. When the newly formed kink eventually becomes dominant, it will travel again in the next cycle.

These results confirm that the model captures the essential features of a self-oscillating tube, including kink formation, propagation, and spontaneous cyclic resetting. This stable self-sustained oscillatory behavior emerges from three experimentally proven assumptions. Note that this model still captures the oscillating behavior despite approximating the dynamics of the fluidics. In fact, for simplicity, we model a sudden increase in pressure as a consequence of the kink. However, in reality, the fluidic resistance would suddenly increase, and pressure would smoothly increase as a consequence. The variable pressure, given constant inflow, would follow the orifice dynamics (*45*), which we did not include in this coarse-grained model.

From this model, we also learn that when the stiffening of the pressurized section is not high enough, the kink does not travel along the tube. In fact, when the stiffness multiplier κ is low, up to 1.5 (Fig. S9A), the formed kink does not propagate along the tube (Fig. S9B,C,F,G). For $\kappa = 1.7$ we observe the kink traveling once, likely due to inertia effects, but subsequent oscillations are not sustained (Fig. S9D,H). When the stiffening is high enough (for $\kappa = 1.9$), the kink is able to travel, and a new kink forms when the previous

one reaches the critical position along the tube (Fig. S9E). This results in the system sustaining subsequent self-oscillations (Fig. S9I).

This key role of the pressure-induced stiffening in enabling the self-sustained oscillations is in line with experimental observations. In Figure S8D we report the experimental torque-angle curves of a thicker silicone tube with inner diameter $3\,\mathrm{mm}$ and thickness $1\,\mathrm{mm}$ for different pressurization levels. For this tube, assumption one still holds (the curves present a peak and a valley, and we observe the formation of a kink), and assumption two as well (the kink locally increases fluidic resistance). However, in contrast to the tubes used throughout the article, when controlling the input flow up to $20\,\mathrm{SLPM}$, we do not observe the kink traveling and the tube oscillating: this is the well-known static behavior of a kinked soft tube previously studied (*33*). With the observations from the model, we now have a better indication of why, in this specific case, the kink does not travel along the tube: the increase in the critical torque to induce kinking due to pressurization (from assumption three) is considerably lower than in the case of the softer tube (compare Fig. S8C with Fig. S8D). The stiffening effect is not sufficient to induce the kink wave, similar to the case of the model with κ up to 1.5 (Fig. S9A,B,C,F,G).

Practical information about the simulations

The parameters used in the simulations are:

- Number of nodes (including boundary nodes): $N = 17$.
- Dimensionless damping coefficient: $\zeta' = 0.4$.
- Dimensionless bending stiffness parameters: $\beta = [1.20, 0.1, 0.2]$.
- Sigmoid function parameters: $k = 5$, $x_0 = 1.5$.

To enhance computational efficiency, we utilized:

- Vectorization: leveraging NumPy's vectorized operations for array computations.

- Just-in-time compilation: using Numba's `@njit` decorator with `fastmath=True` to compile functions that are performance-critical, such as force calculations.

- Piecewise cubic hermite interpolating polynomial (PCHIP): implemented to model the nonlinear bending stiffness smoothly, using `scipy.interpolate.PchipInterpolator`.

The kink propagation was managed by updating an `extra_array` that keeps track of the state and timing of each node's stiffening and softening due to the kink. When a kink is detected at a node (based on a threshold angle deviation), the bending stiffness at that node is increased over time following the sigmoid function.

We followed the following steps for each simulation:

1. Initialization:

    - set initial positions along a half-circle and zero initial velocities;
    - initialize parameters and non-dimensional variables.

2. Time integration loop:

    - at each time step, compute linear and torsional forces;
    - update positions and velocities using the ODE solver;
    - apply boundary conditions;
    - update the bending stiffness at nodes affected by the kink.

3. Data recording: store positions, velocities, and other relevant variables for analysis.

4. Post-processing: analyze the results to observe the oscillatory behavior and the effect of the kink-induced stiffening.

S2 Actuator analysis

We aim to obtain an overview of the behavior of the actuator by studying i) the full-step actuation cycle, ii) the frequency dependencies of the silicone tube actuator, iii) the kinks' behavior in time, iv) the response under flow and pressure control, vi) the fluidic coupling of two actuators, vii) the frequency and stroke of the TPU pouch actuator compared to the silicone tube actuator, viii) the power consumption of the TPU pouch actuator, ix) the characterization of the TPU pouch actuator in terms of design parameters, and x) the constrained actuation of the TPU pouch actuator against an external load.

Full-step actuation cycle

Given the non-trivial behavior of our actuator, which displays kinks traveling on the continuity of the tube, the definition of the actuator tip is not straightforward. For each frame of the high-speed video of the oscillating tube (details on the recording setup in Section M2) we detect the outer edge of the tube (details on the algorithm in Section M3). We define the actuator tip as the point of the outer edge furthest from the horizontal axis of the reference frame defining the actuating plane (Fig. S10A). Note that this is equivalent to defining the actuator tip as the point on the outer edge closest to the surface on which the actuator will perform the full-step action. Importantly, if we rotate the actuating plane, the actuator tip is represented by another point in the plane (Fig. S10B).

The actuator tip trajectory in the actuating plane has different shapes depending on the amount of rotation of the actuating plane. We report three example cases for plane angle equal to $0°$, $15°$, and $30°$ in Figure S10C,D,E. Note that the actuator is in the non-resonating oscillation regime – the input airflow is 6.5 SLPM. Also, note that each trajectory is reported for two subsequent oscillation cycles. To find the value of the plane angle that optimizes the full-step cycle, we define a cost function as the ratio between the y-stroke and the x-stroke. These strokes are defined as the difference between the maximum and the minimum value of, respectively, the x-coordinates and the y-coordinates of the trajectory points. Therefore, qualitatively, the cost function is maximizing the 'effective' stance, so reducing the portion of the stance that is 'lost' by not

being in contact with the ground. The cost function shows a global minimum at $\sim 15°$ for inflow 6.5 SLPM and at $\sim 30°$ for inflow 16 SLPM (Fig. S10F).

To visually confirm that the full-step motion is optimized at such plane angles, we report the normalized x and y displacement of the actuator tip in time for the three example cases of plane angle equal to $0°$, $15°$, and $30°$ in Figure S10G,H,I. Note that non-optimized motions show either an anticipation (in the case of $0°$) or a delay (in the case of $30°$) of the y-motion. The optimized motion (at $15°$) is approaching the shape of an ideal full-step cycle (Fig. S10J), where the stance (increase in x displacement) is performed when the y displacement is low, and the swing (decrease in x displacement) when the y displacement is high.

Frequency dependencies of the silicone tube actuator

The oscillation frequency of the silicone tube actuator depends on various design parameters. For example, scaling a reference design (with $l = 36\,\mathrm{mm}$, $D_i = 2.5\,\mathrm{mm}$, $t = 0.4\,\mathrm{mm}$, and $d = 10\,\mathrm{mm}$) by a factor of ~ 0.8 results in an increase in the activation frequency by a factor ~ 1.4 for the 15 SLPM (resonant) case and ~ 2.1 for the 5 SLPM (non-resonant) case (Fig. S11A). In fact, scaling down the tube by a factor $k \approx 0.8$ decreases the volume of air required for the kink to travel forward in one cycle by a factor $k^3 \approx 0.512$. This is because we approximate the volume of air as a cylinder, with height being the distance covered by the kink and radius being the inner radius of the tube. Therefore, in principle, this factor approximately doubles $(1/0.512)$ the frequency of oscillation, as it halves the time required for the kink to travel, given the same inflow. As shown in the experimental results reported in Figure S11A, when the tube is not resonating, frequency indeed doubles from $\sim 40\,\mathrm{Hz}$ to $\sim 80\,\mathrm{Hz}$. Instead, in the dynamic resonating case, in practice, the frequency scales by a factor ~ 1.4, likely because of inertia playing additional roles that we did not take into account.

We also tune the frequency by acting on the parameters of the surrounding fluidic circuit. We increase the downstream fluidic resistance by decreasing the diameter of an orifice placed in line after the outlet of the actuator. As orifices, we use the Luer-to-barb connectors with different nominal ID diameters ($1.6\,\mathrm{mm}$, $2.4\,\mathrm{mm}$, $3.2\,\mathrm{mm}$, and $4\,\mathrm{mm}$). Note that we manually measure the internal diameter of the orifice with a

caliper, obtaining $1.2\,\mathrm{mm}$, $1.8\,\mathrm{mm}$, $2.3\,\mathrm{mm}$, and $3\,\mathrm{mm}$. For higher downstream resistance, the frequency of oscillation decreases, both in the resonant (Fig. S11B) and non-resonant (Fig. S11C) cases.

We study the influence of structural asymmetry on the oscillation frequency by adding a design parameter h, the height of the inlet over the outlet. Note that, for each h value, we adjust the length l of the tube by subtracting h from a reference length l_0. With this design choice, h represents the portion of the tube that is being clamped at the inlet side. We observe a non-monotonic trend of the oscillation frequency over h, for samples with $l = 36\,\mathrm{mm}$, $D_i = 2.5\,\mathrm{mm}$, $t = 0.4\,\mathrm{mm}$, and $d = 10\,\mathrm{mm}$ (Fig. S11D). This non-monotonic frequency trend is accompanied by a monotonic decrease in the x-stroke of actuation (Fig. S11E). We can calculate an estimated value of the locomotion speed for a hypothetical one-limb robot by multiplying the x-stroke by the activation frequency, observing an optimal value for h between $4\,\mathrm{mm}$ and $6\,\mathrm{mm}$ (Fig. S11F).

Given these various design parameters, we can achieve higher frequencies using a combination of them. For example, the tethered robot reaches $300\,\mathrm{Hz}$ (Figure 3K-N in the main text) because we chose low downstream fluidic resistance, the optimal asymmetry value, and small tubes with diameter scaled by a factor ~ 0.8 and length scaled by a factor ~ 0.5 relative to the reference design (Section S4).

Kinks behavior in time

To ease the understanding of the behavior of the kinks forming, traveling, and disappearing along the tube reported in Figure 2 in the Main section of the article, we report additional data in Figure S12. For clarity, refer to the definitions reported in Section M3.

For each pixel belonging to the outer edge cluster (for example, the 180-th pixel in the cluster is the green dot), we find the closest pixel belonging to the inner edge (magenta dot) (Fig. S12A). The pixel with the coordinates average of these two points (black dot) is assigned to the center line cluster. We resolve the outer and inner edges along the center line (Fig. S12B), and we plot the local width along the tube every $5\,\mathrm{ms}$ (Fig. S12C). The local minima of the local width are the two kinks. If only one local minimum is detected, then only one kink is present. The history of the individual kink (pink highlight) shows that the kink location

doesn't change when the kink is not dominant (grey arrow), while it increases once the kink becomes dominant (black arrow) (Fig. S12D). Moreover, the kink sharpens (the width decreases) while being non-dominant and non-moving (grey arrow), until it becomes dominant (blue star) (Fig. S12E).

In the resonating oscillation regime ($16\,\mathrm{SLPM}$), the kink covers a larger distance in the x-y plane. The kink distance overshoots the non-resonating case of approximately 50% (Fig. S12F). Note that the 'kink distance' fundamentally differs from the 'kink location'. The kink distance is defined on the x-y reference frame and, therefore, carries information regarding the structural displacement of the tube in the actuating plane. On the other hand, the kink location is defined on the reference frame along the tube itself (center line) (Section M3 for details on these definitions).

Flow-controlled and pressure-controlled response

We take a silicone tube actuator with $l = 36\,\mathrm{mm}$, $D_i = 2.5\,\mathrm{mm}$, $t = 0.4\,\mathrm{mm}$, and $d = 10\,\mathrm{mm}$. We decrease the input airflow from $20\,\mathrm{SLPM}$ to $0\,\mathrm{SLPM}$ in $2\,\mathrm{min}$ (Fig. S13A), observing two different oscillating pressure regimes (Fig. S13B) corresponding to the two frequency regimes (Fig. S13C) analyzed in Figure 2I-M in the main text. At $\sim 103\,\mathrm{s}$ ($\sim 3.8\,\mathrm{SLPM}$) the system stops oscillating because the flow is not high enough to build up pressure, and the tube stays in the two-kinks state. When pressure is low enough (at $\sim 112.5\,\mathrm{s}$), the non-dominant kink becomes dominant and the other kink disappears. The fluidic resistance increases, so the upstream pressure increases too, but without resulting in oscillation, since the kink is static (Fig. S13D).

We investigate the direct influence of pressure over the kinks' states by quasi-statically controlling the upstream pressure using a proportional pressure regulator (details on the setup in Section M2). We first increase the upstream pressure to $130\,\mathrm{kPa}$ in one minute, and then we decrease it to atmospheric pressure in one minute (Fig. S14A).

The output flow through the tube throughout the experiment (Fig. S14B) is directly related to the structural state of the system (Fig. S14C). Initially, the actuator is in a 'leaky state', with air flowing through. The actuator is then 'closed' because a sharp kink forms, blocking the airflow. For increasing pressure, the kink

travels along the tube. When the kink reaches the left side of the tube, the kink angle increases, causing the kink to leak and, therefore, the actuator to 'open'. When pressure decreases, the actuator follows a different pathway, staying open and forming a new, non-dominant kink. When pressure is low enough (around $20\,\mathrm{kPa}$), the new kink fully forms, and the actuator goes back to the leaky state. The pressure-flow profile emphasizes this fluidic hysteresis that arises under pressure-controlled conditions (Fig. S14D-H).

In summary, by experimentally simulating the pressure build-up and release, we confirm that the kinks' state is a direct consequence of the pressure state, with a hysteretic dependence. Throughout our work, under flow-controlled conditions, the kinks' state is, in turn, affecting the pressure state, causing pressure build-up when the actuator is 'closed', and release when the actuator is 'open', inducing the self-oscillatory behavior.

Fluidic coupling

We fluidically couple two self-oscillating actuators by connecting them in parallel to the same flow source using two identical tubes (Fig. 3A-G). The actuators have $l = 18\,\mathrm{mm}$, $D_i = 2\,\mathrm{mm}$, $t = 0.3\,\mathrm{mm}$, $d = 7.8\,\mathrm{mm}$, and $h = 3.9\,\mathrm{mm}$. The coupling tubes used for the experiments all have the same inner diameter of $2\,\mathrm{mm}$. The minimum length of each coupling tube is $\sim 7\,\mathrm{cm}$, which includes the Luer™ T connector and the additional length of the actuator at the inlet side. For each experiment, the input flow rate is set to $15\ \mathrm{SLPM}$.

When we couple the two self-oscillating actuators using tubes of length $12\,\mathrm{cm}$, we observe a distribution of the oscillation frequencies with two maxima at the two characteristic frequencies for in-phase and anti-phase activation (Fig. S15A). The system alternates between the in-phase and the anti-phase eigenmodes, as highlighted by the distribution of the phase shift (Fig. S15B). The pressure signals in time show how the two actuators are smoothly transitioning in and out of the two eigenmodes (Fig. S15C).

For coupling tubes' length between $24\,\mathrm{cm}$ and $47\,\mathrm{cm}$, we observe the frequencies of the two actuators becoming different, as a consequence of weaker coupling. With tubes longer than $52\,\mathrm{cm}$, coupling effects disappear, as we see the frequencies approaching the natural frequencies of the individual actuators, measured separately by providing half the inflow ($7.5\ \mathrm{SLPM}$) to each actuator alone (Fig. S15D).

Comparison of frequency and stroke in silicone tube and TPU pouch actuators

The inflow required to activate the oscillation for the TPU pouch actuator is $\sim 0.1\ \mathrm{SLPM}$, which is lower than the inflow provided by the two $3\,\mathrm{V}$ mini air pumps used to power the untethered robot ($\sim 0.54\ \mathrm{SLPM}$ and $\sim 0.64\ \mathrm{SLPM}$ when connected to the LiPo battery) (Fig. S16A). Note that, in comparison, the activating inflow of the silicone tube actuator is $\sim 3.8\ \mathrm{SLPM}$ (Fig. S13), which the mini air pumps cannot provide.

The maximum measured frequency of the TPU pouch actuator (with length $80\,\mathrm{mm}$, width $10\,\mathrm{mm}$, and holder angle $55°$) is $\sim 3.5\,\mathrm{Hz}$ (Fig. S16A). The reason for this lower oscillation frequency compared to the silicone tube design is likely the absence of a resonant mode and the higher geometric volume of fluid required for the kink to travel. We approximate the geometric volume V_{kink} associated with the traveling kink as the volume of a cylinder with area equal to the circular cross-section of the tube (with inner diameter D_{i}) and the height equal to the length of the tube covered by the traveling kink L_{kink}:

$$V_{\text{kink}} = \left(\frac{D_{\text{i}}}{2}\right)^2 \cdot \pi \cdot L_{\text{kink}}. \tag{23}$$

In the case of the silicone tube, we have $D_{\text{i}} = 2.5\,\mathrm{mm}$ by design and $L_{\text{kink}} \approx 8\,\mathrm{mm}$, since the kink moves from $\sim 20\,\mathrm{mm}$ to $\sim 28\,\mathrm{mm}$ along the tube (Fig. S12D). In the case of the TPU pouch, we know that at rest, the perimeter of the cross-section is two times the pouch width, which is $W = 10\,\mathrm{mm}$ by design. Therefore, approximating the shape of the pressurized pouch's cross-section as a circle, the diameter of the pressurized cross-section is $D_{\text{i}} = 2 \cdot W/\pi \approx 6.366\,\mathrm{mm}$. From Fig. 4A and Fig. S16B, we notice that the kink travels approximately from the beginning to the end of the tube, therefore $L_{\text{kink}} \approx 80\,\mathrm{mm}$. Therefore, we obtain the geometric volume associated with the kink traveling in the silicone tube as:

$$V_{\text{kink}}^{\text{tube}} \approx \left(\frac{2.5}{2}\right)^2 \cdot \pi \cdot 8 \approx 39\,\mathrm{mm}^3 \approx 0.039\,\mathrm{mL}, \tag{24}$$

and in the TPU pouch as:

$$V_{\text{kink}}^{\text{pouch}} \approx \left(\frac{6.366}{2}\right)^2 \cdot \pi \cdot 80 \approx 2546\,\mathrm{mm}^3 \approx 2.546\,\mathrm{mL}. \tag{25}$$

The stroke of the TPU pouch actuator is $\sim 57.1\,\mathrm{mm}$, higher than the stroke of the silicone tube actuator, which is $\sim 13.4\,\mathrm{mm}$ (Fig. S16B). Note the stroke of the actuator is obtained as the difference between the maximum and minimum x-coordinates of the actuator tip trajectory on the 26° rotated x-y reference frame. The tip trajectory is obtained from the tip coordinates of four subsequent cycles (Section M3 for details), re-ordered as nearest neighbors. We also report the silicone tube actuator's tip trajectory in the same scale as the TPU pouch actuator to highlight the higher actuation hysteresis of the TPU pouch actuator (Fig. S16C).

Power consumption of the TPU pouch actuator

We are interested in the fluidic power needed for the TPU pouch actuators to locomote (as the product between flow through the actuators and upstream pressure), in addition to the electric power consumed by the pumps, which is $\sim 1.5\,\mathrm{W}$ (Section S4). This analysis removes the contribution of the efficiency of the pumps, indicating the effective power consumed by the limbs to operate.

To compute the flow through the limbs while the robot locomotes, we use the measured pressure signals reported in Figure 4H-J in the main text. We do so by using the pump curve, which relates the downstream pressure to the flow the pump delivers. In principle, higher downstream pressure implies a lower flow delivered by the pump. With no downstream pressure, the pump delivers the maximum flow. We measured the pump curve by placing the pump in line with a pressure sensor, a variable resistance, and a flow sensor. We manually increased the resistance, while measuring pressure and flow. In Figure S17A,B, we report the measured curves of the pumps connected to the left and right limbs, respectively. We used MATLAB to fit the data with a function $Q = Q(p)$ that is the sum of two exponential terms:

$$Q = a \cdot e^{b \cdot p} + c \cdot e^{d \cdot p}, \tag{26}$$

obtaining a, b, c, d that minimize the error between the data and the curve (Fig. S17A,B).

Next, we compute the flow through the limbs by applying the function (26) to the pressure signals of the limbs (Fig. S17C), obtaining the flow signals reported in Figure S17D. We convert the flow from SLPM to liters per minute by using Equation (2) (with T_{gas} being the temperature in the lab $295.65\,\mathrm{K}$, and p_{gas} being

atmospheric pressure plus the pressure in Figure S17C). We obtain the flow in cubic meters per second by dividing by $6 \cdot 10^4$.

We compute the fluidic power provided to each limb by multiplying the pressure in pascals and the flow in cubic meters per second, obtaining the curves shown in Figure S17E. The average fluidic power provided to each limb is $\sim 0.06\,\mathrm{W}$. We obtain the total fluidic power provided to the locomoting robot (Fig. S17F) as the sum of the power provided to each limb. From this signal, we obtain the average fluidic power provided to the robot $\sim 0.11\,\mathrm{W}$.

For an analysis of the locomotion efficiency compared to other animals or robots, we refer to the cost of transport analysis in Section S4.

Characterization of the design parameters of the TPU pouch actuator

In this section, we will provide quantitative design guidelines to select soft tubes that display the self-oscillating behavior, based on the learnings from the mass-spring model (Section S1). We then characterize the self-oscillating behavior in response to changes in the design parameters of the tubes.

Our mass-spring model (Section S1) highlights three key characteristics that the tube must satisfy in order to achieve self-oscillation, namely:

(A) a non-monotonic torque-angle curve, with a negative stiffness regime. This characteristic is a requirement for the formation of a single kink;

(B) an increase in torque needed for kink formation (which typically also relates to stiffening upon pressurization);

(C) a significant increase in flow resistance at the location of the kink (Fig. S20 and Fig. S21).

Material-wise, since the options of commercially available tubes are limited, throughout the paper, we tested off-the-shelf elastomeric tubes with shore hardness 60 A, and we manufactured TPU tubes with shore

hardness 85 A. A complete experimental study on the effect of Young's modulus is therefore difficult to perform. Our coarse-grained model is also not suitable to validate the effect of stiffness. Yet, we can hypothesize the effect of the stiffness, and we believe that increasing the stiffness of the tubes will overall decrease the frequency of oscillation. Note that the kinking of tubes is formed when specific strains are reached, which correlates to the amount of volume in the tube (and thus to the flow). As the input flow is constant in our implementation, we expect the tube to go through the same deformation sequence, independently of stiffness. Yet, higher Young's modulus requires higher pressures, which, in the case of air, requires more air input and will also lead to more leakage through the kink. These two effects will delay the formation of kinks and thus delay the frequency. Still, it should be noted that stiffer tubes are expected to increase the resonance frequency, such that there might be specific inflows where the stiffness could have a positive effect on stiffness.

Various other parameters are more straightforward to change (and therefore more useful in practice). Since the options of commercially available thin tubes are fairly limited, we addressed the characterization of the self-oscillating tube by manufacturing custom-made TPU tubes of various lengths, inner diameters, and thicknesses (details of the manufacturing steps in Section M1). We measured the average oscillation frequency and stroke, given various input flows (Fig. S18). As a whole, the results serve as a guideline for a designer who would have specific requirements in terms of stroke and frequency, so that they could select the appropriate parameters to achieve it.

The TPU pouch tube is characterized by three design parameters: the thickness of the TPU sheet, the length of the sealing lines, and the width W between the sealing lines (Fig. S18A). These design parameters result in a tube with the same length, same thickness, and an inner diameter equal to $2 \cdot W/\pi$, because the circumference is twice the width between the sealing lines (Fig. S18B).

We start by comparing tubes with thickness $0.15\,\mathrm{mm}$ and $0.28\,\mathrm{mm}$, and same length $80\,\mathrm{mm}$ and inner diameter $6.37\,\mathrm{mm}$. We observe a considerably lower frequency for the thicker tube (Fig. S18C). In this case, the stroke is unaffected by the increase in thickness (Fig. S18D). The flow-frequency trend is qualitatively similar in the two thickness cases and scaled by a factor ~ 6.9, approximately equal to the cube of the

thickness ratio $(0.28\,\mathrm{mm}/0.15\,\mathrm{mm})^3 \approx 6.5$ (Fig. S18E).

We vary the length of the tube for a fixed inner diameter of $6.37\,\mathrm{mm}$ (width $10\,\mathrm{mm}$) and thickness $0.15\,\mathrm{mm}$. We observe that the frequency drops for increasing tube length, as more geometric volume of air is required for the kink to travel (Fig. S18F). The stroke increases with increasing tube length (Fig. S18G,J,K).

Finally, we vary the inner diameter of the tube by sealing tubes with widths from $7.5\,\mathrm{mm}$ to $15\,\mathrm{mm}$, keeping the length fixed to $80\,\mathrm{mm}$ and thickness $0.15\,\mathrm{mm}$. The frequency decreases for increasing inner diameter (Fig. S18H). In contrast to increasing the length, increasing the inner diameter results in nearly no change in the stroke (Fig. S18I,L,M).

In conclusion, with the overall information in Figure S18, a designer can determine tube parameters and inflow values that satisfy specific requirements in stroke and frequency. For example, given a requirement in stroke, we can determine the tube length that satisfies it (Fig. S18D). Then, for example, if we have a constraint in input flow that the pumps can provide, we check what frequency is reached by the tube of that length and width $10\,\mathrm{mm}$ (Fig. S18C). Given this result, if we require a higher (or lower) frequency, we design a tube with a lower (or higher) width (Fig. S18E) because the stroke will be unaffected (Fig. S18F).

Constrained actuation

The actuator undergoes the full-step actuation cycles even when constrained between two rigid walls. To study the behavior of the actuator when a rigid wall limits the workspace, we build the setup in Figure S19A. We mount the holder of the actuator on the bottom clamp of a tensile testing machine (details about the machine in Section M2) at a defined angle with the horizontal. We fix a 3D-printed flat PLA plate on the top clamp in series with the load cell. The plate displacement d is defined as a downward displacement of the top clamp. At zero displacement, the plate is not touching the oscillating actuator. Constant flow is provided with a proportional flow regulator, and the pressure in the actuator is measured with a pressure sensor (Section M2) placed before the inlet of the actuator. An x-y stage is placed on the bottom clamp to align the actuator with the top plate.

When fixing the holder angle to 0° and the actuator in contact with the wall, we observe a tooth-shaped profile of the measured force in time; when the wall is closer to the actuator (for higher wall displacement d), amplitude of force increases and frequency decreases (Fig. S19B).

When scanning the entire domain of the wall displacement d, we observe an increase in peak force for increasing values of d, for five different values of the holder angle (Fig. S19C), with a maximum measured force of $\sim 2.4\,\mathrm{N}$. Likewise, the peak pressure inside the actuator increases with d (Fig. S19D), reaching $\sim 150\,\mathrm{kPa}$. This increase in peak force and peak pressure is accompanied by a decrease in oscillation frequency (Fig. S19E). We do not observe oscillation (zero frequency) for holder angle -15°, 0°, and 15° at $d/d_{\text{max}} = 1$.

Placing the wall closer to the actuator not only increases the peak force and pressure but also influences the behavior of the kinks traveling along the tube. For the example case with 45° holder angle, increasing the wall displacement results in the tube undergoing different shapes throughout an oscillation period, and in the outlet holder rotating less (Fig. S19F-H). Importantly, for this specific case with 45° holder angle, the full-step actuation pattern is still present when the wall is in contact with the outlet holder (Fig. S19H).

S3 Kink formation in thin tubes undergoing bending

To investigate the behavior of the kink formation in thin tubes undergoing bending and pressurization and to understand the underlying differences between the specific tubes used throughout our study (silicone tubes and TPU pouches), we build a setup that involves two main parts (Fig. S20A).

In the first part, to control the bending angle in a quasi-static fashion, we mount a 3D-printed rack on the top clamp of a tensile testing machine (details about the machine in Section M2), and a 3D-printed pinion on a bearing connected to the bottom clamp. In this way, controlling the displacement of the rack results in controlling the angle of the pinion. We place the sample on the setup, fixing the inlet side to the bottom stage, and the outlet side to the pinion, so that an imposed angle of the pinion results in an imposed angle between the inlet and the outlet. An x-y stage mounted at the bottom guarantees alignment between the rack and the pinion. The setup is similar to the one used for the soft kink valves (*33*), although here we explicitly control

the bending angle of the tube, instead of the linear distance between the inlet and the outlet.

In the second part, to control the upstream pressure in a quasi-static fashion, we connect the inlet of the sample to a proportional pressure regulator. The regulator is connected to a pressure supply of $1.5\,\mathrm{bar}$. Note that, to guarantee that the desired upstream pressure is applied, we place a needle at the outlet of the tube (METCAL 918050-TE, 18GA 1/2"). The needle acts as a fluidic resistance, to impose the pressure drop needed for the regulator to set the upstream pressure. Between the pressure regulator and the inlet of the sample, we place a flow sensor to measure the airflow Q through the sample. Two pressure sensors are placed before and after the sample, to probe the upstream pressure p_1 and the downstream pressure p_2 (details on the sensors and regulators in Section M2).

We select a silicone tube sample with length $36\,\mathrm{mm}$, inner diameter $2.5\,\mathrm{mm}$, and thickness $0.4\,\mathrm{mm}$, and a TPU pouch sample with length $36\,\mathrm{mm}$ and width $10\,\mathrm{mm}$. This specific choice reflects the two kinds of tubes used throughout our study. We set the upstream pressure to $20\,\mathrm{kPa}$, and we control the bending angle by linearly increasing the rack displacement from $0\,\mathrm{mm}$ to $88\,\mathrm{mm}$ for the silicone tube, and to $80\,\mathrm{mm}$ for the TPU pouch, in 1 minute. From the signals of p_1, p_2 and Q we extract the fluidic resistance as $(p_1 - p_2)/Q$.

In the case of the silicone tube (Fig. S20B), we observe low resistance ($\sim 0.1\,\mathrm{kPa/SLPM}$) for low bending angle values, until $\sim 80°$, because no kink is present in the tube (Fig. S20D). At around $100°$, the system snaps to a higher resistance state ($\sim 20\,\mathrm{kPa/SLPM}$), because the kink suddenly forms (Fig. S20E). The kink is not fully closed, resulting in leakage through the kink; the resistance now increases exponentially with the bending angle ('leaky kink' regime in Figure S20B). Only for bending angles higher than $\sim 130°$, the kink is fully closed (Fig. S20F), with the output flow dropping to zero (plus sensor noise) ('kink' regime in Figure S20B).

For the case of the TPU pouch (Fig. S20C), we also observe an initial no-kink state (Fig. S20G). For increasing bending angle, the system shows a sudden snapping event at $\sim 100°$, with the kink fully forming (Fig. S20H). We don't observe an intermediate leaky-kink regime in this specific test on the TPU pouch.

We derive the phase spaces of both the silicone tube and the TPU pouch as the fluidic resistance function of upstream pressure and bending angle. We perform ten tests with the silicone tube, where we impose

the upstream pressure (from $10\,\mathrm{kPa}$ to $100\,\mathrm{kPa}$ in increments of $10\,\mathrm{kPa}$) and we sweep the bending angle (Fig. S21A). We reverse the loading order by first imposing a bending angle and then sweeping the upstream pressure (Fig. S21B). These two experiments allow us to illustrate the phase space of the tube for both cases of loading order (Fig. S21C,D). We perform equivalent experiments for the TPU pouch but with a lower pressure limit since we observe the curves approaching asymptotes (Fig. S21E,F).

When we compare the phase spaces of the silicone tube (Fig. S21C,D) and of the TPU pouch (Fig. S21G,H), we notice some similarities. In both cases, increasing the upstream pressure leads to a reduction of the kink phase (Fig. S21C,G). This is due to the known effect of inhibition of the kink due to pressurization of the tube (*33*). Moreover, increasing the imposed bending angle leads to kink formation in both cases (Fig. S21D,H).

Comparing the phase spaces, we also notice important differences. We observe a first difference at high upstream pressure values: the kink phase of the silicone tube disappears (Fig. S21C), while it is still present in the case of the TPU pouch (Fig. S21G). This difference also holds for low values of the imposed bending angle: the kink phase is not present in the case of the silicone tube (Fig. S21D), while it appears (for low pressures) in the case of the TPU pouch (Fig. S21H). Moreover, we see that in general, the silicone tube has a larger leaky kink phase compared to the TPU pouch. This is particularly evident at low pressure values, where it is practically absent for the TPU pouch, and it scans half of the angle domain for the silicone tube (Fig. S21C,G). In addition, for low pressure values, the kink of the TPU pouch appears at much lower values of bending angle than in the case of silicone tube (Fig. S21C,G). Finally, when the TPU pouch is first bent at high angle values and then pressurized, it cannot exit the kink phase when pressurized (Fig. S21H), while the silicone tube transitions to a leaky state (Fig. S21D). Taken together, these observations lead us to the conclusion that the TPU pouch favors kink formation, and inhibits kink leakage, compared to the silicone tube, especially at low pressures.

S4 Robots analysis

In this Section, we report additional results and calculations concerning our tethered and untethered robots. We report the analysis of i) the tethered robot stotting, ii) the untethered robot hopping, iii) the cost of transport of the untethered robot, iv) the untethered robot on irregular terrain, v) the tolerance of the implicit synchronization to imbalance between the inputs, and vi) the robots' speed performance compared with the state-of-the-art.

Tethered robot stotting

The tethered robot is connected to the pneumatic power source through a thin tube with inner diameter $2\,\mathrm{mm}$, thickness $0.3\,\mathrm{mm}$, and length $70\,\mathrm{cm}$. When we apply a pressure $p_{\text{in}} = 1.7\,\mathrm{bar} = 1.7 \times 10^5\,\mathrm{Pa}$ at the tether alone, we measure a flow $Q_{\text{in}} \approx 28\,\mathrm{SLPM}$ (Fig. S22A).We derive the flow in cubic meter per second by using Equation (3), obtaining $Q_{\text{in}} \approx 4.98 \times 10^{-4}\,\mathrm{m^3/s}$.

We calculate the power provided to the robot via the tether:

$$P_{\text{in}} = p_{\text{in}} \cdot Q_{\text{in}}, \tag{27}$$

with $p_{in} = 1.7 \times 10^5\,\mathrm{Pa}$ and $Q_{\text{in}} \approx 4.98 \times 10^{-4}\,\mathrm{m^3/s}$, obtaining $P_{\text{in}} \approx 85\,\mathrm{W}$. Each limb is therefore powered by $\sim 21\,\mathrm{W}$.

We perform six tests where we turn on the pressure at the tether, and we track the robot's location in time, observing repeatable behavior (Fig. S22B). We select the last 11 datapoints of the tracked location in time for each test, obtaining the steady-state speed for each test as the slope of the linear fit (Fig. S22C). The average steady-state speed is $1.08 \pm 0.09\,\mathrm{m/s}$ ($30 \pm 2.5\,\mathrm{BL/s}$).

We calculated the Froude number FR of our robot according to:

$$\text{FR} = \frac{v^2}{g \cdot h}, \tag{28}$$

with v the robot's speed, $g = 9.81\,\mathrm{m/s^2}$ gravity acceleration and h the hip joint height (*48, 49*). The Froude number is useful when comparing locomoting gaits of robots or animals that widely differ in size, as it nor-

malizes the speed in relation to the body size (hip joint height), similarly to the relative speed in body lengths per second. In our case, the hip joint height is the distance between the rigid limb-connector and the ground, therefore, the height of the active soft limbs. This distance does vary in time as the limbs self-oscillate, so we consider the approximate average value throughout one oscillation cycle. In the case of the tethered robot, we have $v = 1.1\,\mathrm{m/s}$ and $h \approx 6\,\mathrm{mm} = 6 \times 10^{-3}\,\mathrm{m}$, obtaining FR ≈ 20.6.

We can predict the steady-state speed of the robot from the experimental results concerning an individual limb. Note that the following calculation is approximate, given the manufacturing differences between tubes and the approximate scaling factors. An individual limb with inner diameter $2.5\,\mathrm{mm}$ and asymmetry height $6\,\mathrm{mm}$, when resonating, oscillates at $\sim 155\,\mathrm{Hz}$ with a stroke of $\sim 10\,\mathrm{mm}$, resulting in an estimated single-limbed robot's speed of $\sim 1.5\,\mathrm{m/s}$ (Fig. S11D-F). Note that the robot is equipped with actuators with inner diameter $2\,\mathrm{mm}$, which are smaller than the $2.5\,\mathrm{mm}$ by a factor 0.8. We also designed the other parameters of the actuators on the robot (reference length and inlet-outlet distance) as scaled by a factor 0.8. Therefore we assume that the stroke in Figure S11E also scales by a factor 0.8. Importantly, in the final design we use shorter tubes on the robot, with length $18\,\mathrm{mm}$ (instead of the directly scaled length of $\sim 28\,\mathrm{mm}$), therefore we further scale the stroke by a factor 0.65. Moreover, the volume of air required for the kink to travel scales linearly with the length of the tube, as it approximates a cylinder with height being the distance covered by the kink along the tube. So, we estimate that the time required for the kink to travel also scales linearly with the length. Therefore, we scale the expected frequency by $1/0.65 = 1.54$, as we scaled the length of the tube by 0.65. Because we scaled the whole tube down by a factor 0.8, we scale the frequency by another factor 1.4 that we measured experimentally (Fig. S11A). This leads to an estimated speed (as stroke times frequency) of $\sim 1.67\,\mathrm{m/s}$, close to the measured speed of the real robot ($1.08\,\mathrm{m/s} \pm 0.09\,\mathrm{m/s}$). The difference might be due to losses in friction and overestimation of the effective stroke of the actuator when interacting with the ground.

Untethered robot hopping and swimming

One example dataset of the tracked position in time of the untethered robot shows that a linear fit captures the locomotion behavior (Fig. S22D). Among eleven runs, the robot locomotes in a repeatable fashion: to ease the visual understanding, in Figure S22E, we offset each dataset along the time-axis so that they are separated by $0.5\,\mathrm{s}$. The robot hops with an average speed of $18.17 \pm 0.68\,\mathrm{cm/s}$ ($1.93 \pm 0.07\ \mathrm{BL/s}$). We calculate the Froude number FR of the untethered robot using Eq. (28), with hip joint height $h \approx 20\,\mathrm{mm} = 2 \times 10^{-2}\,\mathrm{m}$, obtaining FR ≈ 0.16.

The phototactic version of the robot has two modifications. First, the on/off switch is removed. Second, each pump is connected to a transistor, which in turn is connected to a photoresistor (Section M1 and Fig. S4C for details on the connections). We place the robot with an initial angle and distance with respect to the light (Fig. S22F). With this relatively simple update involving the two photoresistors, the robot achieves phototaxis with 87% success rate among 15 runs (Fig. S22G). The robot steers in place because only one photoresistor detects light, as can be seen in Figure S22H,I by the distance not changing and the angle decreasing. The robot hops forward when both photoresistors detect light. Note that the forward hopping presents a slight drift, with the angle increasing while the distance from the light decreases (Fig. S22H,I). This might be due to differences between the two LDRs and the two transistors that, if large enough, result in different pressures in the actuators and, therefore, different forces exerted on the ground. Despite being synchronized in terms of phase, this asymmetry in the force amplitude might be the reason for the robot's drift. However, this drift is negligible in the forward-hopping behavior. Importantly, whenever the cumulative drift causes the robot to point in the 'wrong' direction, the robot autonomously compensates by steering in place, achieving successful phototaxis despite the manufacturing imperfections (movie S7 for visual confirmation).

To quantify the phase shift between the two limbs in the swimming robot, we tether both limbs to two flow regulators set at $0.3\,\mathrm{SLPM}$, and we measure pressure at the tethers with pressure sensors (Section M2). In addition to extrapolating the change in phase shift of the pressure signals due to the transition from ground to water (Fig. 5B), we also compute the average phase shift in steady-state conditions, for 50 oscillations of

each limb, in both media. For the water case, we let the robot swim in the tank, and we consider pressure data of 50 oscillations of each limb when the robot is freely swimming, so we discard spurious data corresponding to the robot bumping against the walls of the tank. On the ground, we use pressure data of the robot hopping 50 times. We extrapolate the phase shift over these 50 limb oscillations, obtaining $0.6 \pm 4.2^\circ$ for the ground case and $181.5 \pm 7.7^\circ$ for the water case, confirming the stability of each gait in steady state.

Cost of transport of the untethered robot

We calculate the total cost of transport C_T of the untethered robot following:

$$C_\mathrm{T} = \frac{E_\mathrm{in}}{w \cdot d}, \tag{29}$$

with E_in the electrical input energy from the LiPo battery, w the weight of the robot, and d the distance traveled given the input energy (*9*). We can rewrite equation (29) as function of input power P_in and robot's speed v:

$$C_\mathrm{T} = \frac{P_\mathrm{in}}{w \cdot v}. \tag{30}$$

The system operates with an electric power $P_\mathrm{in} = 1.5\,\mathrm{W}$. We calculate this value by visually measuring, with an ampere meter, the total current of $\sim 0.4\,\mathrm{A}$ drawn by the hopping robot when connected to a $3.7\,\mathrm{V}$ DC power supply. Considering $P_\mathrm{in} = 2 \cdot P_\mathrm{in}^\mathrm{limb} \approx 1.5\,\mathrm{W}$, robot's weight $w = 7.67 \times 10^{-2}\,\mathrm{kg} \cdot 9.81\,\mathrm{m/s^2}$, and speed $v = 1.817 \times 10^{-1}\,\mathrm{m/s}$, we obtain:

$$C_\mathrm{T} \approx 10.97. \tag{31}$$

Therefore, in terms of the total cost of transport, our robot is more efficient than a mouse and less efficient than a rat, according to the comprehensive list reported by Baines et al. (*40*).

We compare our tethered robot with the untethered robot in terms of speed and efficiency. The tethered robot moves fast with a high Froude number ~ 20.6, but inefficiently with high cost of transport ~ 1926. Our untethered robot, on the other hand, moves efficiently with a relatively low cost of transport ~ 11, but more slowly, with Froude number ~ 0.16.

Untethered robot locomoting on irregular terrain

To understand how the untethered robot negotiates irregular grounds, we started by placing a single bump in front of the untethered robot (Fig. S23). We ran multiple tests with bumps of width $200\,\mathrm{mm}$, depth $16\,\mathrm{mm}$ and different heights ranging from $3\,\mathrm{mm}$ to $21\,\mathrm{mm}$ in increments of $3\,\mathrm{mm}$.

We observed three distinct behaviors of the robot in response to the presence of the bump. The robot negotiates low bumps (up to around $9\,\mathrm{mm}$) by hopping over it, as the soft limbs deform when interacting with the bump (Fig. S23A). The robot fails to overcome the bump for bump heights around $12\,\mathrm{mm}$, as the front rigid limbs act as a pivot (Fig. S23B). Higher bumps act as an obstacle, and the robot avoids them as the limbs go out of synch, causing the robot to steer in place (Fig. S23C).

We ran five tests for each value of bump height for two cases of surface (flat metal and flat paper). For each test, we took note of the outcome of the negotiation. We observe that the success rate of negotiation drops as the bump height increases (Fig. S23D, purple). On a paper surface, the increase of friction between the limbs and the ground leads to higher success rates (Fig. S23E, purple). This is thanks to the front limbs elevating at larger heights, likely as a result of the higher forces exerted by the self-oscillating limbs due to the increased friction.

With this understanding of how the robot deals with a single bump, we checked how it manages locomotion on an irregular, granular terrain with granules size between $8\,\mathrm{mm}$ and $16\,\mathrm{mm}$ (Stonewish Yellow 8-16mm, GAMMA). As shown in Figure S23F, the robot displays the same failure mode as in the single bump scenario, pivoting around the front rigid limbs. Considering that this whole-body flipping is the only failure mode we observed, we decided to re-design the front limbs to address the issue. We 3D-printed longer limbs ($15\,\mathrm{mm}$ longer), and we placed them wider on the body of the robot ($105\,\mathrm{mm}$ wider) (Fig. S24A). The updated robot successfully locomotes on an uneven, granular terrain with granules size between $8\,\mathrm{mm}$ and $16\,\mathrm{mm}$, with the limbs synchronizing in-phase (Fig. S24B). This updated design reduces the rotational motion of the robot, stabilizing the in-phase synchronization of the self-oscillating limbs. As seen in Figure S24C, this change in the body morphology removes the obstacle avoidance behavior that we previously observed in Figure S23C.

Tolerance of the implicit synchronization to imbalance between the inputs

To understand the tolerance of the synchronized behavior to differences in left and right inputs to the limbs, we focus on the untethered robot as the platform for the case study. To precisely control the variable inputs to each limb, we removed the pumps and battery, and we tethered each limb to a flow regulator (details on the fluidic setup in Section M2). We applied a constant input flow of 0.4 SLPM to the left limb, and we varied the input flow to the right limb from 0.4 SLPM to 0.1 SLPM in intervals of 0.05 SLPM. For each of these cases, we measured the natural frequencies of the self-oscillating limbs when not interacting with the ground, and we then placed the robot in locomoting position on the ground.

In Figure S26A, we report the on-ground frequencies of the limbs as a function of the ratio of the two natural frequencies. We observe that up to natural frequencies ratio ~ 1.7, the two on-ground frequencies match, so their ratio is ~ 1 (Fig. S26B). Up to this value of the difference between the two inputs, the system is in a phase-lock state: the in-phase synchronization is stable (Fig. S26A,B, yellow highlight). For larger differences in inputs, the two limbs oscillate at different frequencies (Fig. S26A,B). We call this value the critical natural frequencies ratio (purple star in Figure S26B), as the synchronization tolerates a ratio of natural frequencies smaller than such value.

We repeated the same experiments while adding additional mass to the robot (Fig. S26C). We added weights of $\sim 35\,\mathrm{g}$ and $\sim 65\,\mathrm{g}$. We discovered that, due to the added inertia, the critical ratio of natural frequencies increases (Fig. S26D). In other words, the system with mass $\sim 98\,\mathrm{g}$ now synchronizes in-phase even if the natural frequency of the left limb is ~ 3.4 times the one of the right limb. This is because the two limbs are more strongly coupled, thanks to the increased downward force acting on them.

Robots' speed performance compared with the state-of-the-art

We frame the performance of our robots in the context of state-of-the-art soft robots. We gather data concerning the fastest tethered and untethered soft robots and classify them depending on their actuation and control mechanisms. We classify 'tethered' as any soft robot that is connected to the tether line, either for power or

control. We call 'untethered' any soft robot that instead carries both power and control systems on board. Note that here, when we mention 'control', we slightly diverge from the classical mechatronics definition. We consider 'control' any mechanism that sequences the activation of robotic actuators so that a desired functionality, such as a walking gait, emerges. For example, classical control involves microcontrollers sending sequenced input signals to activate pumps or motors, and fluidic circuits generate these sequenced signals through the interaction of fluid flow or pressure and nonlinear mechanical elements, that imitate analog or digital electronic circuits (*15*).

Next, we divide the fast tethered robots into two categories. i) Soft robots that internally embody the actuation sequencing (*17–20, 23–26*) (blue dots in Figure S27A,C and in Figure 3J). ii) Soft robots that rely on external control apparatus for actuation sequencing (typically microcontrollers and software, or signal generators), spanning a wide range of physics underlying their actuation (among others, piezos, dielectric elastomers, shape-memory alloys, etc.) (*37, 39, 50–62*) (grey dots in Figure S27A,C and in Figure 3J).

By definition, the untethered robots carry their control systems on board. Therefore, technically, they all have internal actuation sequencing based either on microcontrollers or fluidic circuits. For this reason, we decide to classify them depending on the actuation technology: fluidic (*18, 20, 25, 26, 34*) (blue dots in Figure S27B,D) compared to any other technology (grey dots in Figure S27B,D) (*39, 50, 51, 57, 61*). The data gathered for this modest performance review are reported in Tables S2 and S3, sorted for descending relative speed ($\mathrm{BL/s}$). Note that data strictly refer to robots that perform controlled, robust locomotion on a flat surface. We did not include robots locomoting on engineered surfaces or robots performing uncontrolled or unstable locomotion.

Our tethered robot is two orders of magnitude faster than state-of-the-art robots with internal actuation sequencing and runs at a speed comparable to other ultrafast soft robots that require external control signals to operate (Fig. S27A,C and Fig. 3J). Our untethered robot is one order of magnitude faster than state-of-the-art untethered fluidic robots and hops at a speed comparable to other untethered soft robots that implement any other soft technology (Fig. S27B,D).

Supplementary Figures

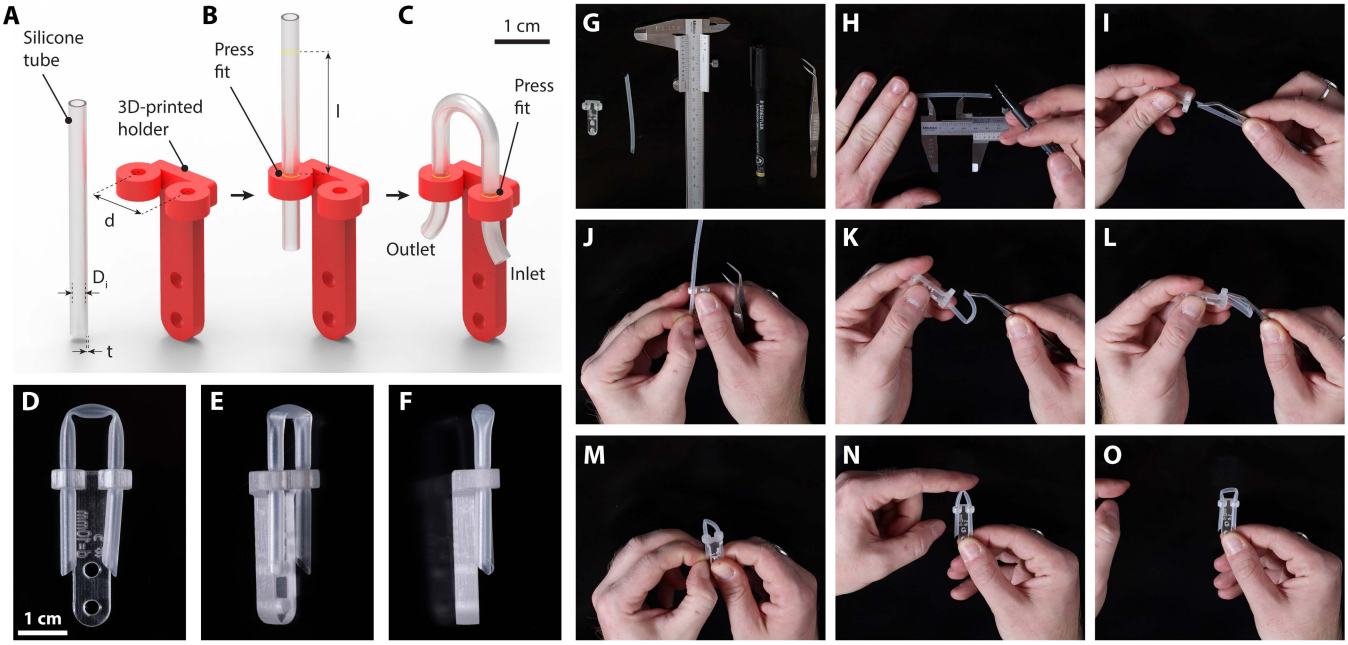

Figure S1: **Manufacturing of the silicone tube actuator.**
The manufacturing of the silicone tube actuator follows a straightforward three-step procedure. After (**A**) printing the holder and marking the desired tube length, we (**B**) insert the tube in one end, sliding it until the first mark. (**C**) We then insert the other end. (**D**, **E**, **F**) Photographs of a manufactured sample. After (**G**) preparing the required materials and tools (3D-printed holder, silicone tube, caliper, marker, tweezer), (**H**) we mark the tube at the desired length. (**I**) We insert the first side of the tube, and (**J**) we slide the tube until the mark. We (**K**) bend (without twisting) the tube, (**L**) inserting it in the other side of the holder. (**M**) We slide this side until the mark. We (**N**) poke the tube to check the existence of (**O**) the other two-kink stable state.

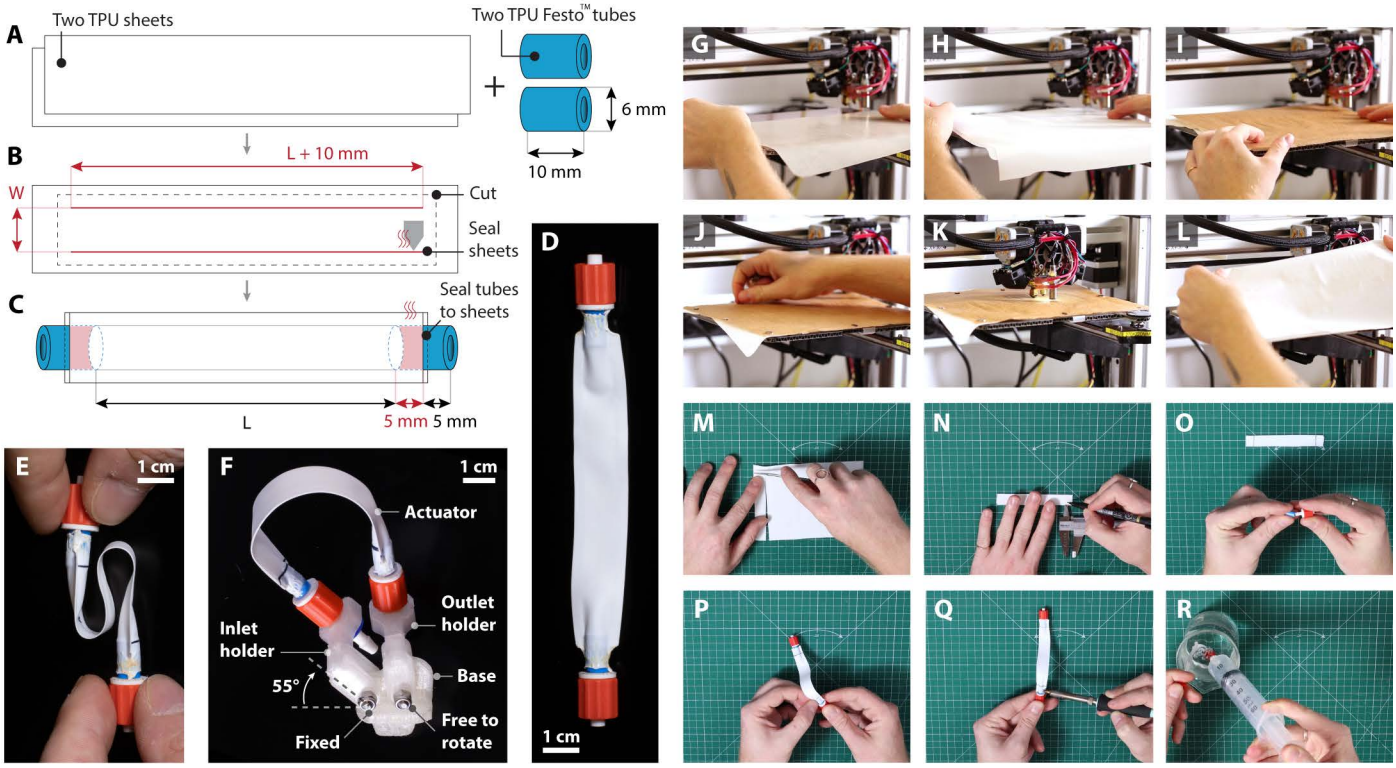

Figure S2: **Manufacturing of the TPU pouch actuator.**
The manufacturing of the TPU pouch actuator follows a three-step procedure. (**A**) We take two TPU sheets with thickness $0.15\,\mathrm{mm}$ and two TPU Festo™ with external diameter $6\,\mathrm{mm}$ and length $10\,\mathrm{mm}$. (**B**) We heat-seal the two sheets along two lines of length $L + 10\,\mathrm{mm}$, at a distance W from each other (with L the desired length of the actuator and W the desired width) and we cut the residual material. (**C**) We insert the Festo™ tubes in both ends of the pouch (both entering $5\,\mathrm{mm}$ inside the pouch) and we seal the pouch to the tubes with a soldering iron. Photographs of a manufactured sample, (**D**, **E**) without and (**F**) with holder. Snapshots of the heat-sealing procedure show that (**G**) we first place the silicone mat on the machine bed, then (**H**) the two TPU sheets with the glossy side sandwiched, followed by (**I**) oven paper. (**J**) We place magnets to keep the sheets in place. (**K**) After the G-code is sent, the machine heat-seals the sheets (note that we heat-seal multiple actuators at once to minimize waste material). (**L**) We inspect the sealed sheets. After (**M**) cutting the residual material around the sheets, (**N**) we mark the desired length of the actuator. (**O**) We insert the Luer™ connectors in the Festo™ tubes and (**P**) the Festo ™ tubes in the sealed sheets. (**Q**) Using a soldering iron, we heat-seal the sheets to the tubes on both sides. (**R**) We check for leakage by pressurizing the actuator with air using a syringe and placing it underwater. If we notice bubbles exiting the actuator, the seal leaks. In that case, we repeat steps **Q** and **R** until we don't see bubbles anymore.

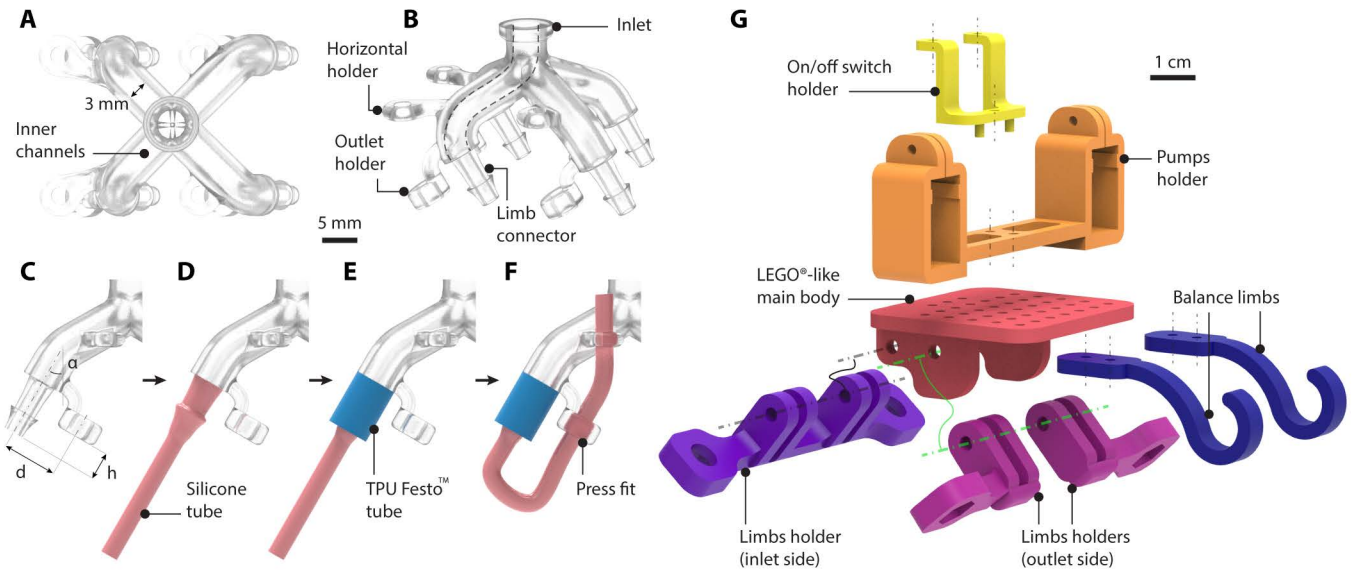

Figure S3: **Manufacturing of the robots.**
(**A**, **B**) Renders of the body of the tethered robot. (**C**, **D**, **E**, **F**) The limbs are mounted on the robot with a three-step process. (**G**) Exploded render of the untethered robot.

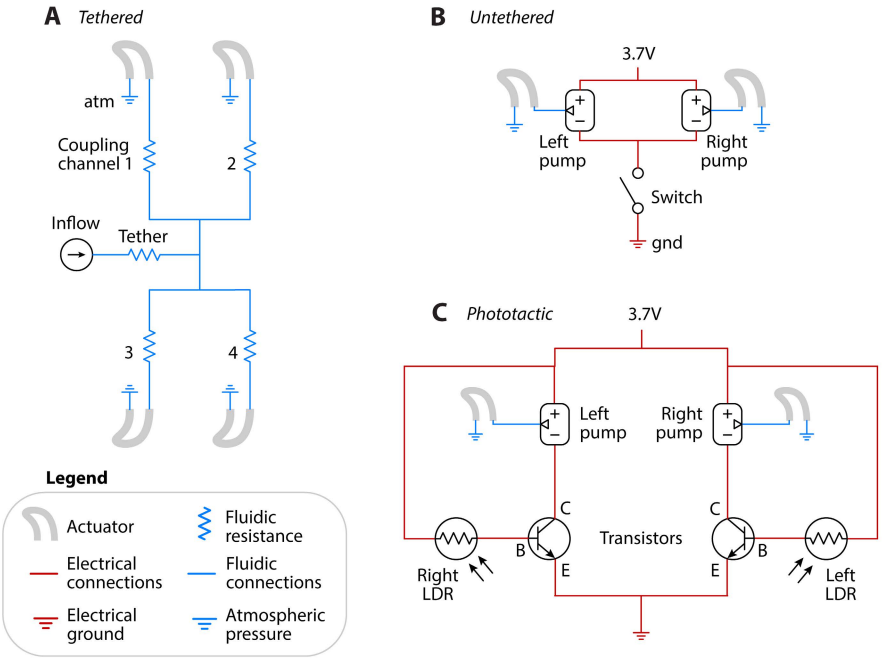

Figure S4: **Schematics of the robots.**
(**A**) Schematic of the fluidic connections of the tethered robot. Schematic of the fluidic and electrical connections of (**B**) the untethered robot and of (**C**) the phototactic untethered robot.

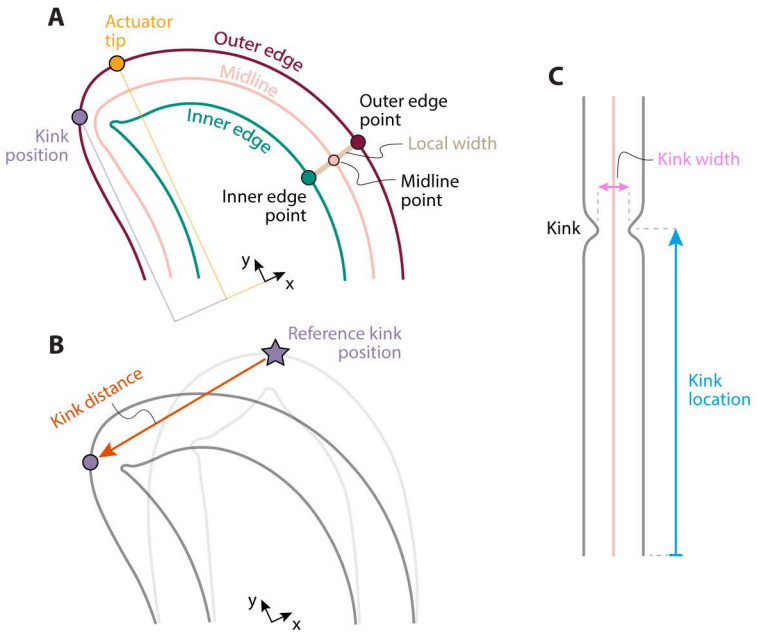

Figure S5: **Visual representation of the defined quantities.**
(**A**) Quantities that can be extrapolated from a single frame of the high-speed recordings. (**B**) Storing the kink position at an arbitrary reference instant allows us to define the kink distance. (**C**) Unfolding the tube along the center line allows us to extrapolate the kink location and the kink width.

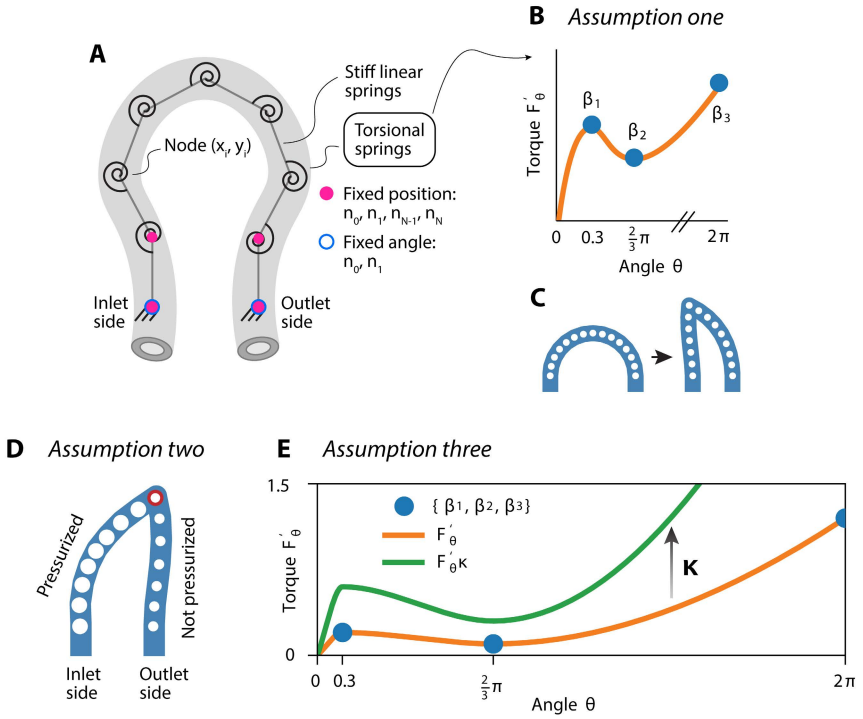

Figure S6: **Mass-spring model to simulate the self-oscillating behavior of a tube.** (**A**) Mechanical mass-spring model representation of the tube, with point masses at nodes connected by linear and torsional springs that simulate stretching and bending. (**B**) Assumption one: nonlinear torque-angle curve $\beta_{(\theta)}$ of the torsional springs. We also report the reference points used for interpolation (β_1, β_2, and β_3). **C**) As a consequence of assumption one, when inlet and outlet are moved closer together, a kink forms in the tube, because that specific torsional spring snaps to the other stable branch between β_2 and β_3. (**D**) Assumption two: the section of the tube before the dominant, sharpest kink (red dot), on the inlet side, is pressurized because the kink locally increases fluidic resistance under flow-controlled conditions (Fig. S20 and Fig. S21) (larger white dots correspond to higher pressure). (**E**) Assumption three: the torsional springs on the pressurized section of the tube are stiffer by a factor κ. In this specific case, we assigned $\kappa = 2$.

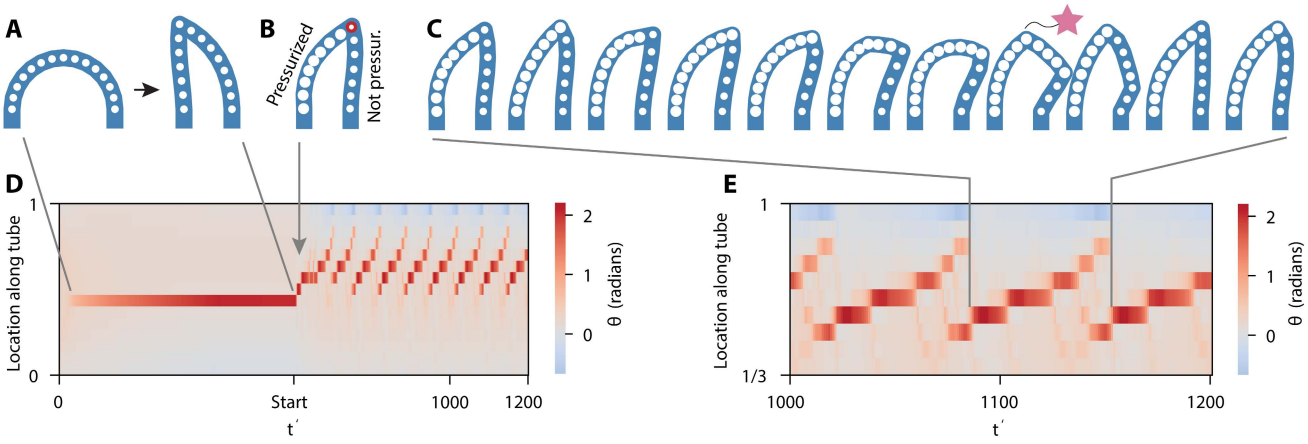

Figure S7: **Simulation of the mass-spring model of the tube.**
(**A**) We start the simulation by displacing the inlet side toward the outlet side, and, as a consequence of assumption one (Fig. S6), a kink forms at around the center. (**B**) We enforce assumptions two and three (Fig. S6). (**C**) As a consequence of the three assumptions, after the kink forms, the stiffening on the left side of the kink results in the kink traveling along the tube. When the kink reaches a critical location along the tube, a new kink forms in the stiffer section (pink star), because the springs in the stiffer part of the tube still present the non-linear behavior of assumption one. (**D**) Spatiotemporal signature of the system, i.e., the angles of the springs on all locations along the tube, in time. From non-dimensional time $t' = 600$ (start), the stiffening (assumption two and three) is enforced, and the kinks arise, travel, and disappear cyclically at a stable frequency. (**E**) Spatiotemporal signature for two full oscillation cycles, showing how the second instability causes two kinks to briefly appear simultaneously. A switch in the dominant kink is then observed, leading to the spontaneous reset of the system, such that the cycle repeats.

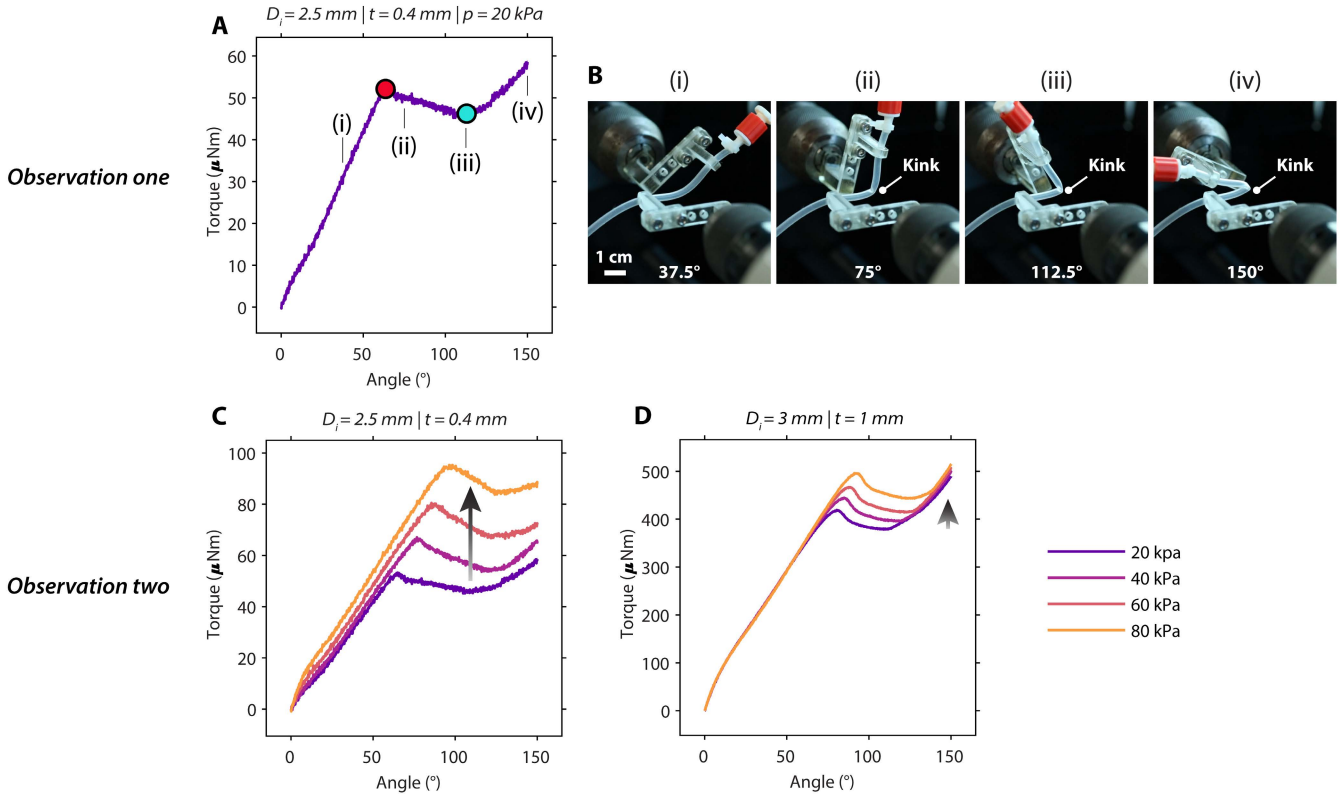

Figure S8: **Two experimental observations that inform the mass-spring model to simulate the self-oscillating tube.** Using a microtorsion testing machine (Instron MT1-E1), we increase the bending angle of a silicone tube of length 36 mm, and we measure the torque while regulating pressure inside the tube. (**A**) Observation one: we observe a non-monotonic torque-angle response, with a negative stiffness branch between a peak (red dot) and a valley (blue dot): the formation of the kink is a mechanical instability. (**B**) Snapshots of the tube at angle (i) 37.5°, (ii) 75°, (iii) 112.5°, (iv) 150°. (**C**) Observation two: when increasing the pressure inside the tube, higher torques are required to kink and unkink the tube. (**D**) A thicker silicone tube with inner diameter 3 mm and thickness 1 mm still displays the non-monotonic response, but the relative change in behavior upon pressurization is lower than in the case of the thinner tube in **C**.

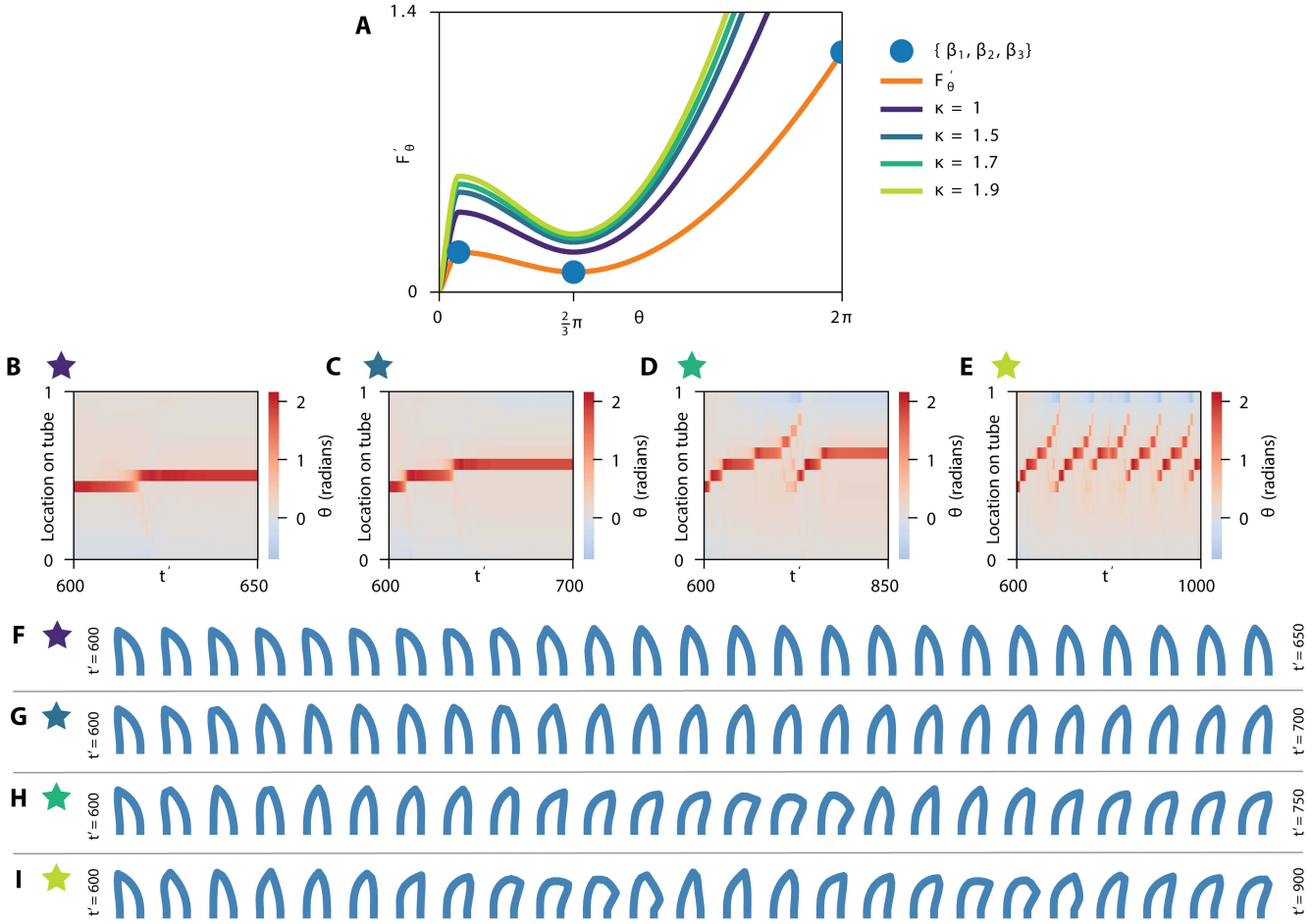

Figure S9: **In the simulation, increasing the pressure-induced stiffening enables the self-oscillation.** (**A**) Torque-angle curves of the springs in the soft region after the kink (orange line) and in the stiff region before the kink (blue to green lines), for different values of stiffness multiplier κ (1, 1.5, 1.7, and 1.9). (**B**) Bending angles of the nodes along the tube (location 0 being the inlet, and location 1 the outlet) over time for $\kappa = 1$. Insufficient stiffening prevents the kink from traveling further than the middle of the tube, and the oscillation is not sustained. (**C**) Angles over time for $\kappa = 1.5$. The kink is able to propagate further along the tube because of the increased stiffness but does not reach the point where a new instability forms in the stiff region, so oscillation is not sustained. (**D**) For $\kappa = 1.7$, the kink propagates far enough to reach a second instability and initiate a restart of the process once due to initial momentum, but it is not able to sustain the oscillation over multiple cycles. (**E**) Angles over time for $\kappa = 1.9$. This is the lowest value of κ that enables the tube to sustain subsequent oscillations. (**F**, **G**, **H**, **I**) State of the tube over time corresponding to the situations in **B**-**E**.

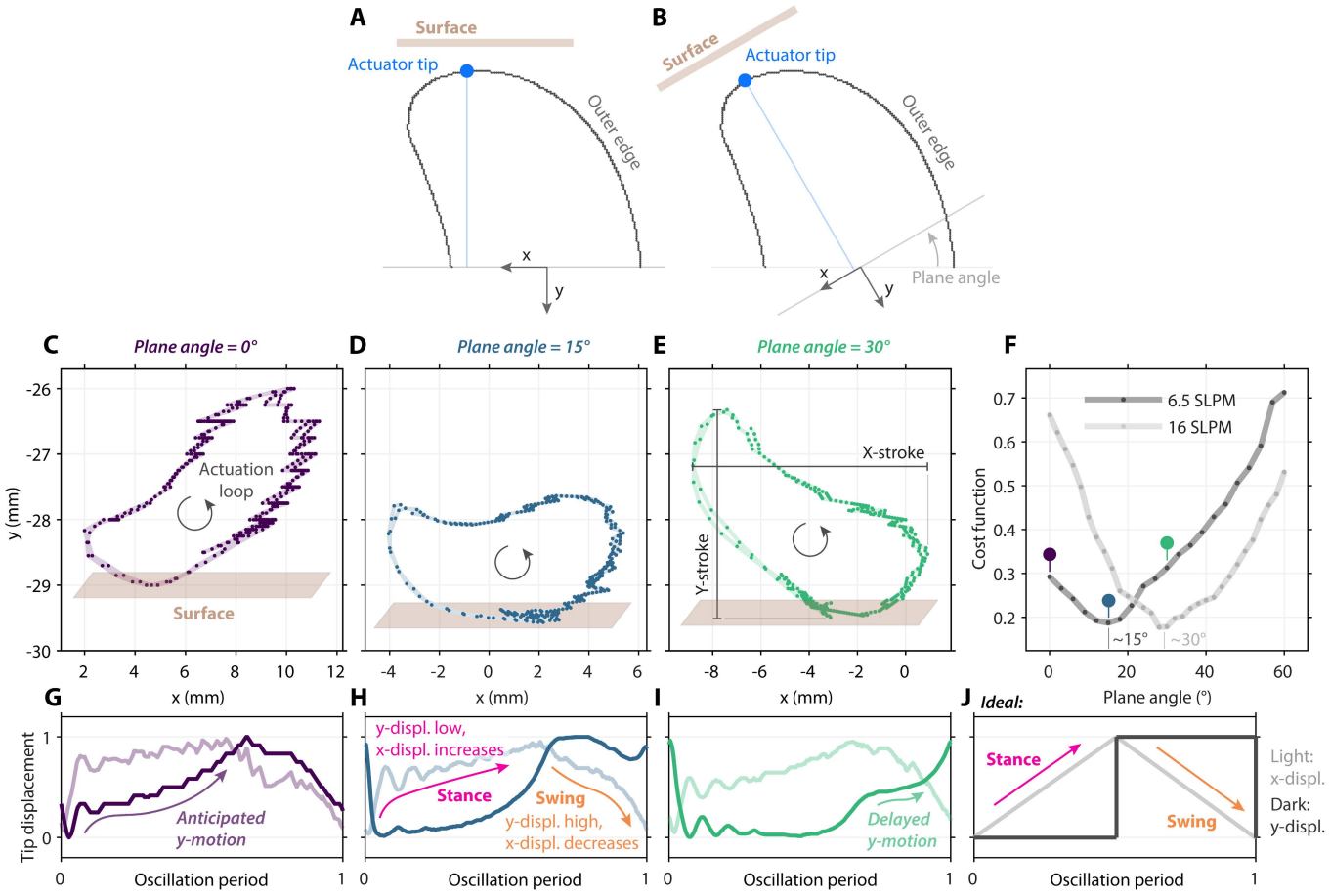

Figure S10: **The full-step actuation cycle is influenced by the angle between the limb and the surface.** (**A**) The limb tip is defined as the point of the outer edge furthest from the x-axis of the actuating plane reference frame (the x-axis is parallel to the surface on which the limb will step). (**B**) When the reference frame of the surface is rotated, the limb tip is, by definition, a different point. (**C**, **D**, **E**) Limb tip trajectory for plane angle $0°$, $15°$, and $30°$, for input airflow of 6.5 SLPM. (**F**) The shape of the cost function, defined as the ratio between the y-stroke and the x-stroke, for plane angle between $0°$ and $60°$. (**G**, **H**, **I**) Normalized x and y displacement (in the actuating plane reference frame) of the limb tip in time, for plane angle equal to $0°$, $15°$, and $30°$. (**J**) The shape of x and y displacement in time of an ideal full-step cycle. In **G**, **H**, **I**, **J**, we refer to x (light curves) and y (dark curves) as the displacements of the limb tip along the two axes of the reference frame of the actuating plane defined in **A**.

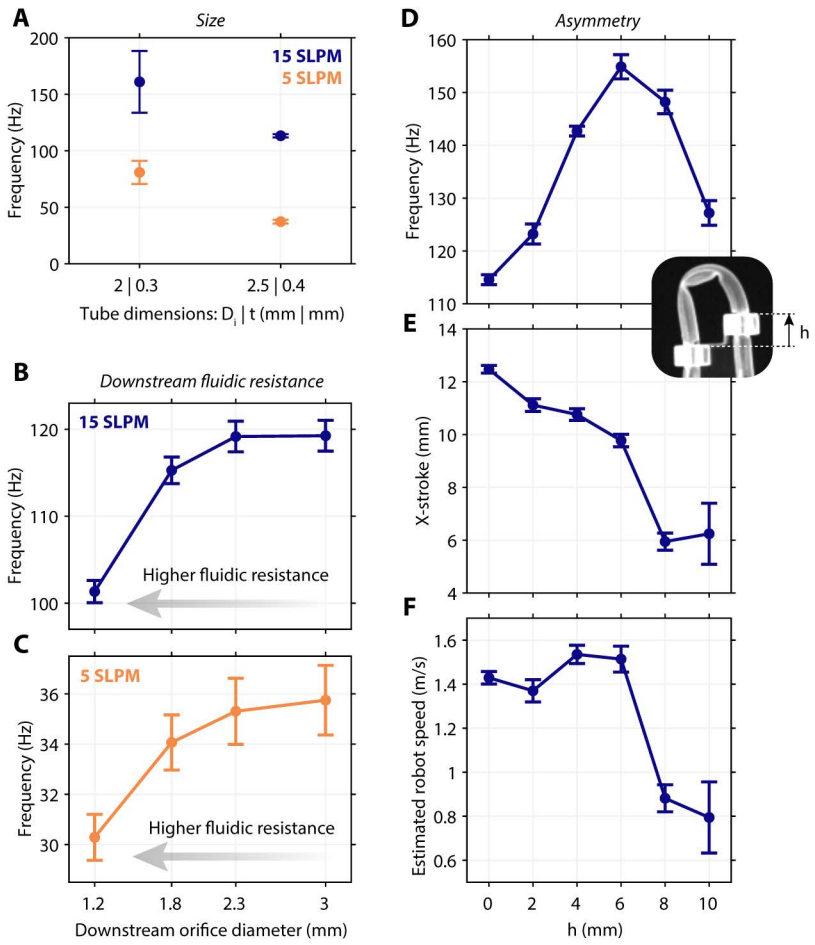

Figure S11: **Frequency dependencies of the silicone tube actuator.**
(**A**) Oscillation frequency of a reference silicone tube design (with $l = 36\,\mathrm{mm}$, $D_i = 2.5\,\mathrm{mm}$, $t = 0.4\,\mathrm{mm}$, and $d = 10\,\mathrm{mm}$), and a factor ~ 0.8 scaled design, for the 15 SLPM (resonant) case and for the 5 SLPM (non-resonant) case. (**B**, **C**) We place a needle in series with the actuator, connected to the outlet, to introduce a downstream fluidic resistance. Influence of the downstream orifice diameter over the frequency for the resonant case in **B** and the non-resonant cases in **C**. Influence of the asymmetry parameter h over (**D**) the oscillation frequency, (**E**) the x-stroke of actuation, and (**F**) the locomotion speed of a hypothetical one-limb robot, for inflow $15\,\mathrm{SLPM}$.

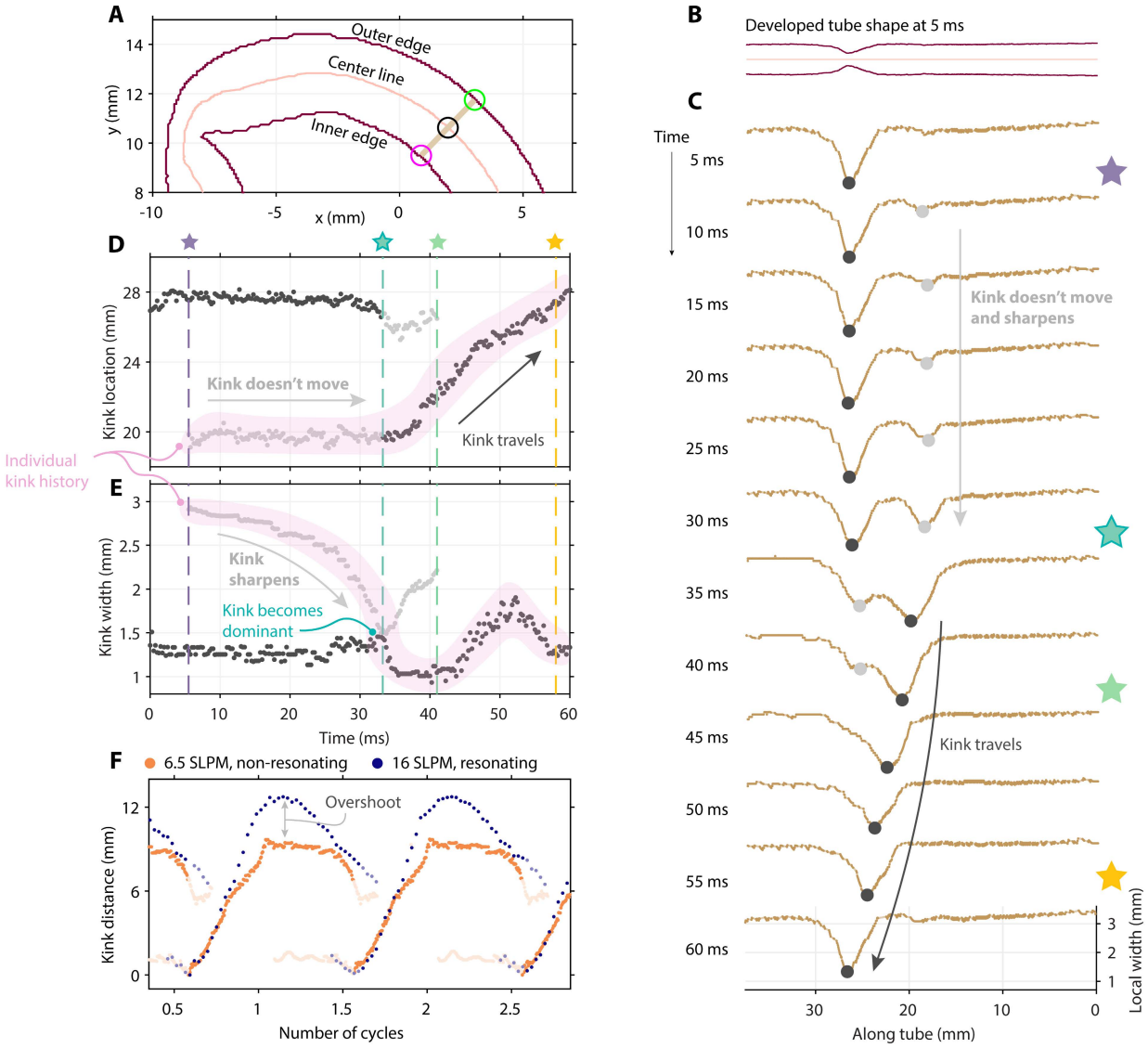

Figure S12: **Kinks behavior in time.**
(**A**) Visualization of the outer and inner edges of the tube (red), the center line (pink), and the local width (brown). (**B**) Tube resolved on the center line. (**C**) Local width along the tube every 5 ms. (**D**) History of the individual kink location (pink highlight), with an initial non-moving state (grey arrow) and a subsequent traveling state (black arrow). (**E**) History of the individual kink width, with the kink sharpening while being non-dominant and non-moving (grey arrow), until it becomes dominant (blue star). (**F**) Kink distance for the non-resonating (6.5 SLPM) and resonating (16 SLPM) cases.

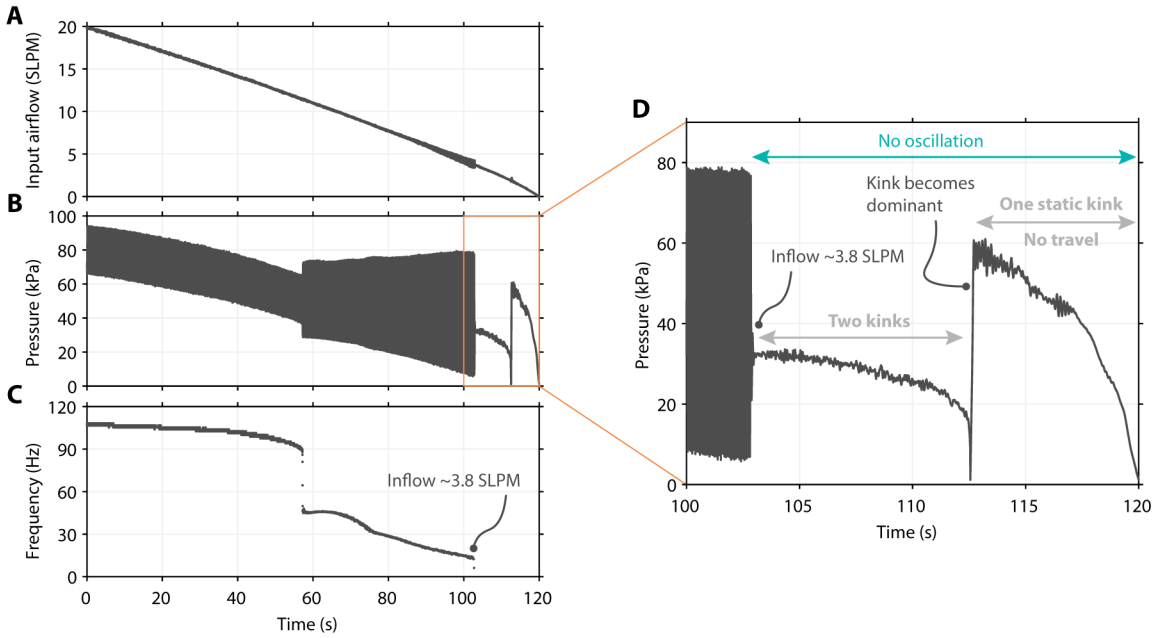

Figure S13: **Flow-controlled response.**
We take a silicone tube actuator with $l = 36\,\mathrm{mm}$, $D_i = 2.5\,\mathrm{mm}$, $t = 0.4\,\mathrm{mm}$, and $d = 10\,\mathrm{mm}$. (**A**) Applied input airflow profile, linearly decreasing from 20 SLPM to 0 SLPM in $2\,\mathrm{min}$. Measured (**B**) pressure and (**C**) frequency. (**D**) The pressure profile between ~ 4 SLPM and 0 SLPM highlights the leaking state of the kinks when the inflow is below ~ 3.8 SLPM.

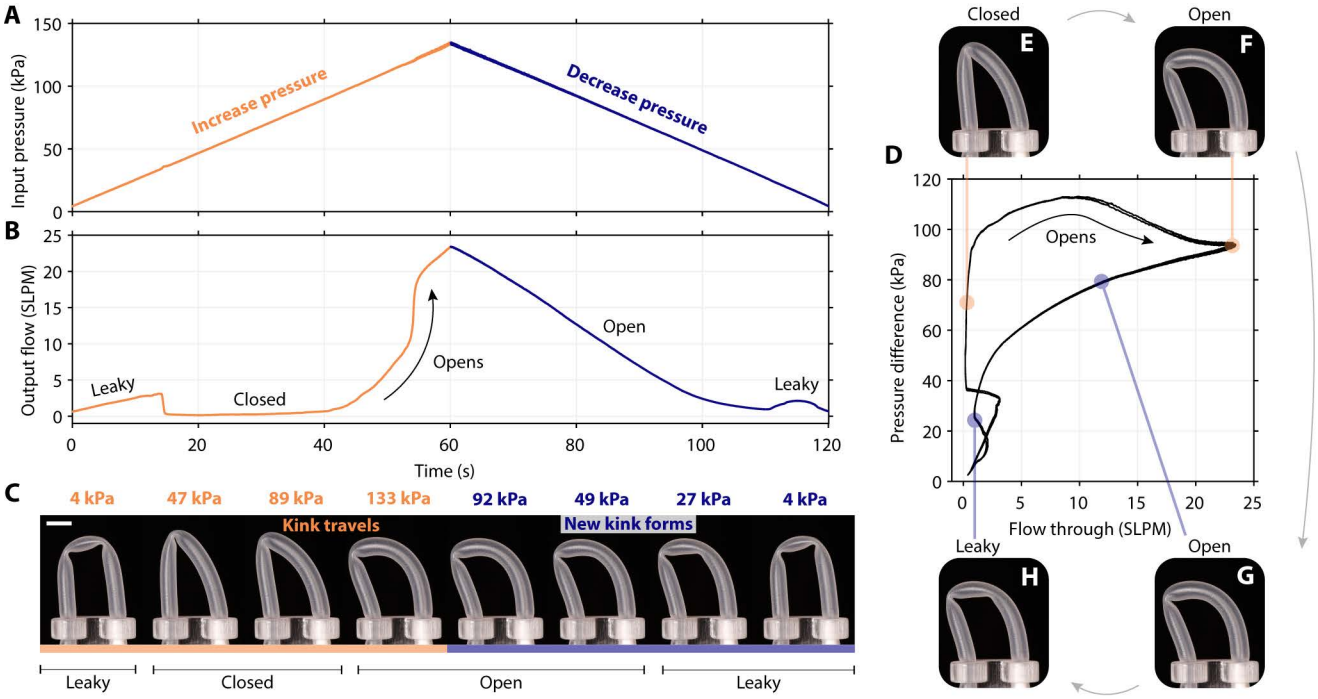

Figure S14: **Quasi-static pressure-controlled response.**
We take a silicone tube actuator with $l = 36\,\mathrm{mm}$, $D_i = 2.5\,\mathrm{mm}$, $t = 0.4\,\mathrm{mm}$, and $d = 10\,\mathrm{mm}$. (**A**) The applied pressure profile increases to $130\,\mathrm{kPa}$ in one minute, and then decreases to atmospheric pressure in one minute. (**B**) The output flow through the tube throughout the experiment. (**C**) Snapshots of the tube state in time. (**D**) Pressure-flow profile, for two subsequent cycles of pressure loading and unloading. (**E**, **F**, **G**, **H**) Snapshots of four key states.

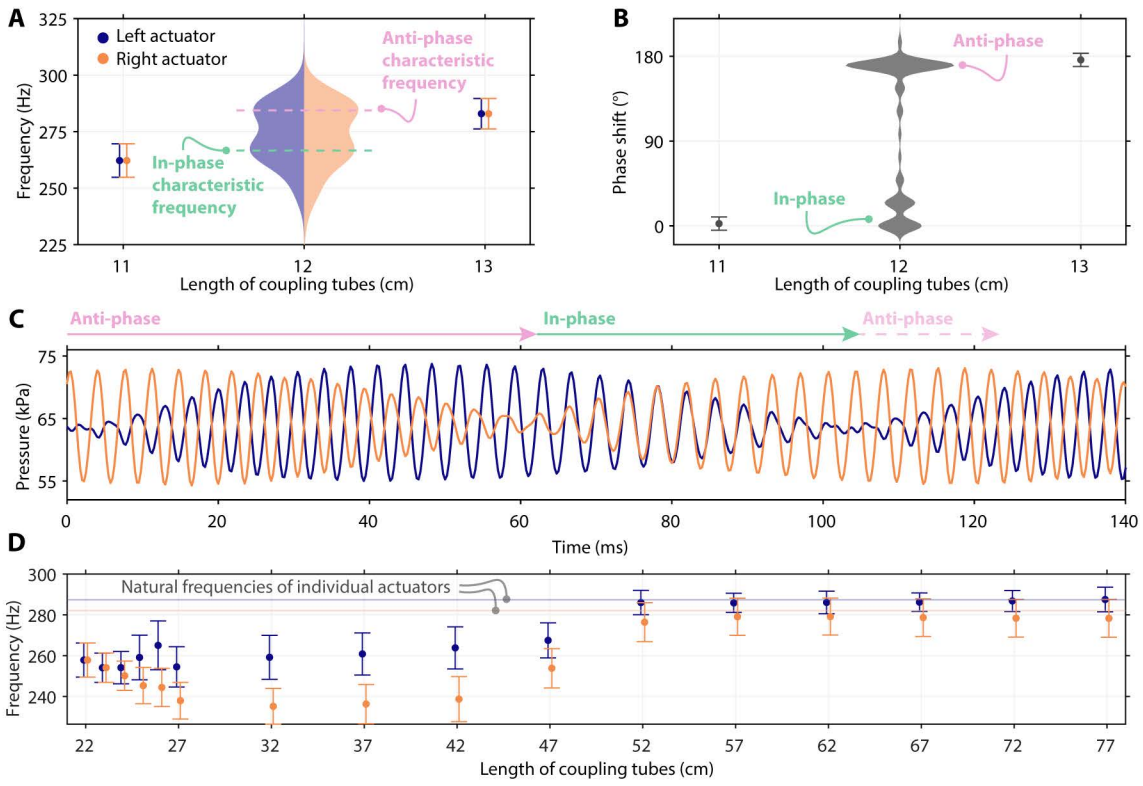

Figure S15: **Fluidic coupling.**
(**A**) Distribution of the oscillation frequencies of two actuators coupled through two coupling tubes of length $12\,\mathrm{cm}$ (data reported in Figure 3F). The actuators have $l = 18\,\mathrm{mm}$, $D_i = 2\,\mathrm{mm}$, $t = 0.3\,\mathrm{mm}$, $d = 7.8\,\mathrm{mm}$, and $h = 3.9\,\mathrm{mm}$. (**B**) Distribution of the phase shift (data reported in Figure 3G). (**C**) Pressure signals of the two actuators in time. (**D**) Frequency of the two actuators for coupling tubes' length between $22\,\mathrm{cm}$ and $77\,\mathrm{cm}$.

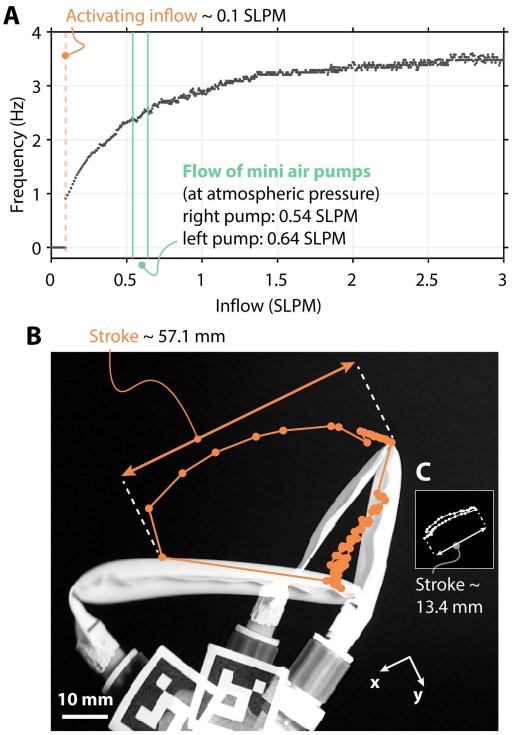

Figure S16: **Frequency and stroke of the TPU pouch actuator.**
(**A**) Frequency of the TPU pouch actuator for increasing input airflow from $0\,\mathrm{SLPM}$ to $3\,\mathrm{SLPM}$. (**B**) Trajectory of the actuator tip on the rotated x-y reference frame (data reported in Figure 4B). (**C**) Tip trajectory of the silicone tube actuator in the same scale as the TPU pouch actuator.

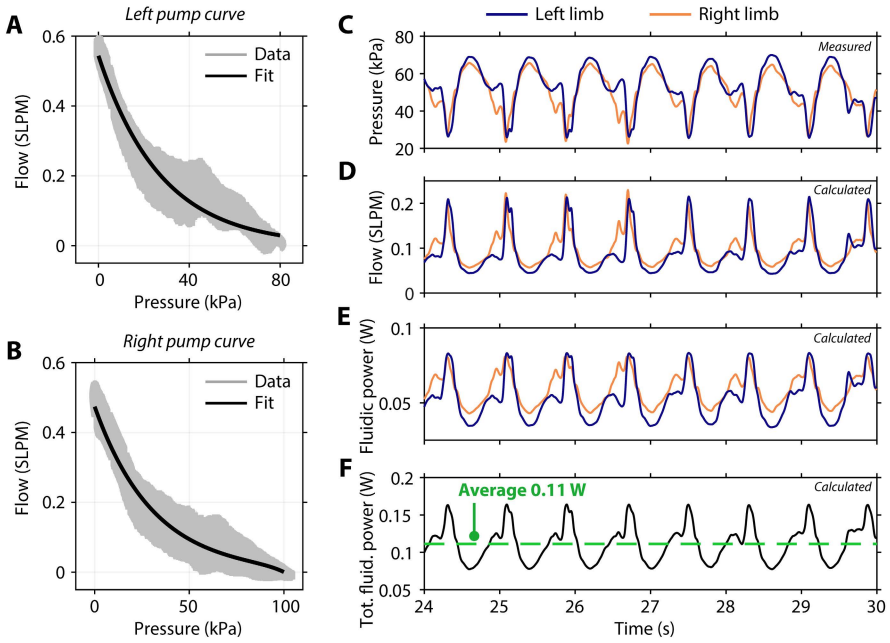

Figure S17: **Fluidic power required for the TPU pouch actuators to operate in the untethered scenario.** The pressure-flow curves of the pumps connected to (**A**) the left actuator and (**B**) the right actuator of the untethered robot. (**C**) The measured pressures of the left and right actuators of the robot locomoting on the ground (experiment shown in Figure 4H-J in the main text). (**D**) The flow provided to each actuator, determined from the pressure values in **C** and the pump curves in **A** and **B**. (**E**) The fluidic power provided to each actuator, determined by multiplying the pressure in **C** in pascal and the flow in **D** converted to cubic meters per second. (**F**) The total fluidic power provided to the robot, obtained by summing the fluidic power provided to the two actuators in **E**.

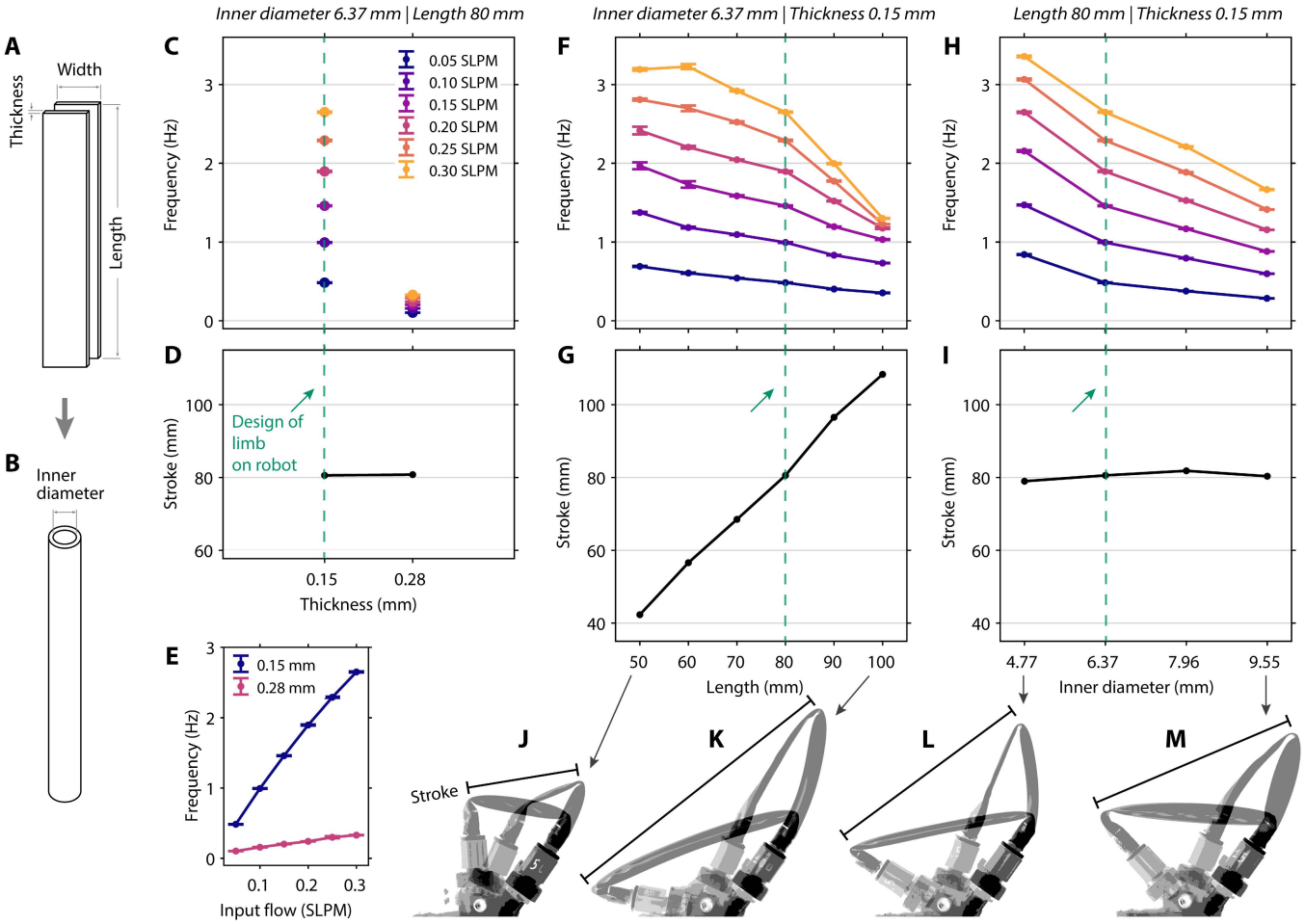

Figure S18: **Characterization of the TPU pouch actuator for several design parameters.** (**A**) The TPU pouch actuator is characterized by three design parameters: the thickness t of the TPU sheet, the length L of the sealing lines, and the width W between the sealing lines. (**B**) When inflated with air and at atmospheric pressure, these design parameters result in a tube with the same length, the same thickness, and inner diameter equal to $2 \cdot W/\pi$. (**C**) Frequency and (**D**) stroke of the actuator as a function of thickness. The tubes have fixed inner diameter $6.37\,\mathrm{mm}$ and length $80\,\mathrm{mm}$. (**E**) Frequency as a function of the input flow for the tubes with thickness $0.15\,\mathrm{mm}$ and $0.28\,\mathrm{mm}$. (**F**) Frequency and (**G**) stroke of the self-oscillating tube as a function of length for various input flows between 0.05 SLPM and 0.30 SLPM. The tubes have fixed inner diameter $6.37\,\mathrm{mm}$ and thickness $0.15\,\mathrm{mm}$. (**H**) Frequency and (**I**) stroke of the actuator as a function of width. The tubes have fixed length $80\,\mathrm{mm}$ and thickness $0.15\,\mathrm{mm}$. In panels **C**, **D**, **F**, **G**, **H**, and **I**, the green dashed line refers to the design parameters of the limb that we placed on the untethered robot. In panels **C**, **F**, and **H**, each dot represents the average frequency and standard deviation over $20\,\mathrm{s}$ of steady-state oscillation. (**J**,**K**,**L**,**M**) Overlapped photographs highlight the stroke of the actuator for four example cases.

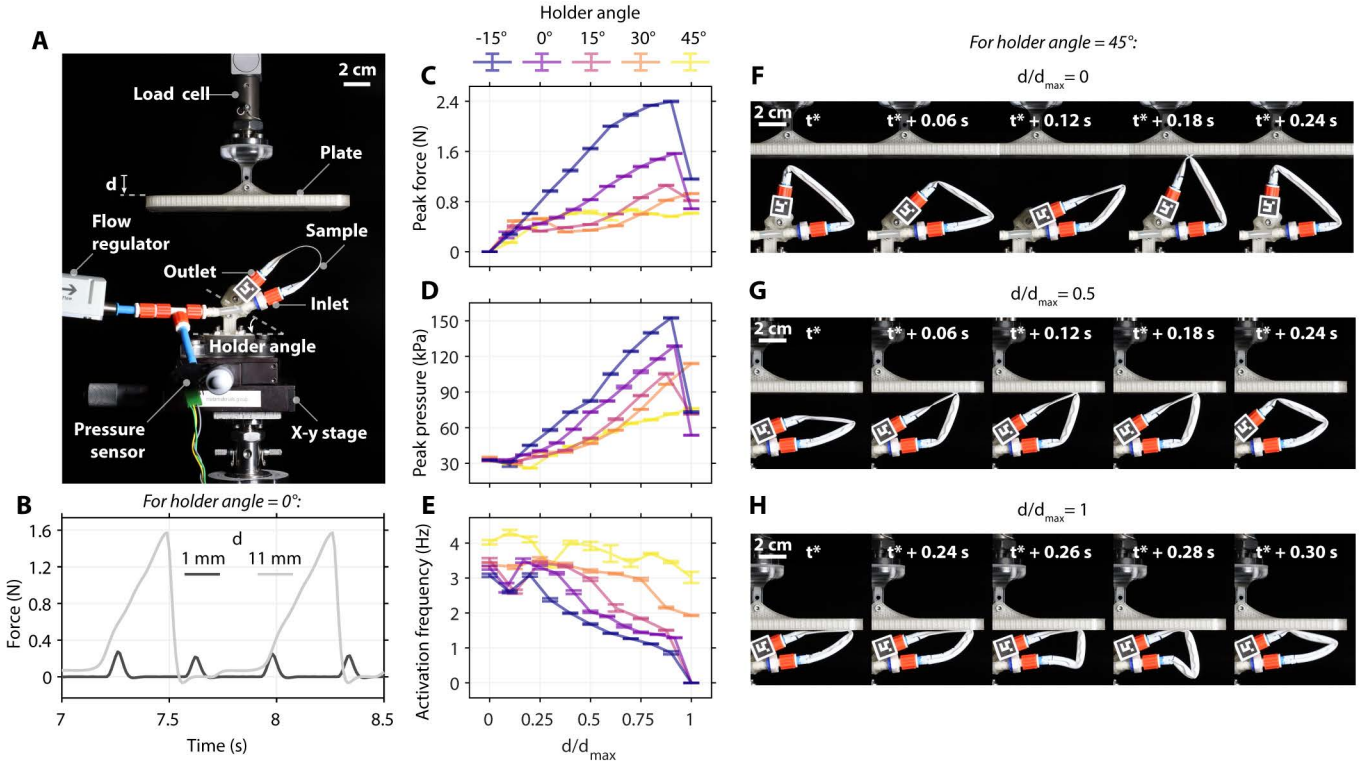

Figure S19: **Constrained actuation of the TPU pouch actuator.**
(**A**) The experimental setup measures the force exerted by the actuator while oscillating against a fixed wall. (**B**) Example force profiles for a fixed holder angle ($0°$), for wall displacement d equal to 1 mm and 11 mm. (**C**) Peak force, (**D**) peak actuator pressure, and (**E**) oscillation frequency for five holder angle values, increasing the wall displacement. In the example case of the holder angle equal to $45°$, the oscillation cycle of the actuator for (**F**) $d/d_{\max} = 0$, (**G**) $d/d_{\max} = 0.5$, and (**H**) $d/d_{\max} = 1$.

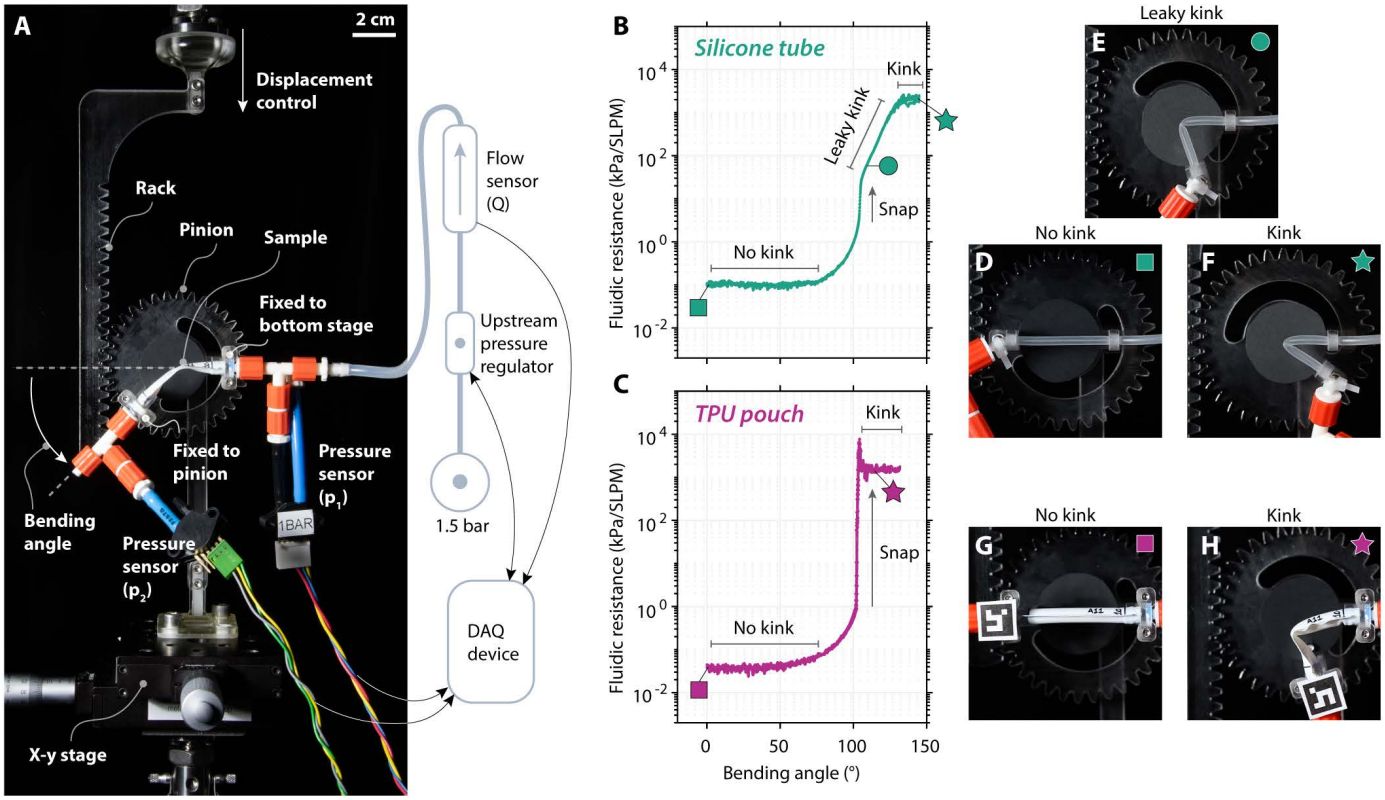

Figure S20: **Setup for experiments on kink behavior under bending and pressurization.** (**A**) The experimental setup to control the bending angle and the upstream pressure of a tube while measuring the pressure drop over, and the flow through, the tube. Two example datasets for (**B**) the silicone tube sample and (**C**) the TPU pouch sample, where we fix the upstream pressure to $20\,\mathrm{kPa}$, and we increase the bending angle in 1 minute. In both **B** and **C**, we overlay the results of three tests. In the case of the silicone tube, for increasing bending angle, after (**D**) an initial state with the absence of a kink, we observe (**E**) a snapping event to a leaky-link state, followed by (**F**) a fully-formed-kink state. In the case of the TPU pouch actuator, after (**G**) the no-kink state, the system directly snaps to (**H**) a fully-formed-kink state.

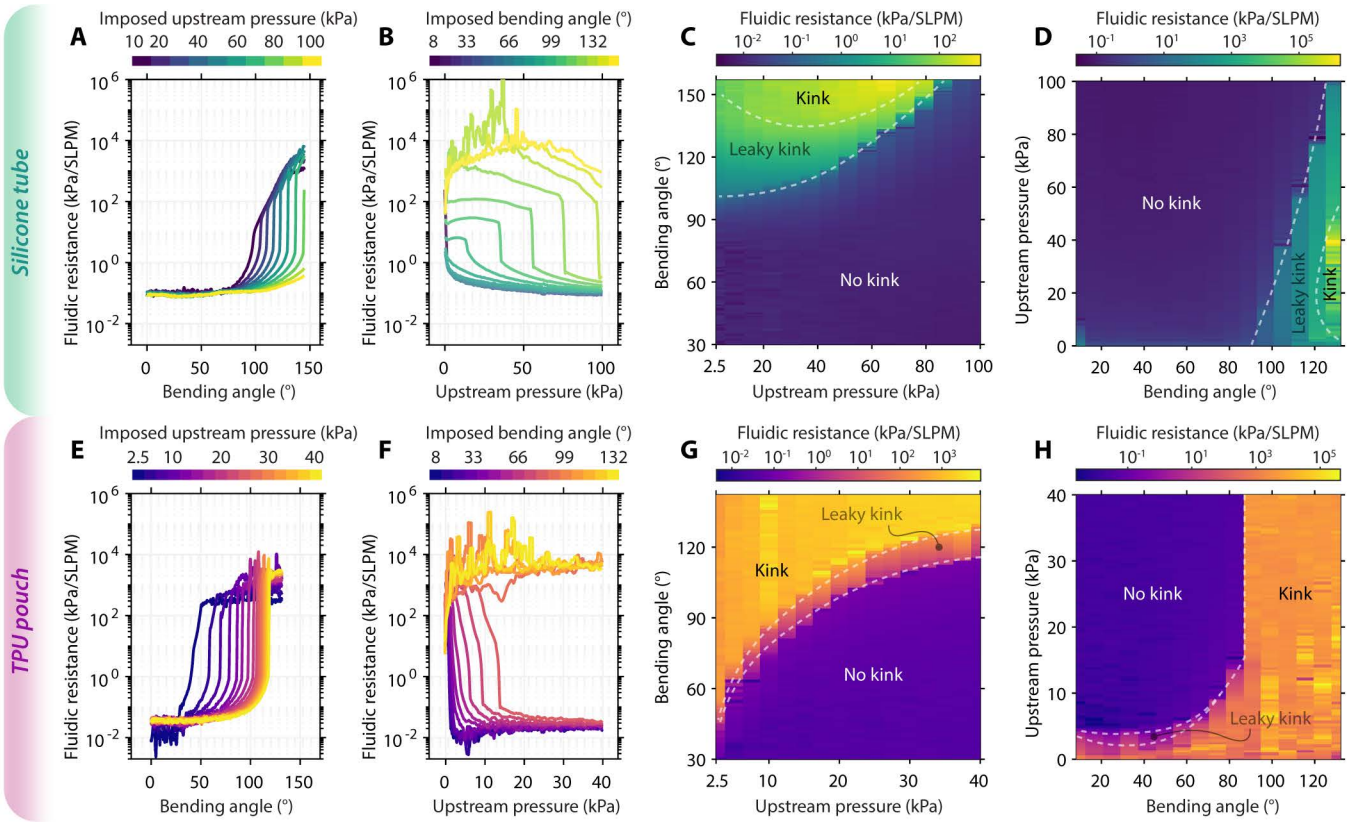

Figure S21: **Behavior of the kink under bending and pressurization.**
(**A**, **E**) Fluidic resistance resulting from the quasi-static sweep of the bending angle, for different values of imposed upstream pressure (**A** silicone tube, **E** TPU pouch). (**B**, **F**) Fluidic resistance resulting from the quasi-static sweep of the upstream pressure for different values of imposed bending angle (**B** silicone tube, **F** TPU pouch). (**C**, **G**) The resulting phase space when we fix the upstream pressure and sweep the bending angle (**C** silicone tube, **G** TPU pouch). (**D**, **H**) The resulting phase space when we fix the bending angle and sweep the upstream pressure (**D** silicone tube, **H** TPU pouch).

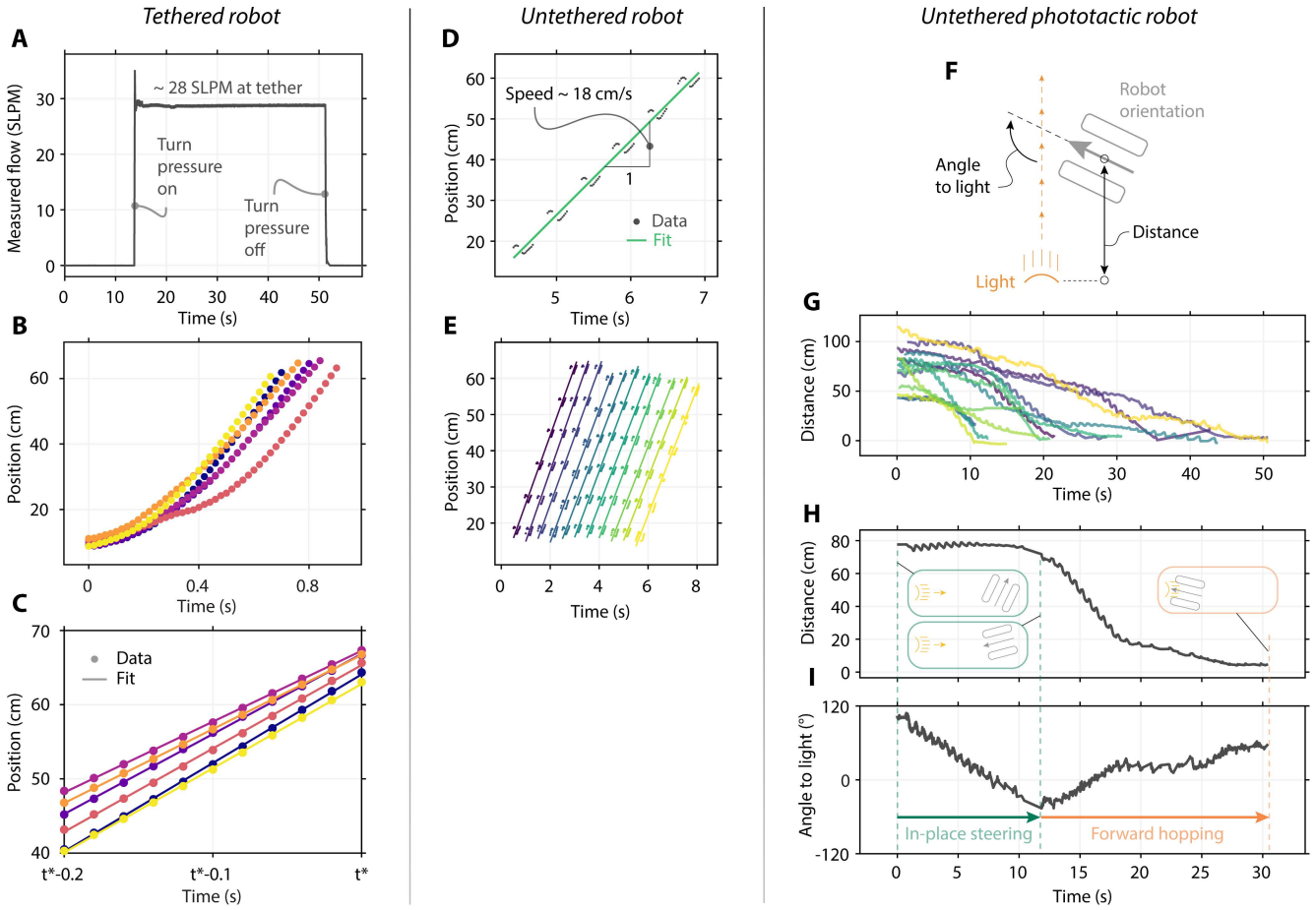

Figure S22: **Running robots.**
(**A**) We provide constant flow as input using a pressure source of $1.7\,\mathrm{bar}$ at the tether. (**B**) We let the robot run, measuring its location every $20\,\mathrm{ms}$. (**C**) Last 11 datapoints of the location for each test (dots, each run with a different color), and linear fit (lines, each run with a different color). (**D**) One example dataset of the tracked position in time of the untethered robot (dots) and linear fit (line). (**E**) Eleven tests of the hopping untethered robot, offset by $0.5\,\mathrm{s}$ (each run with a different color). (**F**) Schematic showing the definitions used to describe the distance and orientation of the phototactic robot with respect to the light source. (**G**) The autonomous version of the untethered robot achieves phototaxis (87% success rate) among 15 runs (each run with a different color) as shown by the distance between the robot and the light decreasing in time. Detected (**H**) distance of the robot from the light and (**I**) its angle to the light during one example run.

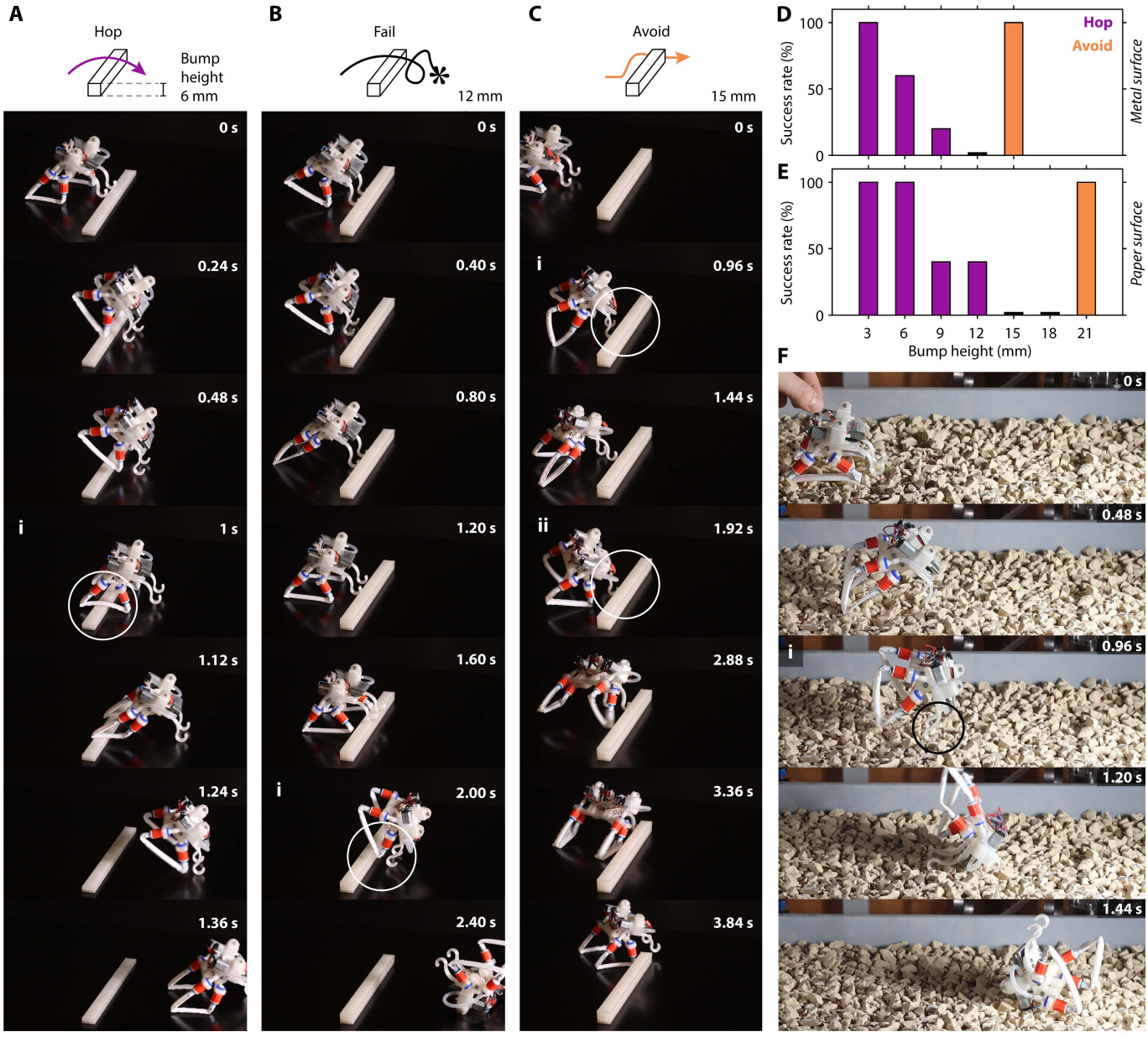

Figure S23: **The untethered robot negotiating bumps.**
We observe three distinct reactions of the robot to a bump. (**A**) For bump height $6\,\mathrm{mm}$, the robot hops over the bump, (i) with the limbs deforming when interacting with the bump. (**B**) For bump height $12\,\mathrm{mm}$, the robot fails to negotiate the bump, (i) flipping around the front limbs. (**C**) For bump height $15\,\mathrm{mm}$, the bump acts as an obstacle (experiment reported in Figure 5C in the main text). (i, ii) As the robot interacts with the obstacle, the limbs activate asynchronously, and the robot steers in place. (**D**) Success rate of bump negotiation on a flat metal surface, varying bump height (five tests for each value of bump height). (**E**) Success rate of negotiation on a paper surface. (**F**) When locomoting on granular terrain with granule size $8\,\mathrm{mm}$-$16\,\mathrm{mm}$, the robot fails, (i) displaying the pivot-flipping behavior seen in **B**.

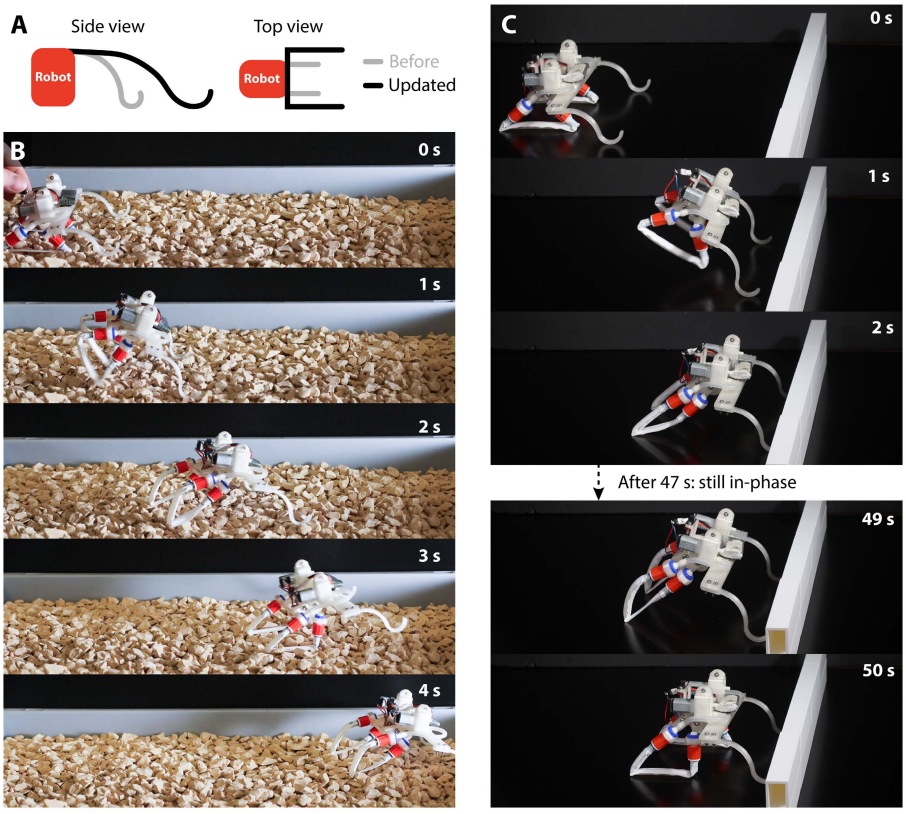

Figure S24: **Updated design of the front rigid limbs results in successful locomotion on granular terrain.** (**A**) Side view and top view of the robot (red) with the updated front rigid limbs (black) compared to the previous limbs (grey). The updated limbs are $15\,\mathrm{mm}$ longer and $105\,\mathrm{mm}$ wider. (**B**) The updated robot does not display the pivot-flipping issue seen in Figure S23 and successfully locomotes on a granular terrain with granule size $8\,\mathrm{mm}$-$16\,\mathrm{mm}$. (**C**) The updated design diminishes the rotational motion of the robot, stabilizing the in-phase synchronization of the self-oscillating limbs and therefore preventing the obstacle avoidance behavior observed in Figure S23C.

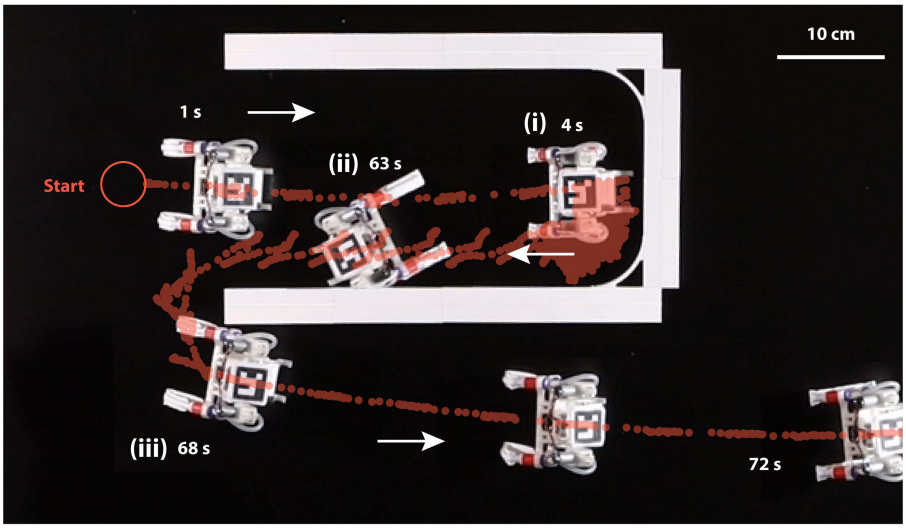

Figure S25: **The robot autonomously escapes U-shaped obstructions.**
When interacting with the walls, the robot randomly turns left or right, as shown in Figure S23C. (i) In this example test, the robot after $4\,\mathrm{s}$ interacts with the first wall. In the next $\sim 60\,\mathrm{s}$, the robot turns right and left multiple times, until it turns right twice in a row. (ii) The robot then hops straight. When the robot interacts with the bottom-left corner, the robot turns $180°$. Note that this last interaction is particularly sensitive to the approach angle, as we observed the robot taking various random directions after interacting with corners (movie S6).

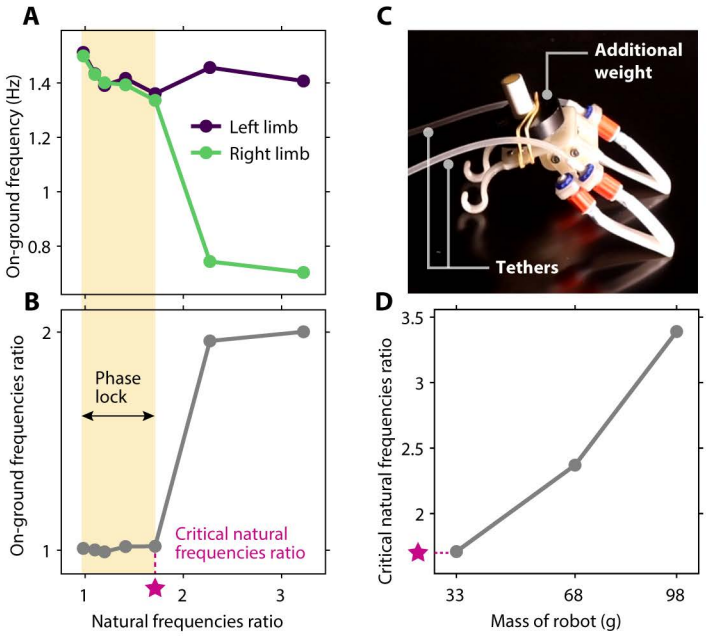

Figure S26: **A larger body mass increases tolerance to imbalance in left and right inputs.** We provide different values of inflow to the left and right limbs, and we measure both the two natural frequencies and the frequencies when the robot locomotes on the ground. (**A**) Frequencies of the left and right limbs when the robot locomotes on the ground as a function of the ratio of the natural frequencies of the two limbs. (**B**) Ratio of the on-ground frequencies of the limbs as a function of the ratio of the natural frequencies of the two limbs. The purple star indicates the critical natural frequencies ratio – higher values result in the limbs not activating in-phase, while lower values result in the phase lock of the limbs. (**C**) The robot has an additional weight placed on its back, and one tether connected to each limb. (**D**) The critical ratio of the natural frequencies increases for increasing mass of the robot.

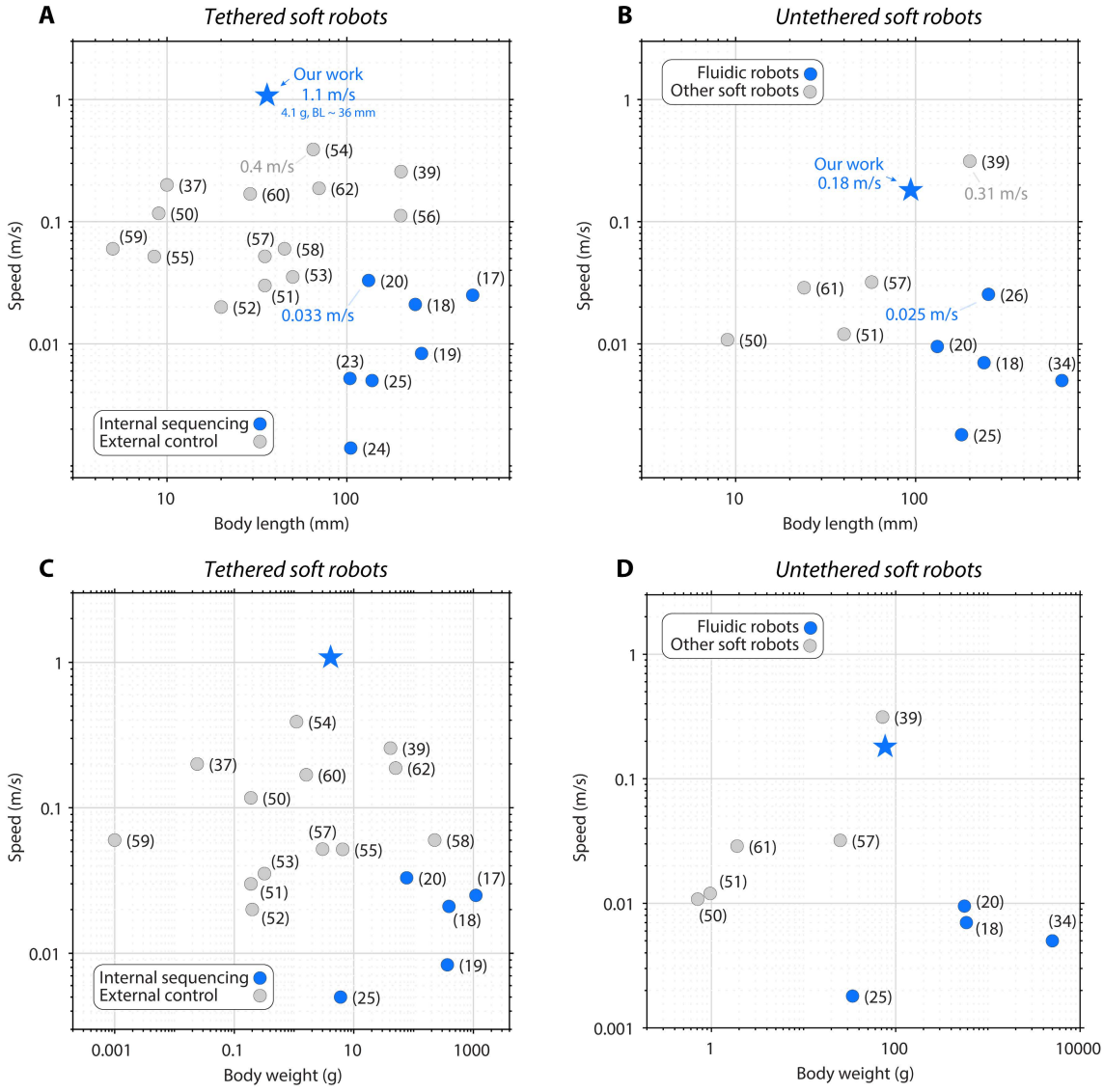

Figure S27: **Comparison between our robots and comparable state-of-the-art soft robots.** Body length of some of the current fastest (**A**) tethered and (**B**) untethered soft robots versus their absolute speed. Body weight of some of the current fastest (**C**) tethered and (**D**) untethered soft robots versus their absolute speed. The data points in **A** and **C** are reported in Table S2. The data points in **B** and **D** are reported in Table S3.

Table S1: **Lookup table for the conversion of units of flow rate.**
Values of flow rate in standard liter per minute (SLPM), used throughout the article, converted to cubic meter per second (m^3/s) using Eq. (3).

Flow rate (SLPM)	*Flow rate* (m^3/s)
0	0
0.05	8.9×10^{-7}
0.1	1.78×10^{-6}
0.3	5.34×10^{-6}
0.4	7.12×10^{-6}
3.8	6.76×10^{-5}
4	7.12×10^{-5}
6.5	1.16×10^{-4}
7.5	1.33×10^{-4}
11.4	2.03×10^{-4}
15	2.67×10^{-4}
16	2.85×10^{-4}
20	3.56×10^{-4}
28	4.98×10^{-4}

Table S2: **State-of-the-art tethered soft robots.**
Data of the tethered soft robots reported in Fig. 3J and in Figure S27A,C sorted for descending relative speed in body lengths per second ($\mathrm{BL/s}$).

Reference	*Speed* ($\mathrm{BL/s}$)	*Speed* ($\mathrm{mm/s}$)	*Weight* (g)	*Length* (mm)
Our work	30	1080	4.09	36
(*37*)	20	200	0.024	10
(*50*)	13	117	0.19	9
(*59*)	12	60	0.001	5
(*55*)	6.1	51.83	6.5	8.5
(*54*)	6.01	390.5	1.1	65
(*60*)	5.82	168.6	1.6	29
(*62*)	2.68	187.5	50	70
(*57*)	1.5	52	3	35
(*58*)	1.33	60	225	45
(*39*)	1.28	257	41	200
(*52*)	1	20	0.2	20
(*51*)	0.85	30	0.19	35
(*53*)	0.7	35.3	0.32	50
(*56*)	0.56	112	n/a	199
(*20*)	0.25	33	76.5	132
(*18*)	0.09	21	390	240
(*17*)	0.05	25	1100	500
(*23*)	0.05	5.2	n/a	104
(*19*)	0.033	8.33	367	260
(*25*)	0.03	5	6	138
(*24*)	0.01	1.4	n/a	105

Table S3: **State-of-the-art untethered soft robots.**
Data of the untethered soft robots reported in Figure S27B,D sorted for descending relative speed ($\mathrm{BL/s}$).

Reference	*Speed* ($\mathrm{BL/s}$)	*Speed* ($\mathrm{mm/s}$)	*Weight* (g)	*Length* (mm)
Our work	1.93	181	76.7	94
(*39*)	1.56	313	72	200
(*50*)	1.2	10.8	0.71	9
(*61*)	1.2	28.8	1.9	24
(*57*)	0.56	32	25	57
(*51*)	0.3	12	0.97	40
(*26*)	0.1	25.4	n/a	254
(*20*)	0.07	9.5	556	132
(*18*)	0.03	7	584	240
(*25*)	0.01	1.8	34	180
(*34*)	0.0076	5	5000	650

Table S4: **Components of the fluidic data acquisition setup.**
List of the components used to regulate and acquire the fluidic quantities (pressure and flow).

Part	*Model*
Input/output board	National Instruments IN USB-6212
Precision pressure regulator	Festo™ LRP-1/4-10
Proportional pressure regulator	Festo™ VEAB-L-26-D18-Q4-V1-1R1
Proportional flow control valve	Festo™ VEMD-L-6-14-20-D21-M5-1-R1-V4
Pressure sensor $100\,\mathrm{kPa}$	NXP MPX5100DP
Pressure sensor $250\,\mathrm{kPa}$	NXP MPX4250DP
Pressure sensor $15\,\mathrm{psi}$	Honeywell 015PDAA5
Flowrate sensor $20\ \mathrm{SLPM}$	Honeywell AWM5104

Movie S1. The self-oscillating limb. The self-oscillating limb is a soft tube bent 180° and constrained in a rigid holder. i) The limb performs a full-step motion while self-oscillating at a high frequency of $\sim 100\,\mathrm{Hz}$, when constant input airflow of $15\,\mathrm{SLPM}$ is provided. High-speed recordings highlight the asymmetric cyclic motion of the limb, in slow motion (200x slower, repeated movies of two consecutive oscillations). The trajectory of the limb's tip on the actuating plane shows that the x- and y-coordinates are intrinsically sequenced, tracing the full-step loop in the plane. ii) The TPU pouch version behaves similarly to the silicone tube limb, while exhibiting higher stroke and hysteresis in the actuation, at lower frequencies. iii) The self-oscillating limb is versatile, operating with both compressible (air) and incompressible (water) driving fluids. We supply water flows of $333\,\mathrm{mL/min}$ to the silicone tube limb and $56\,\mathrm{mL/min}$ to the TPU pouch limb, respectively.

Movie S2. The resonating behavior. High-speed recordings highlight that the resonating behavior of the limb enables high frequencies of oscillation. i) We detect the edges of the tube for each frame of the recording. The kinks are the points along the tube corresponding to the minima of the tube width (distance between edges). The behavior of the tube width in time (40x slower, repeated movies of two consecutive oscillations) shows that the kinks arise, travel, and disappear along the tube. ii) The distance covered by the kinks on the plane and their velocity show that high frequencies of oscillation are triggered by resonance. The distance covered by the kink in the resonating case overshoots by $\sim 50\%$ the one of the non-resonating case. The kink velocity in the resonating case is quasi-sinusoidal and reaches $\sim 3.5\,\mathrm{m/s}$, while in the non-resonating case is not quasi-sinusoidal and stays close to zero.

Movie S3. Synchronizing via fluidic coupling. We realize strong coupling between two self-oscillating limbs through parallel connection to the same flow source of $15\,\mathrm{SLPM}$ using Y-connected tubes. We vary the length of these coupling tubes, and we display the measured pressure and the high-speed recordings (200x slower). For short coupling tubes of $7\,\mathrm{cm}$, we observe in-phase synchronization (same frequency, phase $\sim 0°$). For longer coupling tubes ($17\,\mathrm{cm}$), we observe anti-phase synchronization (same frequency, phase $\sim 180°$).

There is a critical length for which the behavior transitions from in-phase to anti-phase. When the system is placed at this transition ($12\,\mathrm{cm}$), the self-oscillating limbs continuously alternate between the two eigenmodes.

Movie S4. The tethered robot. The tethered robot runs at more than one meter per second with a stotting gait. As a reference for scale, the body length of the robot is $36\,\mathrm{mm}$. i) The robot design consists of a monolithic rigid body and four tubes as self-oscillating limbs. The robot moves at 30 ± 2.5 body lengths per second ($1.1 \pm 0.09\,\mathrm{m/s}$) among six runs. ii) High-speed recordings of the robot (400x and 800x slower) show that the four limbs perform full steps with in-phase synchronization, being fluidically coupled through the inner channels. The robot is locomoting with a stotting gait. When the robot is not in contact with the ground, the four limbs are still synchronized, confirming that the coupling arises from the fluidic internal connections and not from the interaction with the ground. iii) When the four limbs are not synchronized, the robot stumbles, and ultrafast speeds are not reached anymore (10x slower).

Movie S5. The untethered robot. The untethered robot exploits environmental interactions to achieve in-phase synchronization of two limbs, moving at 1.9 body lengths per second. All the recordings are in real time. For scale, the robot's body length is $94\,\mathrm{mm}$. i) The untethered robot is equipped with two self-oscillating limbs, two mini air pumps, a LiPo battery, and two rigid balance limbs. When the pumps are turned on, the robot displays a hopping gait. ii) Occasionally, we observe a transient phase with no synchronization of the limbs during the startup of the pumps. iii) When upside-down, the limbs do not synchronize, as they are independently powered by two distinct fluidic lines (one pump for each limb). iv) When we flip the robot into locomotion position, the limbs synchronize thanks to the interaction with the environment, as shown by the pressure signals of the two limbs aligning.

Movie S6. Autonomy through physical interactions with the environment. The untethered robot exploits body-environment interactions to transition between locomotion gaits depending on the medium, and to navigate obstacles autonomously. i) Before diving into the water, the robot hops on the ground with an

in-phase gait. After diving, the robot autonomously transitions to an anti-phase swimming gait. This change in behavior occurs spontaneously via the implicit coupling with the new medium, without any control input or change in morphology. The phase shift of the swimming gait, obtained from the measured pressure signals, is stable around $\sim 180^\circ$. ii) We prevent lateral swaying by manually blocking the body of the robot. In these conditions, the implicit coupling between the buoyant body and water is inhibited, and the limbs do not synchronize anymore, as seen by the phase shift assuming all values between 0° and 360°. iii) When hopping on the ground, the limbs temporarily get out of synchronization when the robot is externally perturbed, and then return to the stable synchronized mode. iv) When encountering an obstacle, too, the robot exits the synchronized mode and steers in place, randomly either to the left or right. This behavior is stochastic, as it relies on noisy, friction-dominated interactions. v) The robot harnesses the noisy body-obstacle interactions to escape a U-shaped obstruction autonomously, through consecutive random changes of direction (8x and 16x faster). vi) When the robot navigates among multiple (seven) obstacles, the outcome is unpredictable due to the stochasticity of the interactions. We overlay eight different runs recorded from above (6x faster).

Movie S7. Autonomous phototaxis through internal connections. The untethered robot exhibits autonomous phototaxis through internal connections directly between sensors and limbs. i) We design a high-level sense of direction through internal connections between the limbs and two photoresistors. The photoresistors are placed facing the front-left and front-right directions. The front-left photoresistor is connected to the right limb, and vice-versa for the front-right sensor, inspired by Braitenberg's 'aggressive vehicle' (*41*). In this way, when the light is coming, for example, from the front-left direction, the right limb will be active, and the robot will steer to the left. The robot autonomously moves toward the light (real time and 8x faster). ii) We place the robot in a dark room. When we open the door of another room, the robot prefers the brighter one (real time). iii) The robot autonomously follows an operator that carries a light in a real-world environment, the coffee corner at AMOLF (16x faster).